Shape-Preserving Physical and Chemical Transformations of Si and SiO_2 Nano- and Microstructures

A Dissertation
Presented to
The Academic Faculty

by

Ari Gordin

In Partial Fulfillment
Of the Requirements for the Degree
Doctor of Philosophy in Materials Science and Engineering

Georgia Institute of Technology
August, 2014

Shape-Preserving Physical and Chemical
Transformations of Si and SiO_2 Nano- and Microstructures

Approved by:

Dr. Kenneth H. Sandhage, Advisor
School of Materials Science
and Engineering
Georgia Institute of Technology

Dr. Michael A. Filler
School of Chemical and
Biomolecular Engineering
Georgia Institute of Technology

Dr. Thomas H. Sanders, Jr.
School of Materials Science
and Engineering
Georgia Institute of Technology

Dr. Lawrence Bottomley
School of Chemistry & Biochemistry
Georgia Institute of Technology

Dr. Angus P. Wilkinson
School of Materials Science
and Engineering
Georgia Institute of Technology

Date Approved: June 30, 2014

Acknowledgements

My advisor, Dr. Sandhage, for never accepting mediocre work, for giving me the freedom and encouragement to explore my own ideas (which rarely worked as planned), for sharing his seemingly limitless knowledge, and, it must be said, for making sure my paychecks cleared.

My committee members, including Dr. Bottomley (who taught the first class I ever took at Georgia Tech nearly a decade ago), Dr. Wilkinson (who taught the first inorganic chemistry class I ever took, which convinced me to pursue a career in solid state chemistry), and Dr. Sanders (who taught the first materials science class I ever took).

My coworkers, all of whom I consider personal friends (except Ben), for putting up with my personality, humor, complaints, and making my daily work-life enjoyable and fun, even when the work itself may not have been.

My hair-stylist, David Zecca; my personal trainer, Kafka; and my personal shopping assistant, Lucky Yates.

My parents, whose immeasurable support more often than not went unthanked (but never unappreciated).

The partner and love of my life, my wife Paulina, whose enduring support and personal sacrifices cannot be put into words. I don't know where we will go next, but I know we will get there together.

Table of Contents

List of Tables

List of Figures

List of Symbols and Abbreviations

3D	Three-Dimensional
CVD	Chemical Vapor Deposition
DI	Deionized
$D_{g.b.}$	Grain Boundary Diffusion
EDS/EDX	Energy Dispersive X-ray Spectroscopy
HC-PCF	Hollow core photonic crystal fiber
hr	hour(s)
HRTEM	High Resolution Transmission Electron Microscopy
HTXRD	High Temperature X-Ray Diffraction
IPA	Anhydrous Isopropyl Alcohol
k_p	Parabolic Rate Constant
λ	Wavelength (nm)
MACE	Metal Assisted Chemical Etching
µm	Micrometer
n	Index of Refraction
nm	nanometer(s)
NW	Nanowire
PBG	Photonic Bandgap
PC	Photonic Crystal
PCF	Photonic Crystal Fiber
Por-Si	Porous Silicon
Q	Activation Energy
QCM	Quartz Crystal Microbalance
SEM	Scanning Electron Microscopy
SiNW	Silicon Nanowire
TEM	Transmission Electron Microscopy
T_{melt}	Melting Temperature
XRD	X-ray Diffraction

Summary

Shape-preserving reactions are advantageous in that they allow for the use of well-established methods to fabricate an initial structure, followed by a secondary reaction step which introduces some modification to either the physical structure or chemical composition of the initial preform in order to produce a more desirable material which may be difficult to fabricate directly. This thesis considers two broad categories of shape-preserving transformations: **physical transformations**, in which the chemistry of the as-grown material remains constant but some structural change is introduced (i.e., conversion of dense silicon nanowires into porous silicon nanowires); and **chemical transformations**, in which the physical structure of the as-grown material remains constant but the chemical composition is changed (i.e., conversion of SiO_2 photonic crystal fibers into MgF_2 photonic crystal fibers).

Part I of this thesis focuses on the development of a process which allows for the introduction of porosity into dense silicon nano- and microstructures (a shape preserving net **physical** transformation, albeit by chemical means), while Part II focuses on conversion of SiO_2-based photonic structures into replicas with more desirable chemical compositions (a shape preserving net **chemical** transformation). Part III involves a kinetic investigation into the solid state reaction of magnesium and silicon to form magnesium silicide (Mg_2Si), which is utilized throughout this thesis.

Part I: Shape-Preserving Physical Transformation of Silicon Nano- and Microstructures

Chapter 1: Design of a Porosification Process for Si nano- and Micro-structures

1.1 Summary

Porous silicon nanostructures have been proposed for use in various applications due to a combination of the mechanical or electrical properties provided by the nanostructure along with the enhanced surface area and free volume obtained from the porosity. While the electrochemical-based production of porous films is extremely well studied, and while there are a number of established routes for fabrication of dense nanostructures, the fabrication of porous nanostructures represents a more challenging problem with only limited options. In this chapter, a novel shape-preserving process is designed to allow for the conversion of dense silicon nanostructures into porous silicon replicas via a selective leaching method. The principles and criteria behind the porosification process are described and materials are rationally selected.

1.2 Motivation

Porous silicon has been the subject of intense research over the past several decades. Due to a combination of interesting properties including high specific surface area, photo-luminescence, biocompatibility, and enhanced chemical reactivity, porous silicon based materials have been explored for potential applications in a broad range of fields including optics, sensors, energy storage, and biomedical applications[1,2]. Conventionally, porous silicon is fabricated via anodization of a single crystal silicon wafer. Although very fine control of pore sizes and total porosity of resulting porous

silicon can be achieved by varying anodization parameters, the process is nonetheless limited to producing two-dimensional porous films on a silicon wafer.

Parallel to research into porous silicon, the advancement of nanoscale fabrication techniques has allowed for the investigation of silicon nanostructures which often show strikingly unique thermal, electrical, mechanical, and optical properties when compared to bulk silicon. While nanowires have arguably received the most attention, a number of other micro- and nanostructures, including tubes, spheres, belts, opals, and complex waveguides, have also been fabricated. Numerous bottom-up (i.e. CVD, MBE, laser ablation, etc.) and top-down (advanced lithography and etching) methods have been developed for fabrication of dense silicon nanostructures.

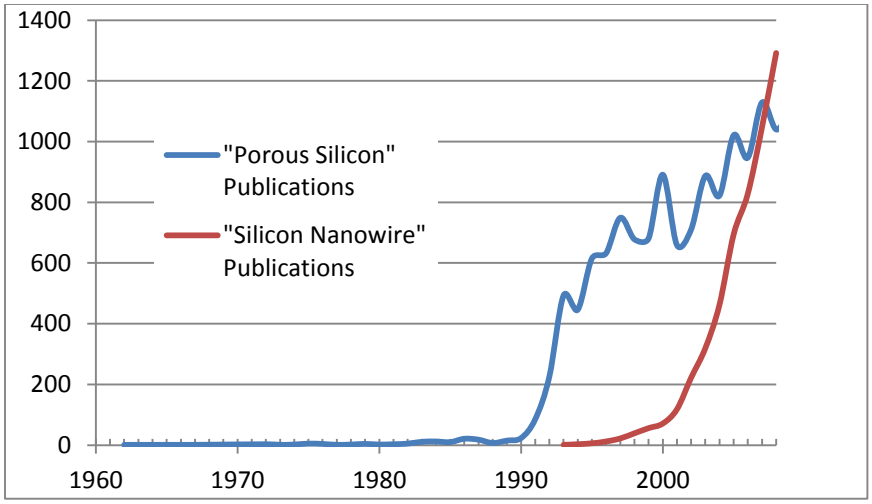

Figure 1: Number of publications/year showing simultaneous surge in interest in porous silicon and in silicon nanostructures (from Web of Science).

Similar to anodically etched porous silicon, the interest into silicon micro- and nanostructures is driven by the unique properties such structures exhibit relative to bulk silicon. As a result, silicon nanostructures have been extensively studied in many of the same fields as porous silicon, including energy storage, chemical and optical sensors, and

biomedical devices. Despite the strong overlap in potential areas of application between porous silicon and nanostructured silicon, the two lines of research have largely remained separated. Only recently have researchers begun to explore the use of *porous silicon nanostructures* which, ideally, could combine the unique properties of highly porous silicon with the advantages of silicon nanostructures (Table 1). For example, porous silicon nanoparticles have been investigated as a drug delivery material. The nanoscale structure of the particles allowed for avoidance of renal filtration, while the porosity allowed for large drug loading capacity and photoluminescence.

Table 1: Published applications involving porous silicon nanostructures.

Material	Application	Role of Nanostructure	Role of Porosity	Method of Fabrication
Por-Si Nanoparticles (no controlled shape)	Luminescent drug delivery vessels[3]	Long residual lifetime in blood stream due to ability to avoid renal filtration	Increased drug loading and luminescence	Mechanical fracture of porous film.
Por-Si Nanowires	Por-Si nanowires for Li-ion batteries[4]	One dimensional electron transport and mechanical stability	Free volume which can accommodate volume changes	Metal assisted chemical etching.
Por-Si Waveguides	Gas and bio-sensing.[5]	Light guiding	Increased surface area for analyte adsorption	Magnesiothermic reduction or AAO-masking.

Established methods allow for production of *porous films* or of *dense nanostructures*. However, methods for fabrication of *porous nanostructures* are limited. Freestanding porous silicon particles fabricated via mechanical liftoff and fracture of anodically etched porous films have shown promising results for both in-vivo medical applications and for use in lithium-ion batteries[6,7], but fine shape control from fractured films is not possible. Metal-assisted chemical etching, discussed later in the chapter, can yield porous nanowires but is fundamentally limited to highly doped silicon nanowires on

a silicon substrate. It cannot be used, for example, to generate other porous shapes either as freestanding structures or on non-silicon substrates.

The motivation behind this chapter is to design and demonstrate a shape-preserving *post-growth* process to allow for conversion of dense silicon nanostructures into porous silicon replicas. A post-growth technique, in which the initial nanostructure growth step is decoupled from the pore-generating step, is advantageous since it allows the initial dense to be fabricated using a variety of well-established methods and is not fundamentally limited to a single shape or substrate.

1.3 Background of Anodized p-Si Films

Anodically etched porous silicon was first described by Uhlir at Bell labs in 1956. Uhlir reported that electropolishing of a silicon wafer only occurred above some threshold current density and that, below this threshold, a red or black film could be observed on top of the silicon wafers[8]. Initial studies did not identify this film as porous silicon but rather speculated it may be an amorphous silicon subfluoride[9], and it was not until 1972 that this film was identified as porous silicon[10]. However, porous silicon remained a relatively niche material until the early 1990's, when both quantum confinement effects[11] and photoluminescence[12] of anodically etched porous silicon films were reported. This lead to a huge surge in the interest and number of groups investigating porous silicon films (see Figure 1).

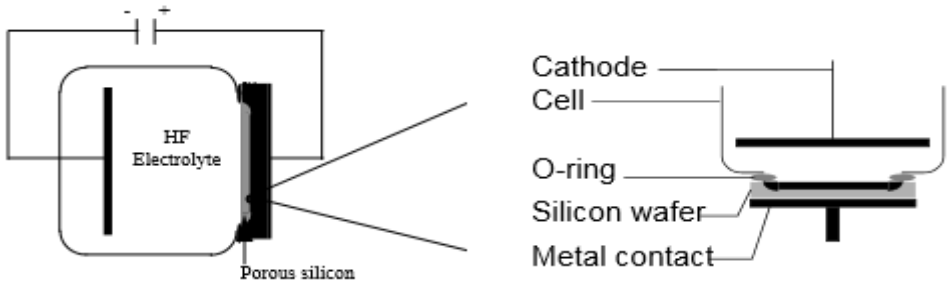

Figure 2: Schematic for Fabrication of Porous Silicon via Anodic Etching

A basic experimental schematic for electrochemical etching of silicon is shown in Figure 2. One side of a single crystal silicon wafer is attached to a metal electrode while the opposite side is exposed to a hydrofluoric acid containing electrolyte. An anodic bias is applied to the metal electrode in contact with the wafer, causing the surface of the wafer to charge. Applying a voltage (and driving a resulting current density) above a threshold value results in uniform dissolution of the silicon across the wafer, exposing a new, smooth silicon layer underneath (this process is known as *electropolishing).* Below the threshold voltage (and current density) necessary for electropolishing the silicon does not oxidize uniformly across its surface. Rather, certain areas are preferentially oxidized and dissolved, resulting in the growth of channels, or pores, into the wafer (Figure 3).

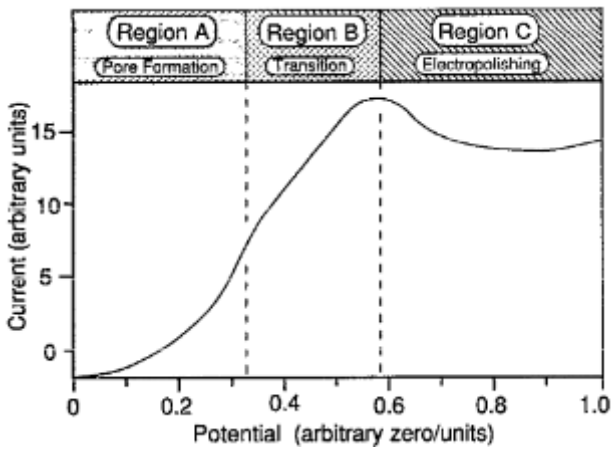

Figure 3: Characteristic Potential vs. current density curve for anodization of Si, showing regimes of pore-formation and electropolishing[13].

The exact mechanism driving preferential dissolution at the pore tips at limited applied voltages has been disputed and investigated in depth, and a number of models have been proposed to explain the phenomenon. It has been found that varying anodization conditions (including applied voltage, composition and concentration of the electrolyte, orientation and surface roughness of the silicon wafer, etc.) leads to significant differences in properties such as average pore diameter, inter-pore spacing, pore concentration, and shape of pores (branched vs. straight channel). Pores with diameters from less than 2 nm to greater than a micron have been fabricated using the anodization method[14].

Anodization therefore allows for easily fabrication of por-Si films on Si wafers. Freestanding, three dimensional porous silicon structures have been fabricated via anodization of a silicon wafer, followed by lift off and fracture of the porous film to yield particles[15] (Figure 4). However, control over the shape and size of particles formed via mechanical fracture of a film is extremely limited. Furthermore, the use of applied currents with HF-bearing solutions makes integration of the anodization method with

silicon-on-insulator platforms difficult. Thus, while anodization therefore offers great flexibility with respect to the size and geometry of pores formed in silicon wafers, it is nevertheless fundamentally limited to the formation of two-dimensional porous films on a silicon wafer.

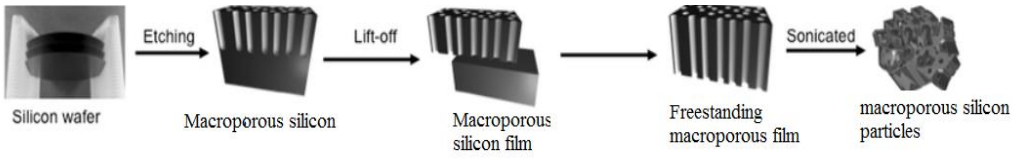

Figure 4: Fabrication of freestanding por-Si particles via liftoff and fracture of anodized film.

1.4 Metal Assisted Chemical Etching

In the late 1990's and early 2000's, interest in silicon nanostructures grew rapidly (see Figure 1). Various micro- and nanostructures of silicon have been fabricated and studied, including nanowires, tubes, spheres, belts, opals, and complex waveguides (Figure 4). Numerous bottom-up (i.e. VLS, CVD, MBE, laser ablation, etc.) and top-down (advanced lithography and etching) methods have been developed for the fabrication of silicon nanostructures.

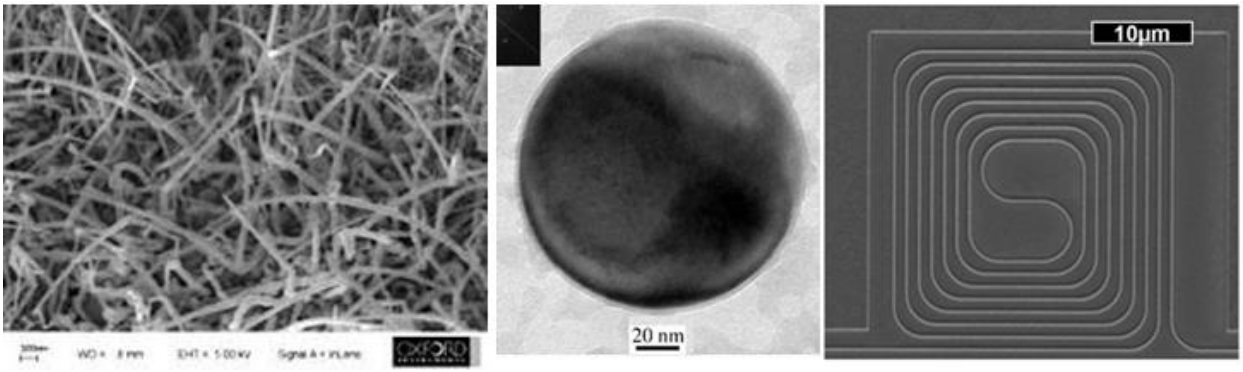

Figure 5: A variety of silicon micro- and nanostructures have been fabricated including nanowires[16], nanospheres[17], and waveguides[18].

Most of these fabrication methods yield dense silicon structures. Methods for the direct growth of porous silicon nanostructures are limited. In 2009, a pair of papers

published in *NanoLetters* reported the direct synthesis of porous silicon nanowires (p-SiNWs) via a top-down method known as *metal assisted chemical etching* (MACE)[19,20]. In a typical MACE process (Figure 6), a single crystal silicon wafer is coated by a layer of discontinuous or discrete particles of a noble metal (normally Au or Ag). The coated wafer is then immersed into a solution containing hydrofluoric acid and an oxidizing agent (generally either H_2O_2 or HNO_3). The metal particles act as a catalyst for silicon oxidation, causing the silicon directly in contact with the metal to oxidize much more rapidly than the exposed silicon. Etching of the oxidized silicon atoms in HF results in the downward growth of channels and the production of aligned nanowires.

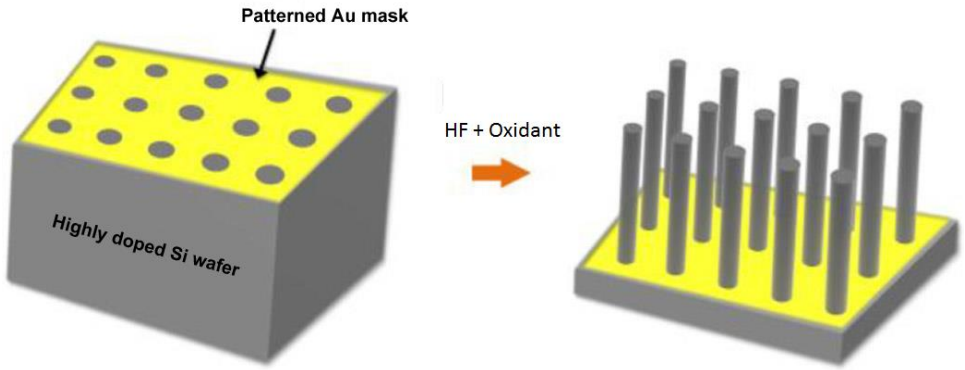

Figure 6: Overview of typical MACE process[21].

If there is an excess of silver in the solution, silver nanoparticles will nucleate on the sidewalls of the nanowires, and there will be some lateral etching into the walls of the nanowires to create pores within the nanowire structure (Figure 7). Porous silicon nanowires can thus be formed using metal assisted chemical etching if the concentration of silver in the solution, the concentration of the oxidant and electrolyte, and the resistance of the silicon wafer are carefully controlled.

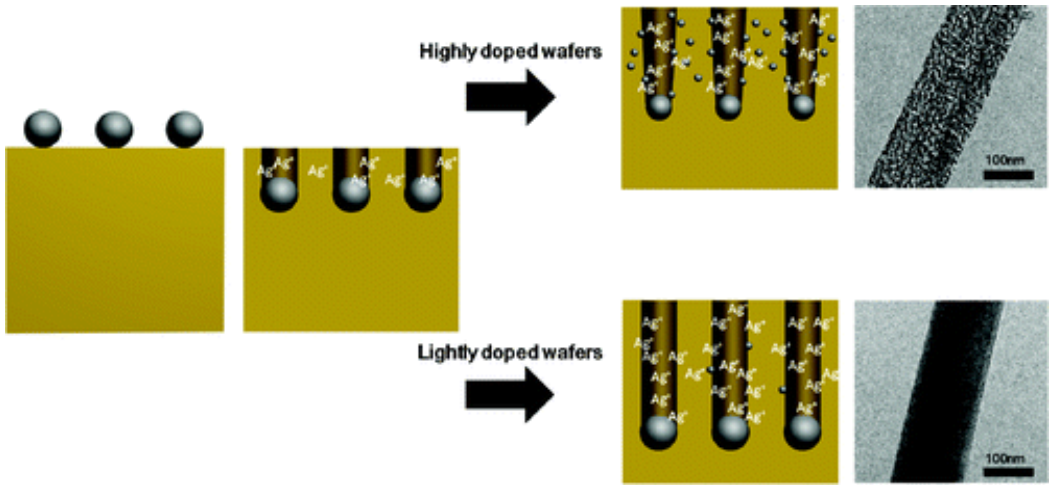

Figure 7: Mechanism of porous nanowire fabrication via metal assisted chemical etching. Porosity is only observed for highly doped silicon[22].

While the mechanism behind the MACE process is certainly interesting and the method has been shown to work quite well for fabrication of highly doped porous silicon nanowires on silicon substrates, the technique is nevertheless limited: the mechanism works only with highly doped silicon (even slight changes in doping levels have been shown to inhibit pore formation) [22], it is compatible only with silicon substrates (and not, for example, freestanding structures or nanostructures on conductive substrates, which are desirable for battery applications), and it is limited to formation of porous nano*wires* and cannot be used to generate other porous structures.

1.5 Formation of Porous Materials via Selective Leaching

Selective leaching reactions, also sometimes referred to as *dealloying* reactions when used for metals, are a class of reactions which have been utilized to fabricate porous particles or films of various compositions. In selective leaching reactions, an initial multicomponent solid material is synthesized which consists of the base material along with some sacrificial component. This initial material is then subject to reaction

conditions during which the sacrificial component will react and leave the solid (either as an aqueous solution or gaseous product) while the base material is inert. Porosity may be generated in the free volume which was occupied by the reacted element. Hence, the sacrificial component is *selectively leached* from the starting material to produce a porous solid consisting only of the inert component.

$$\mathbf{2NiAl_3(s)} + 6NaOH(a) + 18H_2O(l) \rightarrow 6Na[Al(OH)_4](a) + 9H_2(g) + \mathbf{2Ni(s)} \qquad (1.1)$$

Selective leaching methods have been reported for a variety of systems. High surface area porous nickel, known as Raney nickel since its discovery by Murray Raney in 1926[23], can be prepared by selective leaching of the aluminum in aluminum-nickel alloys (reaction 1.1, solid phases shown in bold) and has become a standard catalyst in organic chemistry[24]. Modifying either the amount of aluminum in the starting alloy composition or the reaction conditions has been shown to have a large effect on the activity of the resulting porous nickel[25,26].

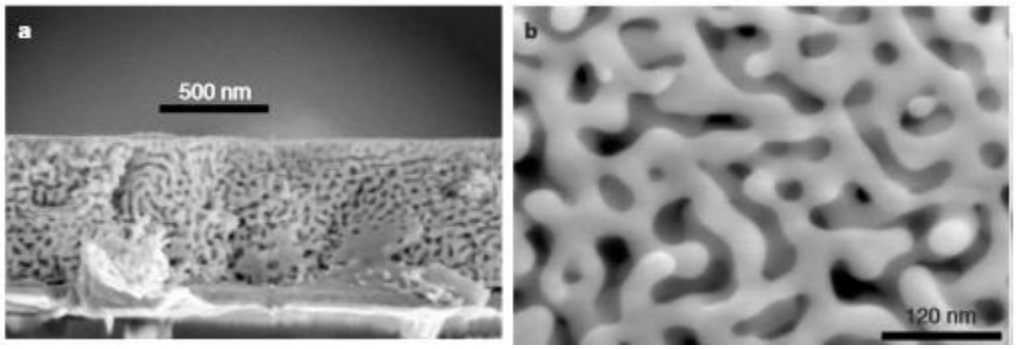

Figure 8: Cross-section and top-down view of porous gold film formed via selective leaching of silver from an Au-Ag alloy[27].

Analogously, porous gold has been reported via leaching of Cu-Au or Ag-Au alloys in nitric acid[28] (Figure 1); porous copper via leaching of Cu-Zr alloys in hydrofluoric acid[29]; and porous platinum via leaching of Cu-Pt alloys in sulfuric acid[30]. Selective leaching reactions are not limited to synthesis of porous metallic elements—both porous Al_2O_3 and SiO_2 have been prepared via treatment of a variety of silicate materials in acidic or basic solutions (for example, treatment of kaolinite, $2SiO_2{\cdot}Al_2O_3{\cdot}2H_2O$, in KOH to remove the SiO_2 component and produce porous Al_2O_3)[31,32,33,34]. Table 2 provides an incomplete list of porous materials which have been formed using a selective leaching technique.

Table 2: Overview of porous-materials which have been prepared using selective leaching techniques.

Porous Material	**Starting Material**	**Sacrificial Component**	**Leaching Method**	**Ref**
Nickel	$NiAl_3$	Al	NaOH(a)	25
Copper	$Cu_{62}Zr_{38}$	Zr	HF(a)	29
Platinum	$PtCu_3$	Cu	H_2SO_4(a) under applied voltage	30
Gold	$AuAg_3$	Ag	Nitric acid	27
Carbon	TiC	Ti	Gas phase halogenation	38
Palladium-Iron	$PdFeAl_6$	Al	NaOH(a)	35
Al_2O_3	Kaolinite ($2SiO_2{\cdot}Al_2O_3{\cdot}2H_2O$)	SiO_2	KOH (a)	31
SiO_2	Vermiculite ($3MgO{\cdot}Al_2O_3{\cdot}2SiO_2{\cdot}4H_2O$)	MgO, Al_2O_3	HCl(a)	36

Selective leaching reactions are also not limited to *aqueous dissolution* of the less noble-component in an acidic or basic solution. One selective leaching method that has received significant recent interest is **carbide-derived-carbon (CDC)**. CDC describes porous carbon which is formed via selective extraction of metal atoms from a metal carbide[37]. The extraction is achieved via elevated temperature reaction with a halide gas, during which the metal forms a gaseous metal halide and leaves porous-carbon as the only remaining solid phase (reaction 1.2)[38].

$$\mathbf{TiC(s)} + 2Cl_2(g) \rightarrow TiCl_4(g) + \mathbf{C(s)} \quad (1.2)$$

The activity of the halide gas is controlled so that only reaction with the sacrificial component (in this case, Ti) is observed while the carbon remains inert and does not form $CCl_4(g)$. The reaction of halide gas with metal carbides has been known since the early part of the 20th century[39], however it was initially used only as a method of fabricating metal chlorides and the resulting carbon was discarded. It was not until much later that the structure of the remaining carbon was probed and found to contain substantial porosity[40,41]. Over the last decade or so, several high profile publications have investigated both methods for tuning pore sizes[42,43] and various potential applications, including as a material for hydrogen storage[44] and supercapacitors[45,46].

Selective leaching reactions are therefore attractive for several reasons: they can produce highly porous materials in a scalable and relatively simple fashion; the resulting porosity is generally open and accessible; the pore characteristics may be controllable by varying reaction conditions and starting compositions; and the shape of the resulting porous material may be inherited from the shape of the starting material before selective leaching[47,48].

1.6 Design of Selective Leaching Method for Silicon

Despite the clear interest in high surface area and porous silicon, no general selective leaching process for the formation of porous silicon with controlled shapes has been described[49]. Development of such a technique could allow for the fabrication of a number of porous silicon structures not possible with current fabrication techniques. A

process that allows for the introduction of porosity into dense silicon nanostructures is envisioned in Figure 9, and consists of a two-step procedure.

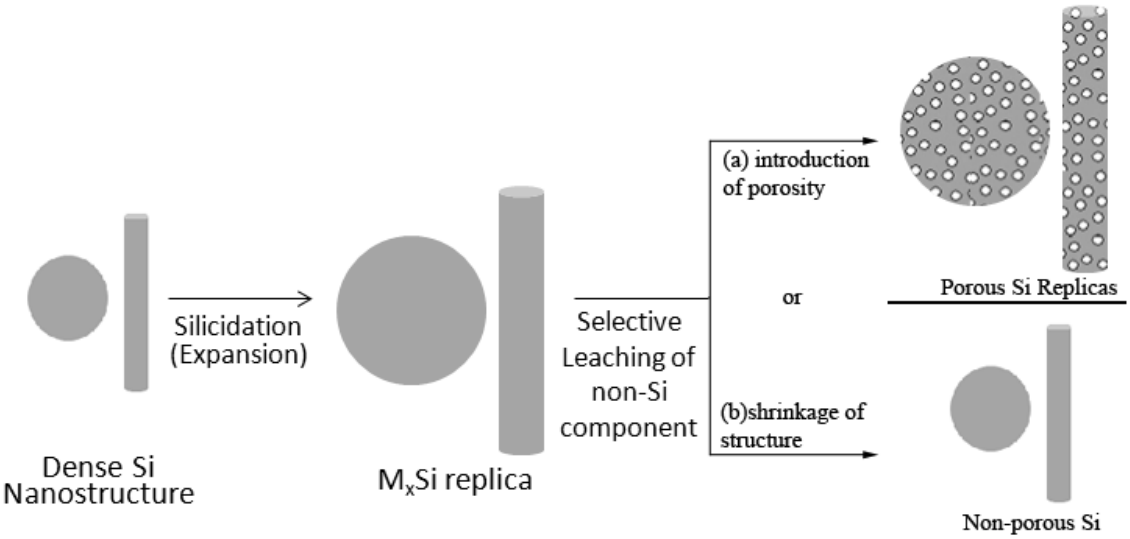

Figure 9: Schematic of post-growth porosification process based on successive silicidation and selective leaching. In the first step, conversion of a dense Si-structure into a silicide with a larger volume results in volume expansion. In the second step, selective extraction of the metal from the silicide will either result in generation of porosity or shrinkage back to the original size.

In the first step, referred to as *silicidation*, the as-grown dense silicon structure is reacted with an alloying element to produce an intermetallic silicide replica. Following formation of the silicide, the sacrificial (non-silicon) element is then extracted and elemental silicon is produced. Assuming the silicide has a larger volume than elemental silicon, the silicidation step will result in expansion of the structure while the selective leaching step will either result in shrinkage of the structure back to its original size *or* to the introduction of porosity. Pore generation is expected to occur only if, during extraction of the non-silicon element, the silicon atoms either lack sufficient mobility or are otherwise somehow inhibited from significantly rearranging. Since pores present high energy free surfaces, if the mobility of silicon atoms is uninhibited than it is thermodynamically expected that the silicon will rearrange to quench pores and push the

free volume generated by the selective leaching to the surface (i.e., shrinkage of the original structure back to its initial size, Figure 9b).

The process shown in Figure 9 and described above is referred to as a *post-growth* porosification method, since the porosity is introduced in a secondary step that occurs after complete growth of the dense silicon structure. This is in contrast to *direct growth*, as in the case of porous silicon nanowires fabricated via metal assisted chemical etching (described previously), in which the porous nanostructure is grown directly in a single step (that is, the pore-generation occurs simultaneously with growth of the desired structure). A *post-growth* method is advantageous since it decouples the nanostructure growth from the pore-generation, and therefore allows the initial dense silicon structure to be fabricated using a variety of well-established methods. The obvious disadvantage of a post-growth technique is that it requires additional steps and may have larger associated time, effort, and material costs than a direct growth method.

If porous silicon is to be obtained via selective removal of a non-silicon element from a silicide, it is essential that an appropriate sacrificial element is chosen. Selection of an appropriate silicide material requires consideration of several criteria: (1)the silicon-to-silicide conversion must be shape-preserving, so as not to lose the desired nanostructure shape upon formation of the silicide; (2)the silicide must possess a higher molar volume than silicon, so that extraction will lead to excess free volume (porosity); and (3)the non-silicon element should be much more reactive than silicon, to allow for selective removal of only the non-silicon element while retaining the silicon framework.

$$xM(g/s) + ySi(s) \rightarrow M_xSi_y(s) \qquad (1.3)$$

With respect to the first criterion, whether or not the silicidation reaction is shape preserving depends on the identity of the diffusing species during the reaction of the metal with silicon to form the metal silicide (reaction 1.3). In the beginning stages of silicide growth, an initial film of silicide will form on the surface of the silicon structure. Assuming that this initial film is dense and crack-free, in order for the reaction to proceed further either: (a) silicon atoms must diffuse outward through the silicide layer (in which case the reaction occurs at the silicide/metal interface) or (b) metal atoms must diffuse inward through the silicide layer (in which case the reaction occurs at the silicon/silicide interface). If silicon is the dominant diffusing species, shape preservation is **not** expected. Rather, voids will be generated due to the outward diffusion of silicon to the silicide/metal interface (known as the Kirkendall effect[50]) and, in the ideal case, the silicide structure will be the *inverse* of the original silicon structure (i.e., silicon nanowires will become silicide nanotubes and silicon spheres will become hollow silicide shells[51]). Only if the metal atom is the dominant diffusing species will shape preservation (accounting for volume expansion) potentially be observed after complete silicidation.

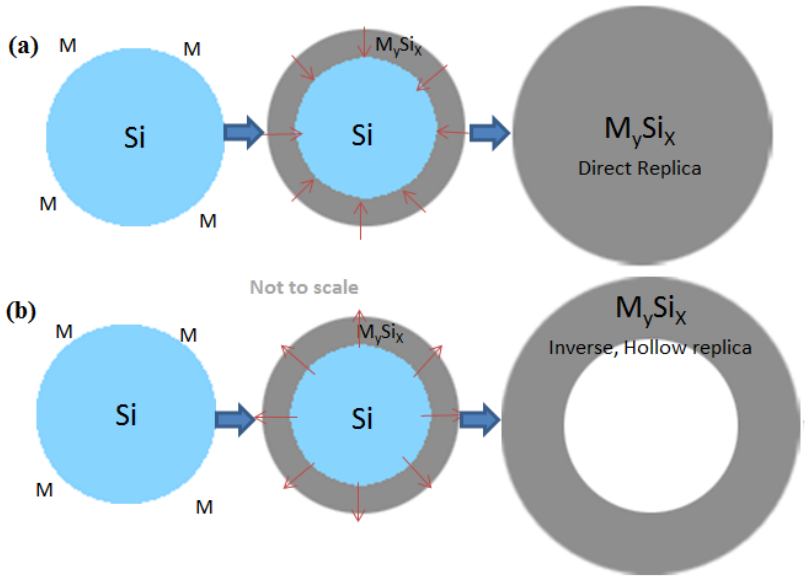

Figure 10: After some initial reaction, a dense metal silicide film forms on the Si surface. For further reaction to proceed, either (a) metal atoms must diffuse inward, in which case a direct replica may be expected, or (b) Si atoms must diffuse outward, in which case an inverse replica is possible.

The dominant diffusing species for a number of silicides has been identified via either inert marker experiments or isotope ratio studies. Inert marker experiments are used to determine at which interface silicide growth occurs, and this information can then be used to identify the diffusing species. In isotope ratio studies, the examination of isotope distributions through a grown silicide thin film can be used to identify the diffusing species—since heavier isotopes diffuse at a different rate than lighter isotopes, the mobile species is expected to show a spatial distribution of isotopes while the immobile species will show no spatial separation of isotopes. In general the diffusing species for growth of a silicide with formula M_xSi_y depends on the ratio of x/y[52]. If x/y is greater than 1 (for example, Ni_2Si) then the metal (Ni, in this case) is generally the dominant diffusing species; if the x/y ratio is less than 1 (for example, $TiSi_2$) then silicon is generally the diffusing species; for compounds in which x/y equals 1, it is difficult to

predict. Note that this is only a general guideline, not a strict rule, and several counterexamples have been reported[53].

The second criterion is that the silicide must possess a larger molar volume than elemental silicon. A "perfect" selective leaching reaction can be defined as one in which the non-silicon element is completely removed while the silicon atoms remain completely immobile (to ensure that there is no shrinkage of the silicon backbone). The maximum theoretical porosity (in volume percent) obtained for a perfect extraction process of a metal *M* from a silicide with the formula M_xSi_y is:

$$P = 1 - \frac{y V_1}{V_2} \qquad \text{Eq. 1.4}$$

where V_2 and V_1 represent the molar volume of the silicide and silicon (V_{molar}=12.1 cm^3/mol)[54], respectively. Since reaction of silicon to form a silicide involves the *addition* of metal atoms to elemental silicon, it seems intuitive that conversion of silicon to a metal silicide would lead to volume expansion. Likewise, since selective leaching involves *the removal* of atoms from a silicide to form silicon, intuition suggests that extraction of metal atoms from a silicide should generate free volume. However, this is not always the case. One mole of $CoSi_2$ (V_{molar} =23.5 cm^3/mol)[55], for instance, actually has a *smaller volume* than two moles of elemental silicon (24.2cm^3). Selective extraction of cobalt atoms from $CoSi_2$, therefore, would theoretically be expected to lead to a slight expansion of the structure and not generation of free volume.

In general, silicides with a higher mole fraction of the metal relative to silicon (i.e., a higher x/y ratio in a silicide with the formula M_xSi_y) are expected to have larger molar volumes and therefore to yield higher porosities after extraction. For example,

porous silicon formed via extraction of iron from FeSi ($V=13.8\ cm^3/mol$)[56] has a maximum theoretical porosity of a modest 12% whereas extraction from Fe_2Si yields a maximum theoretical porosity of 46%. Among silicides with similar metal to silicon ratios, molar volumes of the silicide tend to scale with the covalent radii of the metallic element. For example, Co (atomic radius=126 pm) and Ni (atomic radius=124 pm) form the silicides Co_2Si and Ni_2Si of similar molar volumes 19.67 cm^3/mol and 19.65 cm^3/mol respectively, while Pd (atomic radius=139 pm) forms the silicide Pd_2Si with a molar volume of 25.13cm^3/mol[57,58]. Therefore, in order to maximize the theoretical porosity which can be generated via selective leaching, a silicide should be chosen with a high metal to silicon ratio (≥ 1) and a metallic element with a relatively large atomic radius.

The third criterion, and perhaps the most restrictive, is that the metal atoms in the silicide must be less noble under some reaction conditions than the silicon atoms. The shape preserving conversion of silicon structures into silicide replicas (the first step in Figure 9) has been demonstrated previously for a variety of silicides, including NiSi, PtSi, and CoSi [59]. However, since the metal in these silicides is generally less reactive than elemental silicon, these materials are likely not suitable for selective leaching. Any attempt to either dissolve the metal or to otherwise react the metal would likely lead to simultaneous dissolution or reaction of the silicon atoms and ultimately loss of the structure.

With respect to these criteria, an attempt was made to rationally select an appropriate silicide material which could potentially allow for the generation of substantial porosity upon selective leaching of the sacrificial element. Group I and group II silicides were considered the most promising candidates due to their high reactivity

relative to silicon and their large atomic radii. Group I elements and group I silicides tend to react vigorously in water and humid air to yield hydrogen gas, with the heat of reaction often being sufficient to ignite the resulting hydrogen (reaction 1.5)[60]. As a result, both the group I elements and silicides require extensive handling and safety precautions, which excludes their use in a practical and facile selective leaching process.

$$Na_2Si + H_2O \rightarrow H_2(g) + Na_2SiO_3 \qquad (1.5)$$

Group II elements (the alkaline earth metals) and their corresponding silicides, on the other hand, are relatively stable in both water and air for extended periods of time (the metals will corrode over time if left in air, but do not present an imminent safety hazard) and can be handled using standard laboratory practices. Alkaline earth metals have relatively large atomic radii, and dimetal silicides (M_2Si) have been reported for all group II elements except radium[61]. For Mg_2Si growth, magnesium has been identified as the diffusing species[62], fulfilling the first criterion discussed previously regarding shape preservation during silicidation; for the other alkaline earth silicides no studies to identify the mobile species have been conducted, but the metal is most likely the diffusing species based on stoichiometric trends discussed previously. Table 3 reveals the properties of the three alkaline earth silicides Mg_2Si, Ca_2Si, and Sr_2Si and the maximum theoretical porosity of silicon that can be obtained via extraction of the metal from the respective metal silicide.

Table 3: Relevant properties of selected alkaline earth metal silicides

Formula	Molar Volume (cm^3/mol)	Theoretical porosity of silicon produced by selective extraction of metal from metal silicide (assuming no shrinkage upon extraction)
Si	12.1	N/A
Mg_2Si	39.5	69%
Ca_2Si	49.9[63]	76%
Sr_2Si	59.8[64]	80%

1.7 Conversion of Si-Nanowires into Group II Silicide Replicas

Based on the criteria necessary for porosity generation via selective leaching (discussed in the previous section), alkaline earth metals were considered the most appropriate candidates as sacrificial elements in a potential selective leaching reaction to form porous silicon. Conversion of as-grown, dense silicon structures into group-II silicide replicas (the first step in Figure 9) can be accomplished via either a solid/solid silicidation or a gas/solid silicidation. In a solid/solid reaction, the silicon structure is coated with a layer of the desired metal by physical vapor deposition to create a diffusion couple which is then annealed at elevated temperature to drive the silicidation reaction (Figure 11a). In a gas/solid reaction, the silicon structure is heated under an atmosphere containing metal vapor at a partial pressure sufficient to drive the silicidation reaction, resulting in nucleation and growth of the silicide phase and ultimately conversion of the Si structure into a silicide replica (Figure 11b).

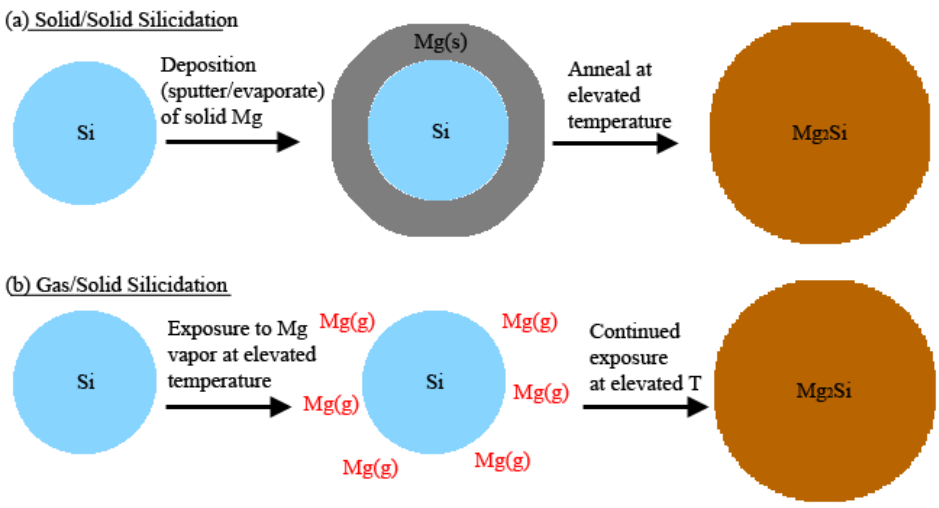

Figure 11: Schematic of (a) a solid/solid silicidation reaction, and (b) a gas/solid silicidation reaction.

Since the solid/solid reaction first requires deposition of the metal onto the silicon structure, it requires access to a physical vapor deposition (PVD) system. Uniform coverage of a deposited layer using PVD is often limited by geometric constraints. E-beam PVD, for instance, is considered strictly a line-of-sight deposition process and will deposit very little material onto areas of a structure not in direct line-of-sight of the evaporated metal. For nanostructures (for example, a collection of randomly oriented nanowires lying flat on a substrate), PVD methods will likely have significant problems depositing a uniform layer across the surface of the entire structure.

Gas/solid reactions, on the other hand, rely on gas-phase diffusion of a metal vapor and therefore have no significant line-of-sight limitations. In a gas/solid silicidation, the silicon structure is placed next to the solid metal in a closed reaction vessel, and the vessel is heated. Metal vapor is formed above the heated solid and reacts with the silicon to form the silicide. Alternatively, instead of using a closed reaction vessel, a flowing argon furnace can be utilized in which the silicon is placed downstream

from the heated metal solid. The advantages of gas/solid reactions, therefore, are that they are not line-of-sight limited and do not require access to a specialized and expensive PVD machine. The advantage of a solid/solid reaction is that the amount of metal deposited can be precisely controlled, allowing for formation of structures with a silicide shell of a desired thickness with an unreacted silicon core. Precise control over silicide thickness formed via a gas/solid reaction is difficult to achieve.

1.8 Experimental

Gas/solid reactions were utilized in an attempt to convert silicon nanowires into Mg_2Si, Ca_2Si, and Sr_2Si replicas. Silicon nanowires with an average diameter of 100 nm were grown via a VLS process onto a stainless steel substrate (courtesy Ildar Musin). An approximately 1 cm x 1 cm section of the SiNW's on stainless steel were placed adjacent to 500 mg of the solid metal source (Mg, -325 mesh, 99.8%, Alfa-Aesar; Ca granules, 99.5%, Alfa-Aesar; or Sr granules) in an iron crucible which was then welded in an argon glove-box which was constantly maintained at less than 0 ppm. The crucibles were heated at 10^{o}C/minute to temperatures between 450-800^{o}C for times varying from 30 minutes to 24 hours. After reaction, the crucibles were cooled in air and opened to remove the reacted nanowires. Excess metal stuck to the SiNW/substrate surface was removed by gently shaking or tapping the sample to remove excess powder. The nanowires were then evaluated via XRD, SEM, EDX, and TEM analysis. Silicon spheres were fabricated via previously published magnesiothermic conversion[65] of commercially available SiO_2 spheres with diameters of 150 nm and 1.5 µm (AngstromSphere, Masachusetts, U.S.A.) fabricated using a Stöber process[66] .

1.9 Results and Discussion

Only exposure to magnesium vapor produced a uniform reaction which consisted primarily of single phase silicide product, with the formula Mg_2Si. Exposure to both Ca and Sr vapor resulted in formation of several silicide species with varying compositions (Figure 12), and the reacted film was highly non-uniform (i.e., parts of the sample closer to the metal source were a different color than parts of the sample farther from the metal source) and damaged (significant spallation of the film was observed, and it was easily removed from the substrate).

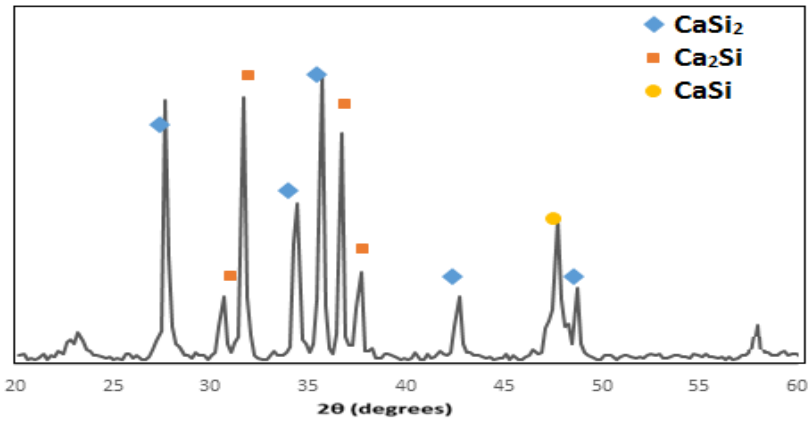

Figure 12: XRD of reaction product of reaction between silicon and calcium and 790°C for 6 hours, confirming the growth of multiple silicide phases.

Examination of phase diagrams for each system (Figure 13) reveals that, while only a single thermodynamically stable silicide phase exists for magnesium (Mg_2Si), the other group-II metals can form a number of different compounds: Ca_2Si, Ca_5Si_3, CaSi, Ca_3Si_4, $CaSi_2$ for calcium and Sr_2Si, Sr_5Si_3, SrSi, and $SrSi_2$ for strontium.

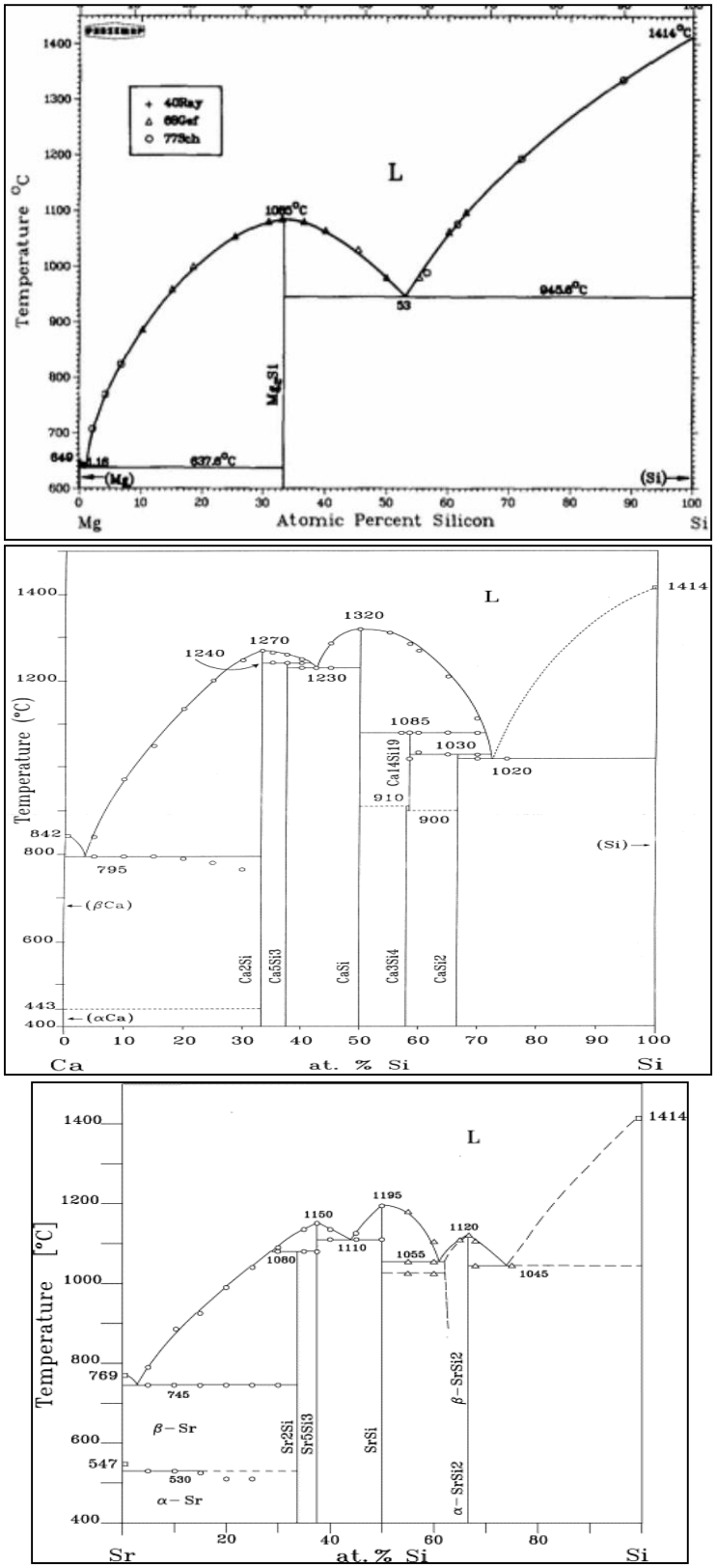

Figure 13: Binary phase diagrams for the Si –Mg[67], Si-Ca[68], and Si-Sr systems[69].

Uniform, selective growth of the M_2Si phases (M=Ca, Sr) via modifying reaction conditions (temperature and metal to silicon ratios used for reaction) could not be achieved for either calcium or strontium. In all cases, a number of silicide phases were formed. Previous investigations of solid/solid silicidation reactions involving calcium deposited onto a silicon wafer have also reported non-selective growth of several phases[70]. Due to the ability to easily fabricate single phase Mg_2Si and the difficulties fabricating single phase silicides for Ca_2Si and Sr_2Si, Mg_2Si was primarily evaluated as the sacrificial silicide for selective leaching.

The conversion of dense silicon nanowires into Mg_2Si replicas is shown in Figure 14. After reaction, characterization of the nanowire film via secondary electron microscopy (SEM), energy-dispersive X-ray spectroscopy (EDS), electron diffraction, and X-ray diffraction (XRD) confirmed that the product consists of nearly single phase, polycrystalline Mg_2Si nanowires with a very small amount of oxygen contamination (~3%). The NW structure was maintained during silicidation, although some bending of the NWs was observed due to the volume expansion associated with reaction, consistent with observations from similar silicidation reactions of NWs[71].

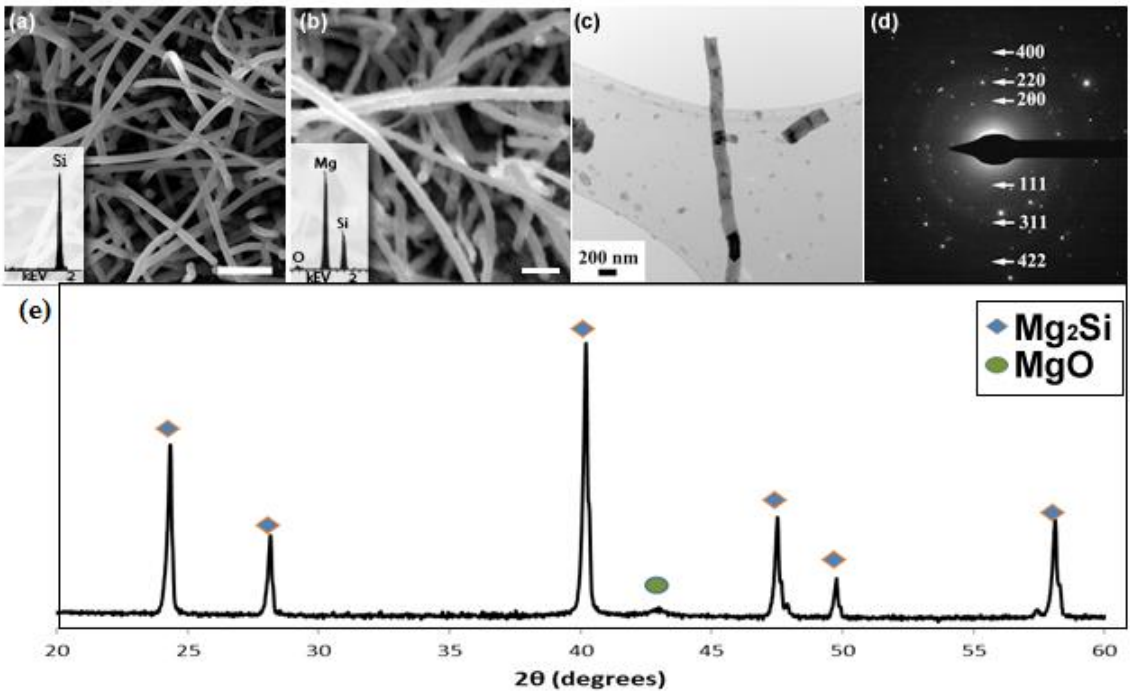

Figure 14: (a) SEM and EDX of as-fabricated Si nanowires before reaction; (b) SEM and EDX of nanowires after reaction with Mg-vapor at 500°C for 6 hours to form Mg_2Si; (c) TEM image of a single nanowire showing polycrystalline nature of nanowires; (d) Electron diffraction pattern confirming Mg_2Si as the only crystalline phase; and (e) XRD pattern of the reacted nanowires consistent with Mg_2Si. Scalebars shown for (a) and (b) are 1 μm.

X-ray diffraction (XRD) confirmed the existence of Mg_2Si and a trace amount of crystalline periclase MgO. The MgO most likely formed due to trace amounts of oxygen during the annealing process. Since electron diffraction patterns of single nanowires show no rings for magnesium oxide (Figure 14d), it was hypothesized that MgO is present primarily as foreign particles on the substrate surface (which could occur via condensation of some Mg vapor onto the substrate surface, followed by oxidation) and not as a secondary phase incorporated into the NWs. High resolution TEM was carried out on a single nanowire in order to look for evidence of secondary MgO particles in the nanowire structure itself. Even in grain boundary regions of the nanowires, no oxidized region was observed (Figure 15).

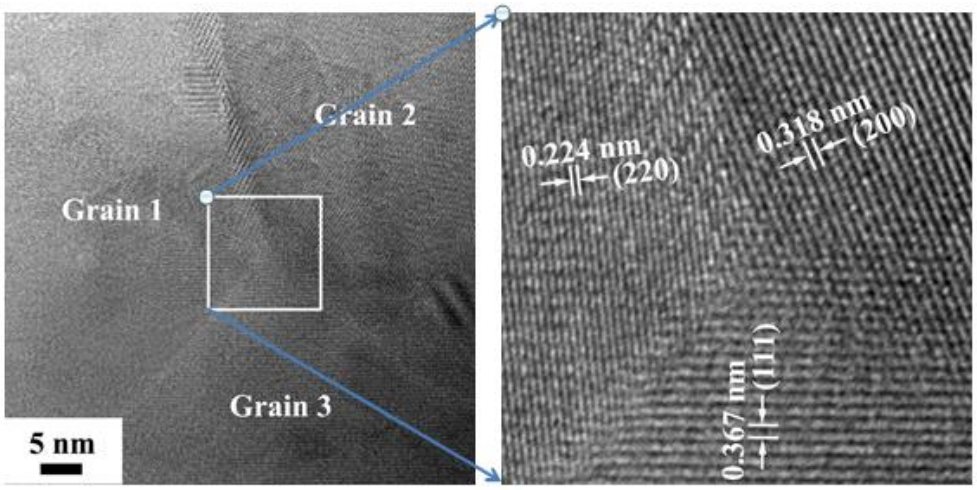

Figure 15: High resolution TEM of grain boundary region in a single Mg_2Si nanowire.

In addition to fabrication of Mg_2Si nanowires, dense Mg_2Si nanospheres (diameter ~150 nm) and microspheres (diameter ~1.5 μm) were synthesized via a similar gas-phase silicidation of silicon nano- and microspheres. For the larger spheres, some irregularities could be observed on the surface of the spheres. However, for each sample, the overall shape of the structure was clearly maintained after formation of Mg_2Si (Figure 16), accounting for volume expansion.

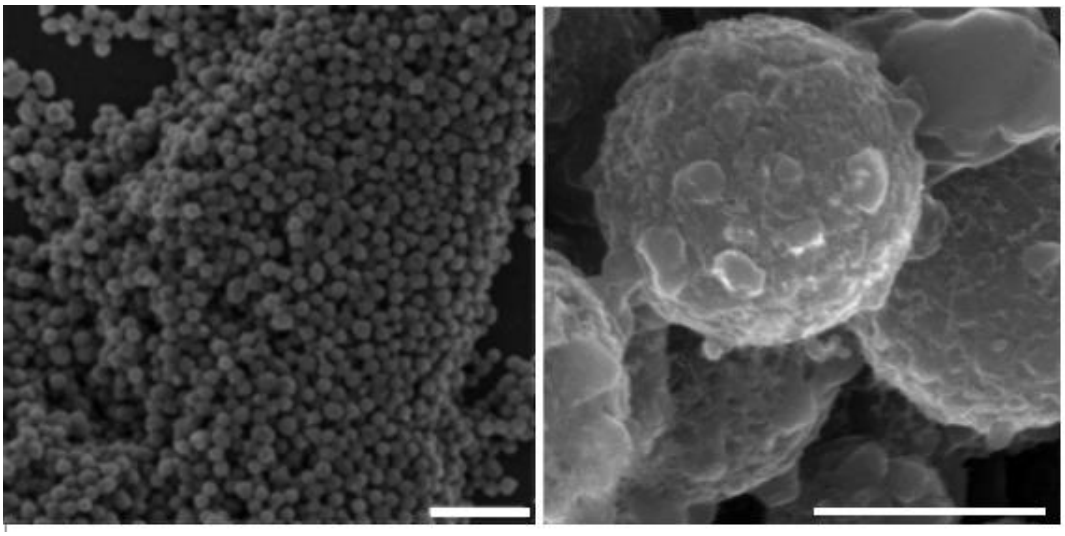

Figure 16: Magnesium silicide (Mg_2Si) nanospheres (left) and microspheres (right), fabricated via gas/solid silicidation of silicon templates. A 10:1 molar ratio of Mg:Si was utilized, and the reaction was carried out at 575ºC for 8 hours. Scalebars are 1 µm.

1.10 Selective Extraction of Magnesium from Mg2Si

In the previous sections, dense silicon structures were converted into magnesium silicide replicas. The conversion of Si nano- and micro-structures into Mg_2Si replicas represents the first step of the porosification process outlined in Figure 9. Subsequent extraction of the magnesium atoms from these Mg_2Si structures may allow for the fabrication of highly porous silicon replicas. The next chapter explores various methods which may allow for selective extraction of magnesium from Mg_2Si. In order to obtain porous silicon from magnesium silicide, it is necessary to selectively extract the magnesium atoms from Mg_2Si while minimizing loss or shrinkage of the silicon atoms (the second step inFigure 9). In the following sections, several techniques are evaluated as potential methods to selectively leach Mg from Mg_2Si. After identifying reaction conditions in which magnesium can be selectively removed from Mg_2Si, the complete conversion of dense Si-nanowires into porous Si-nanowires is demonstrated. The

versatility of the process is demonstrated by fabrication of porous silicon nanospheres and microspheres of various sizes.

1.11 Halide-Based Selective Leaching of Mg from Mg_2Si

As discussed previously, selective leaching reactions have been utilized as a means to fabricate a variety of porous materials. In many of the previously designed processes, the selective leaching step is accomplished via dissolution of the less noble component in an acidic or basic solution (see Table 1). Analogous to these previously reported selective leaching proccesses, it was noted that magnesium dissolves quickly in nearly all acids (except those with which it forms an insoluble salt, i.e. HF), while silicon is relatively stable in non-oxidizing acidic solutions[72]. Therefore, the dissolution of magnesium from Mg_2Si was attempted in a variety of acids (hydrochloric acid; acetic acid; phosphoric acid; etc.). In all cases, a vigorous reaction was observed , usually accompanied by small sparks, which resulted in the formation of an amorphous white or gray solid (Figure 17).

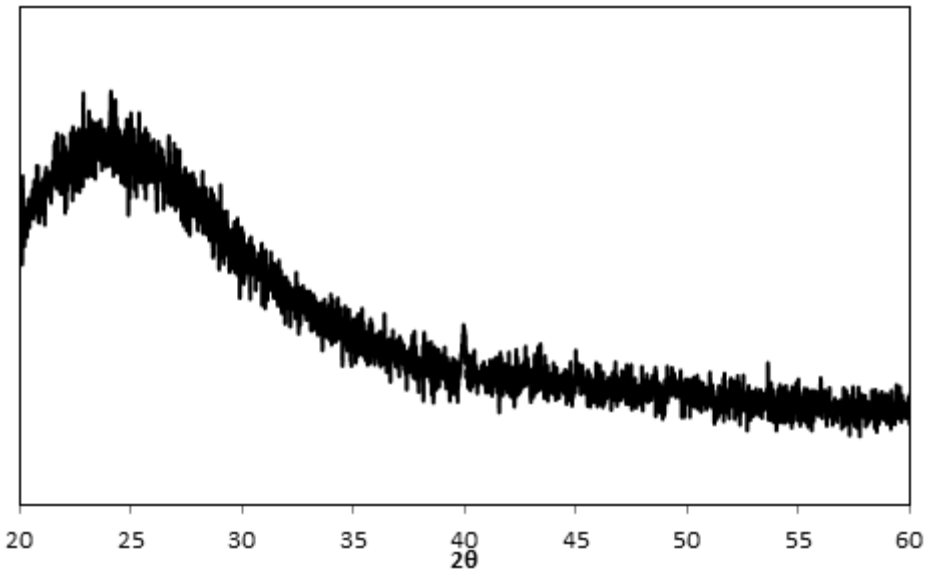

Figure 17: XRD of gray product produced via reaction of Mg_2Si in 1M HCl for 20 minutes; reaction produced visible sparks.

Based on previous reports in literature[73], the initial reaction of Mg_2Si in acidic solutions is known to yield silane gas, which then spontaneously combusts in air to form silicon dioxide and water.

$$Mg_2Si(s) + 4HCl(a) \rightarrow 2MgCl_2(a) + SiH_4(g) \qquad (2.1)$$

$$SiH_4(g) + O_2(g) \rightarrow SiO_2(g) + 2H_2O(l) \qquad (2.2)$$

Although elemental silicon does not react vigorously with hydrochloric acids, the intermetallic compound Mg_2Si *cannot* be treated as simply a mixture of unoxidized Mg^0 and Si^0 atoms. Rather, the magnesium contributes electron density towards the silicon atom and the Mg-Si bond shows some ionic character. *Ab initio* studies into the electronic structure of Mg_2Si[74] reveal that the true oxidation states of each atom are $Mg^{+0.9}{}_2Si^{-1.8}$ (treating the bond as fully ionic would yield $Mg^{+2}{}_2Si^{-4}$). The additional electron density associated with the silicon atom in Mg_2Si as compared to unoxidized silicon makes it highly reactive in acids, and makes selective leaching in acidic solutions impossible. In

order to avoid silane gas formation as shown in reaction 2.1, the leaching process was attempted in a variety of non-aqueous solutions consisting of hydrogen chloride gas dissolved in aprotic solvents (for example DMF-HCl or Diethylether-HCl). However, in all cases silicon was etched along with magnesium, and *selective* dissolution of magnesium (without dissolution of silicon) was not achieved.

Following the failure of aqueous acid-based selective leaching, several gas-phase leaching methods were explored. A flow through-furnace was constructed to allow for reaction between Mg_2Si and Cl_2/Ar gas mixtures. Reaction of magnesium silicide powder with dry chlorine gas (analogous to metal extraction processes used to produce carbide derived porous carbon) gas at elevated temperature resulted in a white solid contained only magnesium, chloride, and only trace amounts of silicon (the product was assumed to be $MgCl_2$, although no further characterization was carried out, Figure 18). No elemental silicon or other silicon-containing solid product was produced from the reaction.

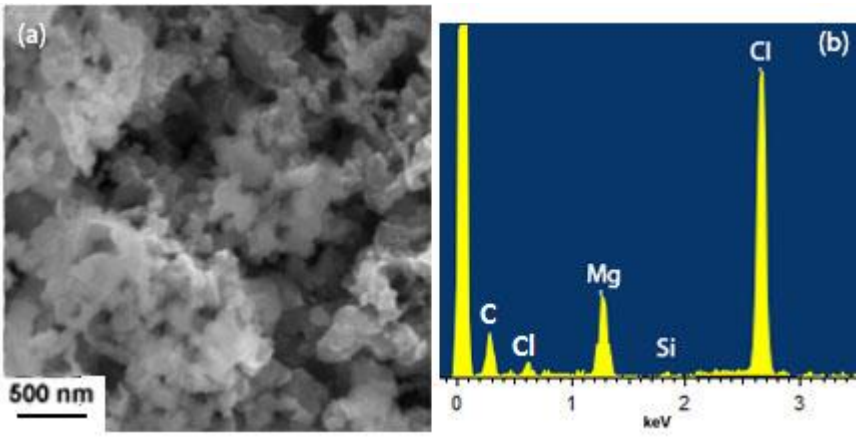

Figure 18: (a) SEM and (b) EDX of residual solid after reaction of Mg_2Si spheres with excess chlorine gas.

The loss of silicon upon reaction of Mg_2Si with Cl_2 gas is almost certainly due to formation of volatile silicon tetrachloride gas (in the case of reaction with dry chlorine) or silane gas (in the case of reaction with hydrogen chloride gas).

$$Mg_2Si(s) + 4Cl_2(g) = 2MgCl_2(s) + SiCl_4(g) \quad (2.3)$$

$$Mg_2Si(s) + 4HCl(g) = 2MgCl_2(s) + SiH_4(g) \quad (2.4)$$

The reaction between silicon and chlorine gas to form silicon tetrachloride gas (reaction 2.3) is favorable at all temperatures up to approximately 4,000^{o}C (well above the boiling point of silicon, 3265^{o}C)[78]. The reaction between **carbon** and chlorine gas to form carbon tetrachloride gas, on the other hand, becomes unfavorable above approximately 400^{o}C[78]. This explains why selective leaching of carbides with chlorine gas to yield solid porous carbon is possible at moderate temperatures (T>~400^{o}C), but selective leaching of silicides with chlorine gas does not yield solid silicon at any temperature. A thermodynamic equilibrium composition diagram for the Mg-Si-Cl system was produced using the HSC chemistry software suit and database[78]. The diagram, which assumes isobaric pressure of 1 atm and excess Cl_2 gas (Cl_2:Mg_2Si molar ratio of 4:1) is shown in Figure 19. As can be seen, solid silicon is not the favorable product at any reaction temperature, precluding the use of Cl_2 gas for selective leaching of Mg from Mg_2Si.

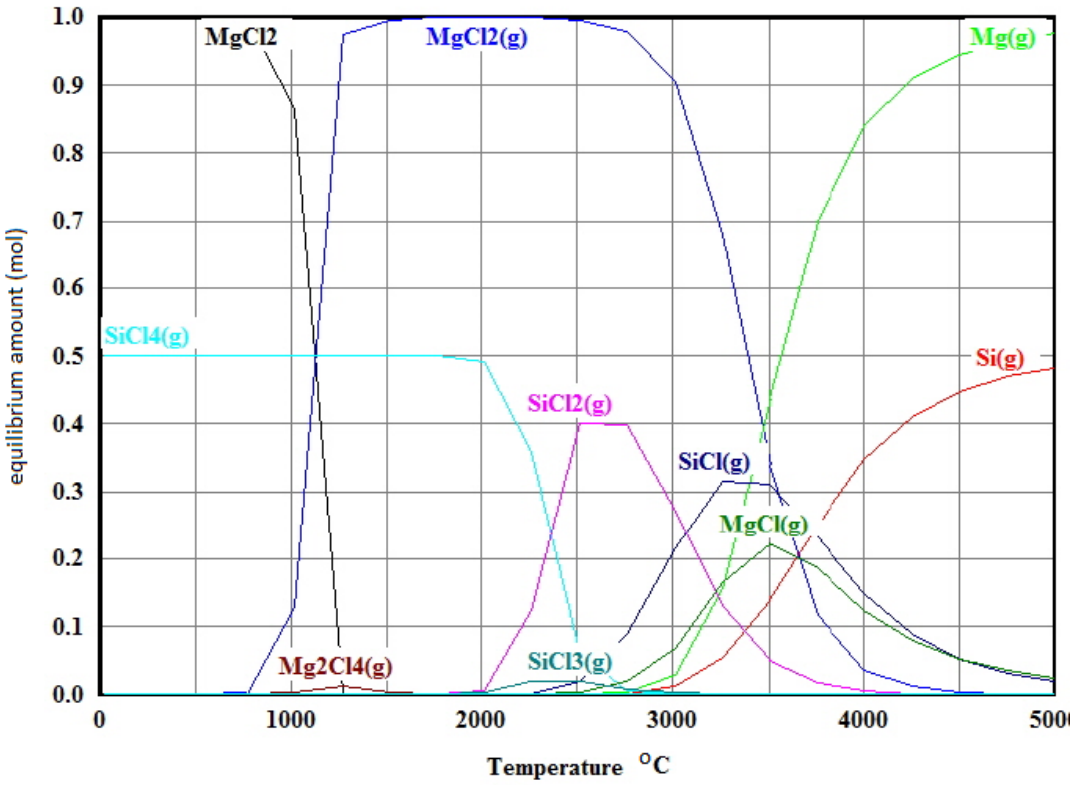

Figure 19: Calculated thermodynamic equilibrium composition diagram for the Mg-Si-Cl system, assuming excess Cl_2 gas.78

The only way to prevent the formation of $SiCl_4$ vapor is to significantly limit the activity of the chlorine species. One way to accomplish this is to use metal halides (M_xCl_y) as the reactive vapor instead of dry chlorine gas. Previous publications[75] have demonstrated the metathesis reaction between magnesium silicide and various gaseous metal-chlorides (i.e., $FeCl_3$) to yield magnesium-halides, metal silicides, and unoxidized metal (reaction 2.5).

$$Mg_2Si + (^4/_y)M_xCl_y(g) \rightarrow 2MgCl_2 + M_zSi + (4\ ^x/_y - z)M \qquad (2.5)$$

The possibility of a metathesis reaction between Mg_2Si and metal halides was thus considered as a potential route for selective magnesium extraction from magnesium silicide. Note that in reaction 2.5, a secondary metal silicide, and not elemental silicon, is

formed from the reaction. It was hypothesized that, if a metal halide was chosen whose metal does not form any compounds with silicon, then elemental silicon may potentially be produced. In order to avoid formation of a secondary metal silicide, aluminum chloride ($AlCl_3$) was chosen as the chloride species since aluminum forms no compounds with silicon (Figure 20)[76].

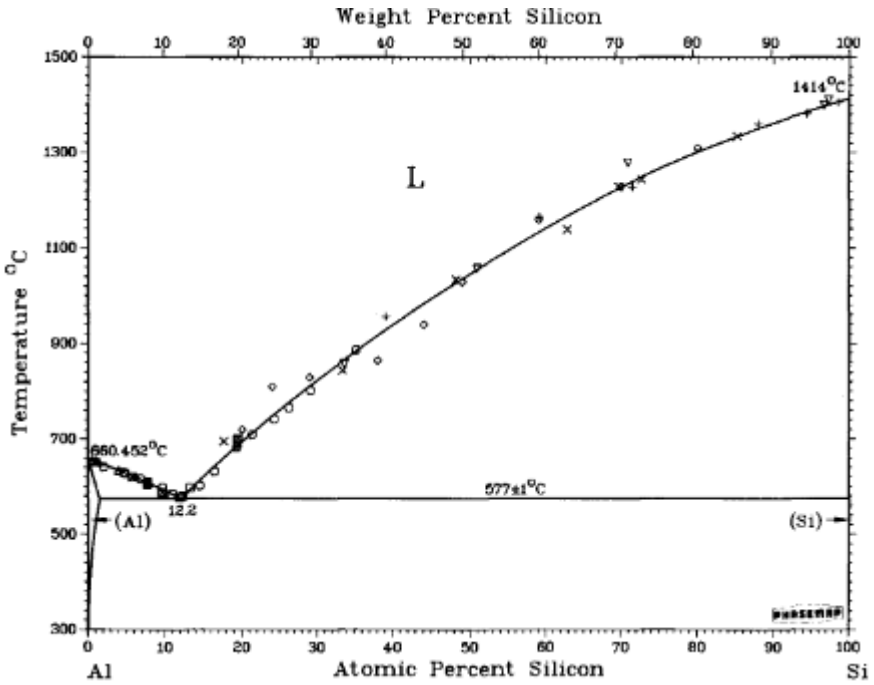

Figure 20: Phase diagram for the Al-Si system[76].

The reaction between $AlCl_3$ with Mg_2Si is thermodynamically expected to form elemental silicon, $MgCl_2$, and aluminum as shown in reaction 2.6. The reaction between aluminum chloride and silicon to form silane gas is unfavorable (reaction 2.7).

$^4/_3AlCl_3 + Mg_2Si \rightarrow 2MgCl_2 + {}^4/_3Al + Si \qquad \triangle G^{o,473K} = -269kJ \qquad (2.6)$

$^4/_3AlCl_3 + Si \rightarrow SiCl_4(g) + {}^4/_3Al \qquad \triangle G^{o,473K} = +43.7kJ \qquad (2.7)$

$Al_2Cl_6(g) + {}^3/_2Si \rightarrow {}^3/_2SiCl_4(g) + 2Al \qquad \triangle G^{o,473K} = +66kJ \qquad (2.8)$

Assuming unity activities for all solid products, an $AlCl_3$ activity of 2E-23 is necessary to drive reaction 2.6 at 200°C. The low sublimation temperature of $AlCl_3$ ($T_{sublimation}$ of ~200°C to form Al_2Cl_6 vapor)[78] should therefore allow for for relatively low reaction temperatures, which are desirable in order to minimize the mobility of silicon atoms during magnesium extraction. The $MgCl_2$ and Al products of reaction 2.6 can be trivially dissolved by washing with acidic solutions to yield presumably porous silicon as the only solid phase product. The formation of silicon tetrachloride gas cannot be avoided completely—sublimation of $AlCl_3$ at 200°C will yield an Al_2Cl_6(g) activity of ~1 and $AlCl_3$(g) activity of 1.5E-3, which, based on the $\triangle G^o$ value for equations 2.7 and 2.8, will lead to a cumulative equilibrium activity of $SiCl_4$ gas of 8.3 E-21. Thus, while not avoided entirely, only a very small amount of silicon tetrachloride gas formation is thermodynamically possible and, especially if the reaction is conducted in a closed system, only a very small amount of solid silicon may be lost via formation of volatile silicon tetrachloride. The thermodynamic equilibrium composition diagram for the Mg_2Si-$AlCl_3$ system is shown in Figure 21, assuming isobaric conditions of 1 atm and a 3:1 molar ratio of $AlCl_3$:Mg_2Si. The diagram demonstrates that at all temperatures below 550°C, the equilbrium species are solid silicon, aluminum, and magnesium chloride.

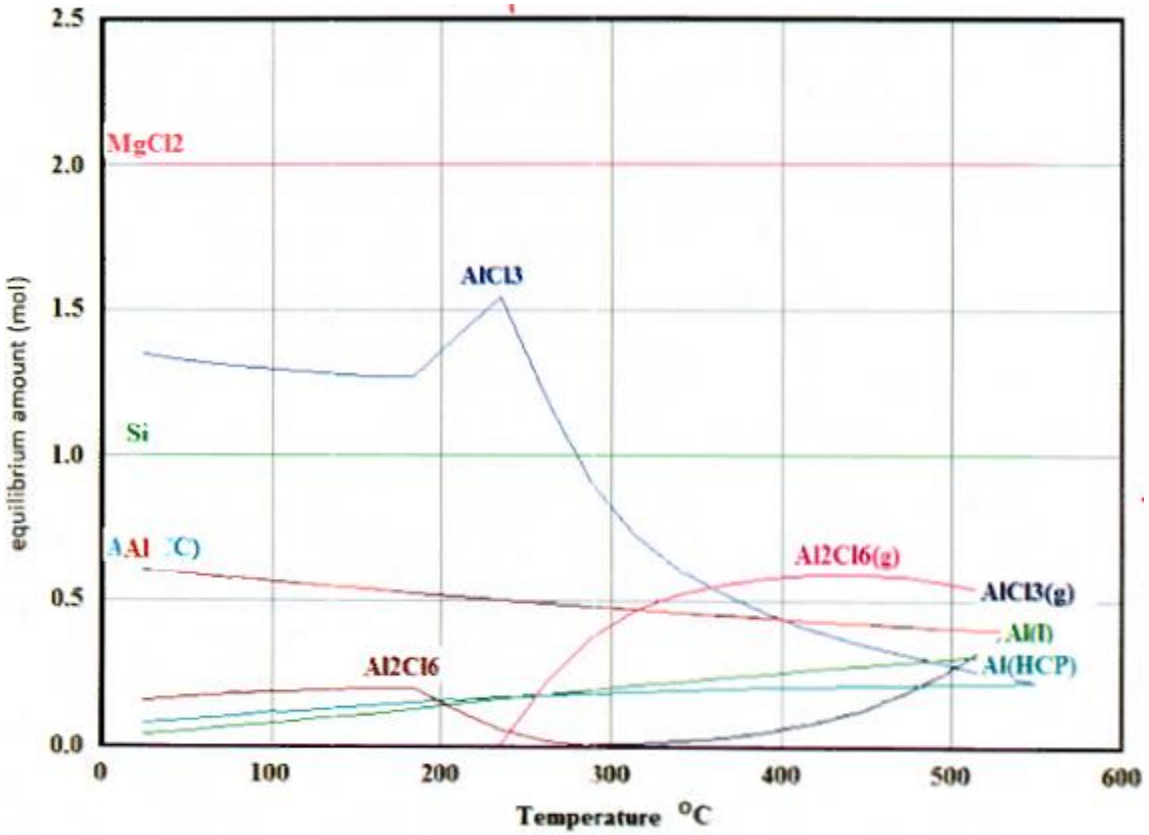

Figure 21: Thermodynamically calculated equilibrium composition diagram for the Mg_2Si-$AlCl_3$ system[78].

In order to evaluate the reaction between $AlCl_3$ and Mg_2Si, an excess of anhydrous $AlCl_3$ (Alfa-Aesar, 95+%) was mixed with bulk Mg_2Si powder (Alfa-Aesar, 99.5%) in an 8:1 weight ratio (4.6:1 molar ratio), sealed in a Pyrex glass ampoule under vacuum, and placed in a preheated furnace at temperatures between 180°C-240°C. The ampoule then cooled and the remaining solid product was stirred in deionized water for 45 minutes. The residual solid after washing was saved for analysis. The supernatant liquid was collected and evaporated to yield an off-white powder, identified as hydrated $MgCl_2$ (Figure 22).

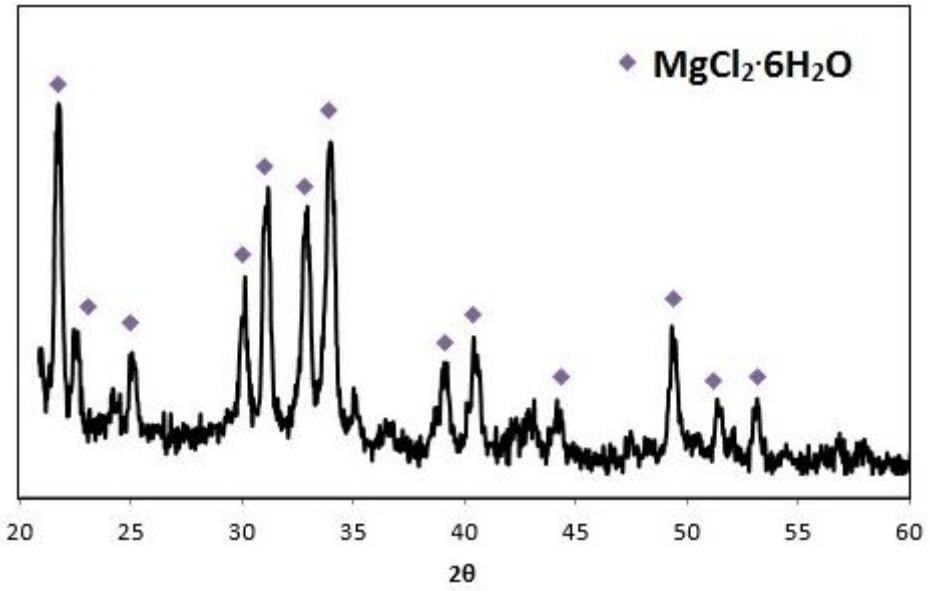

Figure 22: XRD of water-soluble product after reaction of $AlCl_3$ and Mg_2Si under static vacuum at 220°C for 2 hours.

XRD analysis of the residual solid after washing with water confirmed the presence of aluminum and elemental silicon (consistent with reaction 2.6) of very small crystal sizes (mean size 18 nm). Removal of aluminum via washing in hydrochloric acid (1M, 3 hours) yielded a brown powder which XRD analysis confirmed was nanocrystalline silicon (Figure 23).

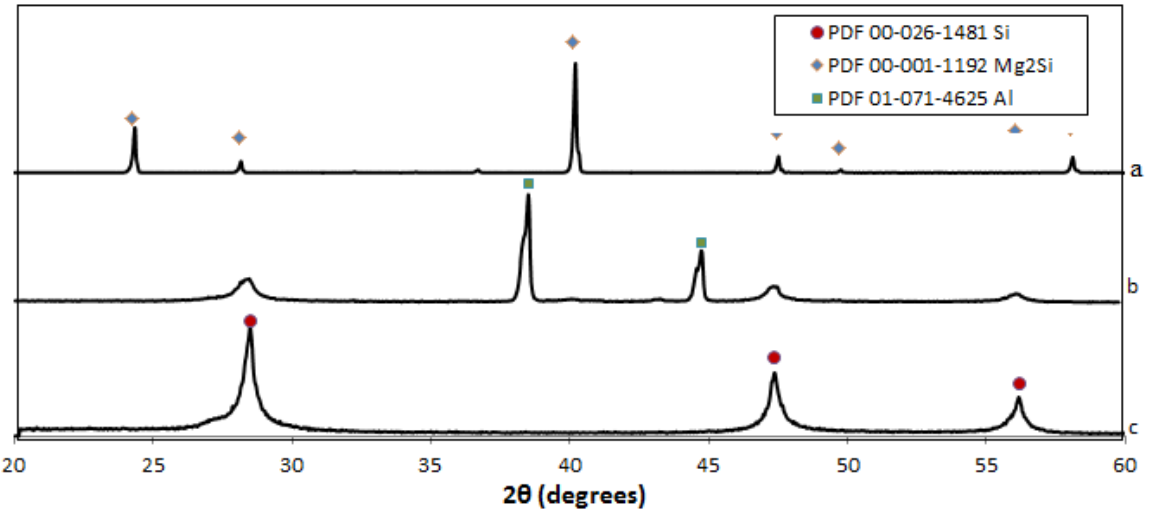

Figure 23: XRD patterns demonstrating conversion of (a) starting Mg_2Si powder into (b) intermixed aluminum and silicon after reaction with $AlCl_3$ vapor, and (c) nanocrystalline Si after subsequent HCl treatment to remove Al.

Specific surface area, mean pore size, and pore size distribution were evaluated using nitrogen adsorption measurements with Brunauer-Emmett-Teller (BET) theory to estimate total specific surface area and density functional theory (DFT) to estimate pore sizes and pore size distribution. BET analysis of silicon powder obtained after the reaction and acid wash revealed a relatively high specific surface area of 242 m^2 g^{-1} (Figure 24a), compared with 6.1 m^2/g^{-1} before porosification, suggesting that a large amount of porosity was retained during magnesium extraction. DFT calculations confirm that a majority of the surface area can be attributed to micropores. Pore size distribution determined by DFT reveals a mean pore size of 0.9nm with a relatively narrow distribution and a small quantity of secondary pores with sizes of 1.3nm and 2.9nm (Figure 24b). There is almost no porosity present above 4 nm. Comparison of specific surface area and pore size distribution for the starting silicon powder (no treatment) and the resulting porous silicon powder after treatment confirms that the porosification process results in a dramatic increase in surface area and microporosity.

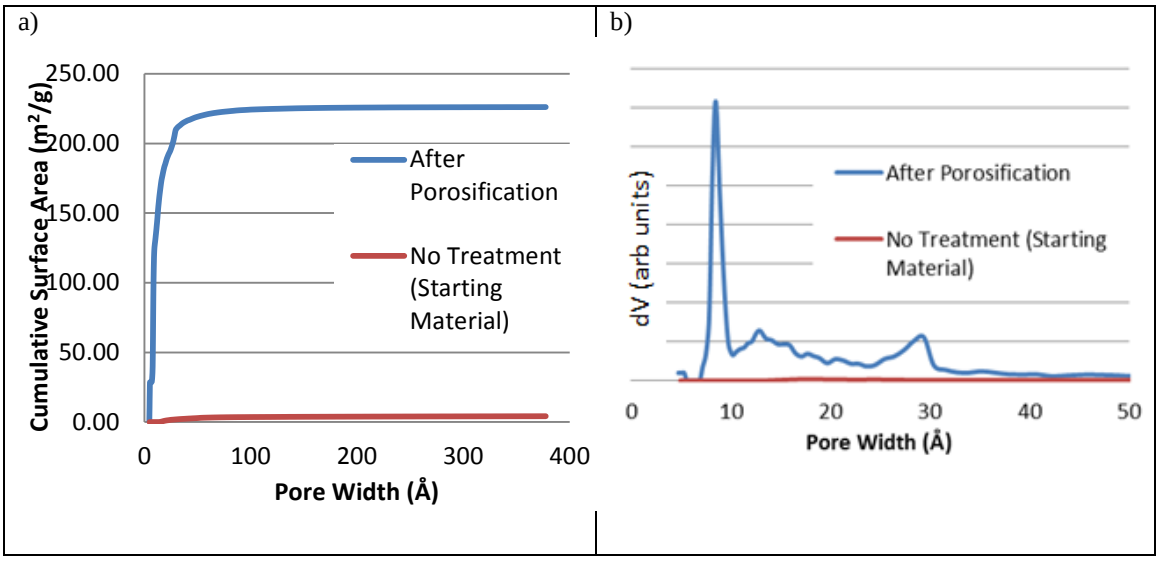

Figure 24: (a) DFT cumulative specific surface area showing starting Si powder before treatment (red) and microporous powder after treatment (blue); and (b) DFT pore size distribution showing absence of porosity before treatment (red) and introduction of microporosity with mean size of ~0.9 nm after treatment (blue). Reaction was carried out at 220°C for 2 hours, and Al was removed with HCl (1M) treatment for 3 hours.

Unfortunately, the morphology of the particles was *not* well preserved during the extraction. Reaction with Mg_2Si nanowires resulted in significant loss of structure after exposure to aluminum chloride gas (Figure 25).

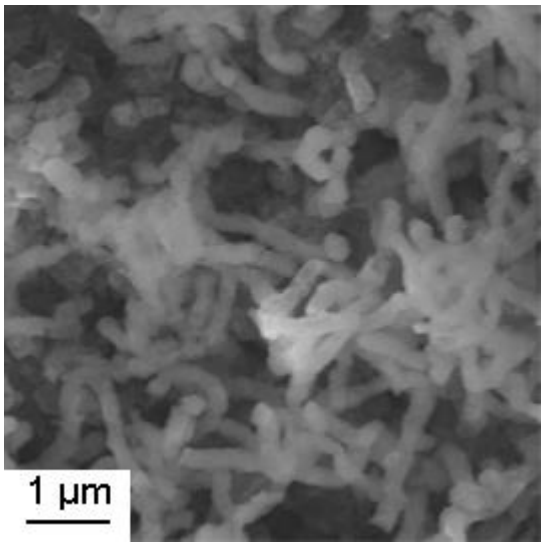

Figure 25: SEM image of product after reaction of Mg_2Si nanowires with $AlCl_3$. While some nanowire features can be observed, significant loss of morphology was evident.

The loss in morphology is likely due to initial, local formation of silicon tetrachloride vapor which then quickly reacted with Mg_2Si or Al to form elemental silicon. Either reaction pathway is thermodynamically possible, would be consistent with the final products observed via XRD, and would explain the loss of morphology.

Reaction Pathway #1:	$\triangle G^0_{rxn}$ (473K)	Reaction Pathway #2:	$\triangle G^0_{rxn}$ (473K)
$^1/_2Mg_2Si + 4/_3AlCl_3 \rightarrow MgCl_2 + 4/_3Al + {}^1/_2SiCl_4(g)$	-85.83kJ	$Mg_2Si + {}^8/_3AlCl_3 \rightarrow 2MgCl_2 + {}^8/_3Al + SiCl_4(g)$	-85.83kJ
$^1/_2SiCl_4(g) + {}^1/_2Mg_2Si \rightarrow MgCl_2 + Si$	-225.9kJ	$SiCl_4(g) + {}^4/_3Al \rightarrow {}^4/_3AlCl_3(g) + Si$	-182.8kJ
Net: $Mg_2Si + {}^4/_3AlCl_3 \rightarrow 2MgCl_2 + {}^4/_3Al + Si$			$\triangle G^0_{rxn}(473K)$=-269kJ

1.12 Selective Oxidation of Magnesium in Mg_2Si

Due to the difficulties encountered with shape preservation during halide reactions, other selective leaching methods were desired. Reports on the behavior of bulk Mg_2Si at 600°C[77] in ambient air have indicated that the primary products of high temperature oxidation are MgO and Si, although no efforts were made to evaluate the extent of silicon oxidation (whose resulting oxide will likely be amorphous and difficult to deteect via XRD analysis). Oxidation of Mg_2Si can result in several thermodynamically favored reaction products.

Table 4: Possible reactions in the oxidation of Mg_2Si[78]

	Reaction	ΔG^o_{rxn}(900K) (kJ)	Δmass (%)
R1	$Mg_2Si + O_2(g) \rightarrow 2MgO + Si$	-938	+41.7
R2	$Mg_2Si + 2O_2(g) \rightarrow 2MgO + SiO_2$	-1685	+83.4
R3	$Mg_2Si + 2O_2(g) \rightarrow MgO + MgSiO_3$	-1724	+83.4
R4	$Mg_2Si + 2O_2(g) \rightarrow Mg_2SiO_4$	-1748	+83.4
R5	$Mg_2Si + {}^3/_2O2(g) \rightarrow 2MgO + SiO(g)$	-266	+5.08

Since MgO, but not Si, is readily soluble in acidic solutions, one intriguing pathway for magnesium extraction from Mg_2Si involves the selective oxidation of Mg_2Si to form a MgO/Si composite (Reaction R1 in Table 4), followed by an acidic wash to

remove the MgO phase. Relatively high temperatures (~600^{o}C) are needed for oxidation (compared to <250^{o}C for reaction with $AlCl_3$) and it is likely that silicon atoms at these temperatures will have sufficient mobility to rearrange significantly during the extraction process. However, the MgO phase produced during oxidation is expected to be dispersed within the silicon structure and can act as a barrier to inhibit shrinkage of the surrounding silicon framework.

An approach involving selective oxidation of Mg atoms in Mg_2Si, followed by dissolution of MgO to yield porous silicon requires that the conditions of the oxidation reaction are controlled so as to completely oxidize the magnesium atoms in the material while minimizing concurrent oxidation of silicon atoms (that is, to achieve only reaction R1 above while avoiding reactions R2-R4). Either thermodynamic control (in which the oxygen partial pressure is maintained at a level sufficient to drive reaction R1 but insufficient to drive reactions R2-R4) or kinetic control (in which the oxidation of silicon is thermodynamically favorable but kinetically limited due to reaction conditions) can be employed.

In order the thermodynamically limit reactions R2-R4 while driving reaction R1, at 900K it is necessary to maintain the oxygen partial pressure between 1E-54atm and 1E-51 atm[78]. In this range of oxygen pressures, **only** oxidation of magnesium is thermodynamically possible. Such precise control at extremely low oxygen partial pressures can be achieved using a Rhines pack[79] of Ti/TiO to establish an oxygen pressure of 1.17E-53atm at 900K. Rhines pack oxidation was carried out by sealing Mg_2Si powder along with a 1:1 molar ratio of Ti (Alfa-Aesar, 98%) and TiO (Alfa-Aesar, 99%) powder in a steel ampoule. The sealed samples were held at 625^{o}C for extended

times. After reaction, the ampoules were cooled, cut open, and the Mg_2Si powder was removed for XRD analysis. Although some oxidation of the magnesium was observed (to form MgO and elemental Si), the reaction proceeded extremely slowly. Even after 96 hrs of Rhines pack oxidation of Mg_2Si nanopowder (mean size 100 nm) at 700°C, a substantial amount of unoxidized Mg_2Si was present after reaction (Figure 26).

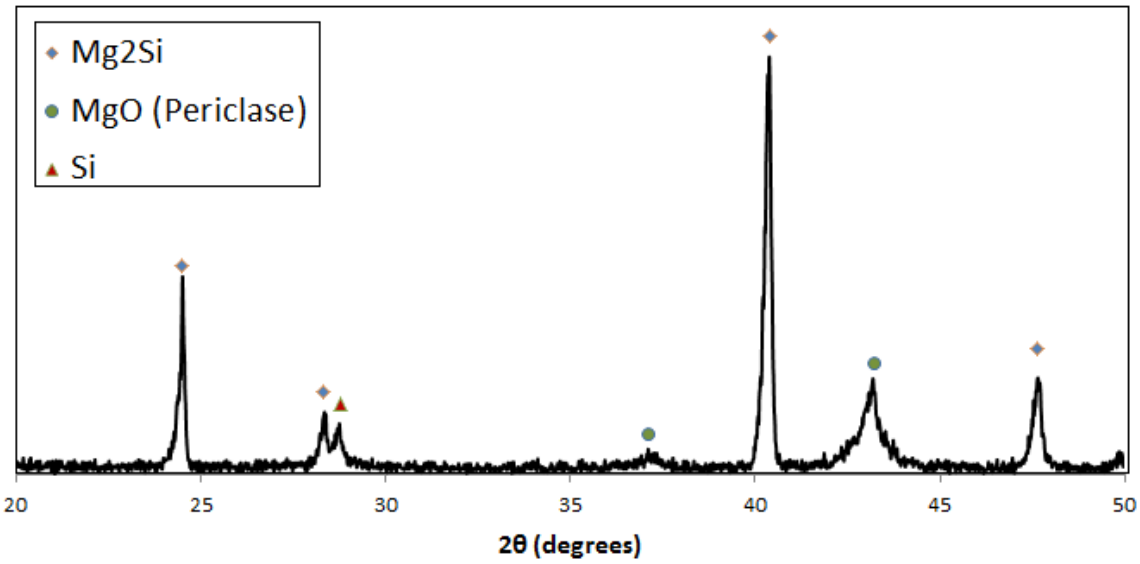

Figure 26: XRD pattern of product after oxidation of Mg_2Si nanopowder in Ti/TiO Rhines pack for 96 hours at 625°C. While some Si and MgO is observed, unreacted Mg_2Si is the primary component.

Kinetic control, in which reaction conditions (temperature and partial pressure of oxidation) are controlled so that silicon oxidation is thermodynamically favorable but minimized due to kinetic limitations, was evaluated. Oxidation of silicon at temperatures below 650°C is known to occur extremely slowly, while magnesium oxidizes readily at these temperatures. It was therefore postulated that, under correct temperatures and oxygen partial pressures, selective oxidation of magnesium could be achieved while kinetically minimizing oxidation of silicon.

In order to monitor the oxidation reaction *in-situ*, thermogravimetric (TG) analysis was used to measure the mass of oxygen uptake during the reaction at a variety of conditions. From the stoichiometry of Reaction R1 (table 1), the selective oxidation of magnesium silicide to form only MgO with no concurrent oxidation of silicon should yield a ~42% increase in mass. A larger mass gain suggests the formation of oxidized silicon species (table 1, R2-4), while a smaller mass gain suggests incomplete oxidation of magnesium. TG analysis of pure magnesium metal and similar analysis of Mg_2Si was conducted at increasing temperatures (heating rate of 10^oC/minutes) under an atmosphere of 0.2 atm O_2 and 0.8 atm N_2.

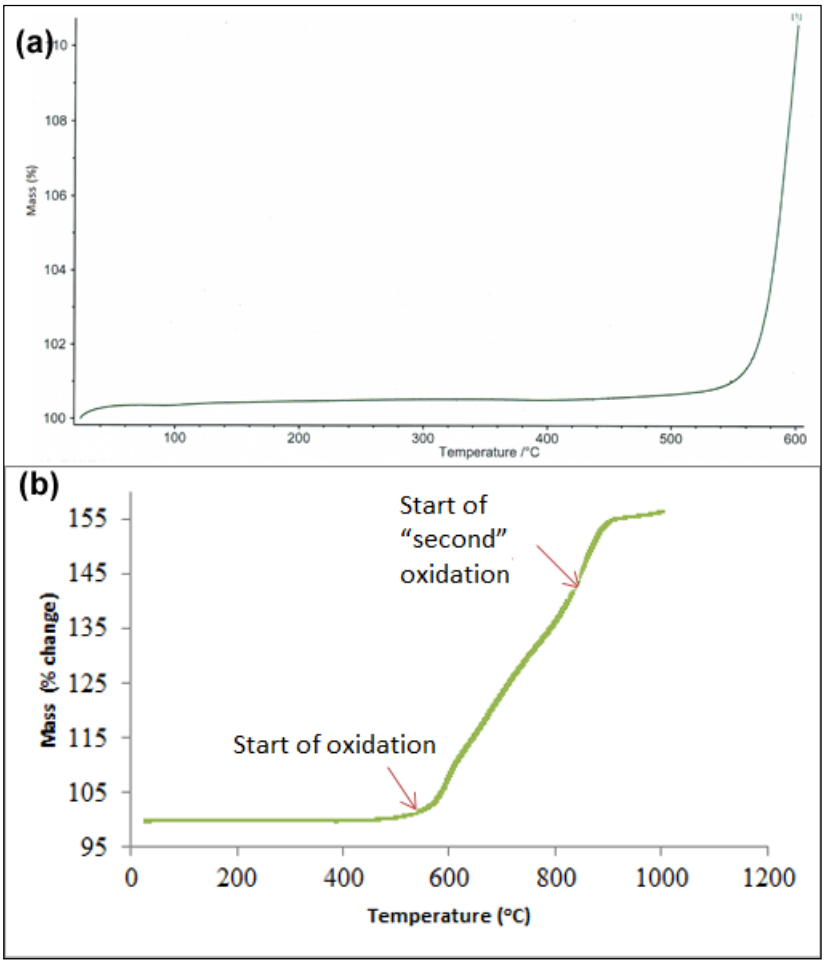

Figure 27: (a) TG analysis of pure Mg metal (Sigma-Aldrich, -325 mesh, 99%) under 20% Oxygen/80% Argon, with a heating rate of 10°C / minute, and (b) similar analysis of Mg_2Si (Sigma-Aldrich, -20 mesh, 99%).

From Figure 27a, the initial oxidation of pure magnesium metal can be observed at around 550°C, and oxidation occurs very rapidly as the temperature increases. Initial oxidation of the Mg_2Si occurs at similar temperatures (Figure 27b). At approximately 800°C, a slight change in the slope of mass gain is observed, suggesting the possible start of a second oxidation reaction. Presumably, due the first oxidation process (at T>~550°C) corresponds to rapid oxidation of magnesium while the second oxidation process (>800°C) corresponds to the onset of silicon oxidation.Once all the magnesium is oxidized, the mass gain slows significantly. However, the total mass gain is higher than

that predicted for **only** oxidation of Mg in Mg_2Si, suggesting some oxidation of silicon (which is expected given the high temperatures which were evaluated).

Based on the TG analysis shown in Figure 27, additional experiments were undertaken to examine the isothermal oxidation behavior of Mg_2Si under various conditions (Figure 28). Temperatures between 525^{o}C to 825^{o}C were chosen for isothermal oxidation studies since rapid oxidation of magnesium is expected at these temperatures. At 525^{o}C under exposure to 0.2atm of O_2, a gradual mass gain was observed which, even after extended time periods, was well below the value expected for complete oxidation of magnesium. At 625^{o}C, a rapid mass gain was observed and the total increase was consistent with the value expected for selective oxidation of only the magnesium atoms. At 725^{o}C, a similar rapid mass gain was observed. However, the total mass increase was slightly higher, indicating that, although minimal, some of the silicon may have been oxidized. At 825^{o}C, the total mass gain increased significantly, well above the value expected for complete oxidation of magnesium suggesting substantial oxidation of silicon.

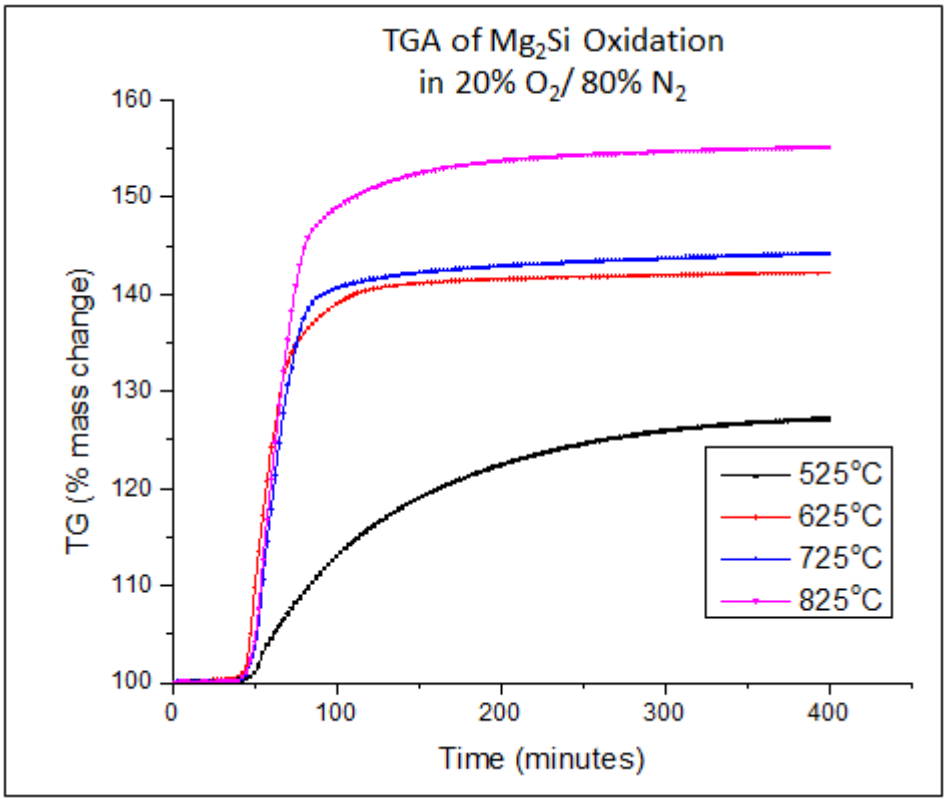

Figure 28: Isothermal oxidation of Mg_2Si at 0.2atm O2 and various temperatures.

From TG analysis, a reaction time of approximately 300 minutes at 625°C/0.2atm-O_2 was considered sufficient for complete oxidation of Mg_2Si powder while avoiding oxidation of Si. Maintaining the oxidation conditions for longer periods (up to 24 hours) resulted in no significant additional mass gain. The oxidation reaction was also monitored by HT-XRD (Figure 29, Panalytical X'Pert Pro MPD diffractometer with HTK-1200 furnace under gonio geometry) to determine in-situ the chemical identities of the products formed via oxidation at 625°C with a partial oxygen pressure of 0.2 atm. Results from HTXRD, as expected from the TGA, the main products of Mg_2Si oxidation at T=625°C and pO_2=0.2 atm are MgO and Si, and that the oxidation occurs directly with no formation of any intermediates. The decrease in Mg_2Si peaks (2Θ=24°,

27.5º, 40º) corresponds to the formation of periclase MgO (2Θ=43º) and silicon (2Θ=28º). No amorphous hump is observed in the diffraction pattern, suggesting that no significant amount of amorphous silica products is produced. Together, the TG and HTXRD data of the oxidation reaction of Mg2Si demonstrate conclusively that, given the appropriate temperature and pressure of oxygen, it is possible selectively oxidize the magnesium atoms completely while avoiding oxidation of the silicon in order to form a MgO/Si composite.

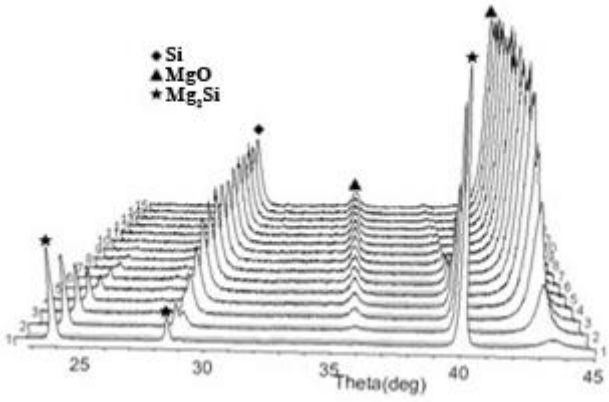

Figure 29: HT-XRD analysis of Mg2Si oxidation at 625ºC. The initial scan was collected at room temperature, while subsequent scans were collected after heating (25ºC / minute) to desired temperature. Each scan represents a 10 minute time interval.

After establishing reaction conditions necessary for selective oxidation of Mg in Mg2Si powder, the selective oxidation method was subsequently attempted using theMg_2Si nanowires fabricated in chapter 1. Mg_2Si nanowires, still on the iron substrate, were placed in a tube furnace and held in air at 625ºC for 4 hours. After oxidation, the substrate with the nanowires was removed from the furnace and an XRD pattern was collected of the oxidized nanowires. The XRD pattern confirms the complete selective oxidation of Mg_2Si to form nanocrystalline MgO and Si (Figure 30).

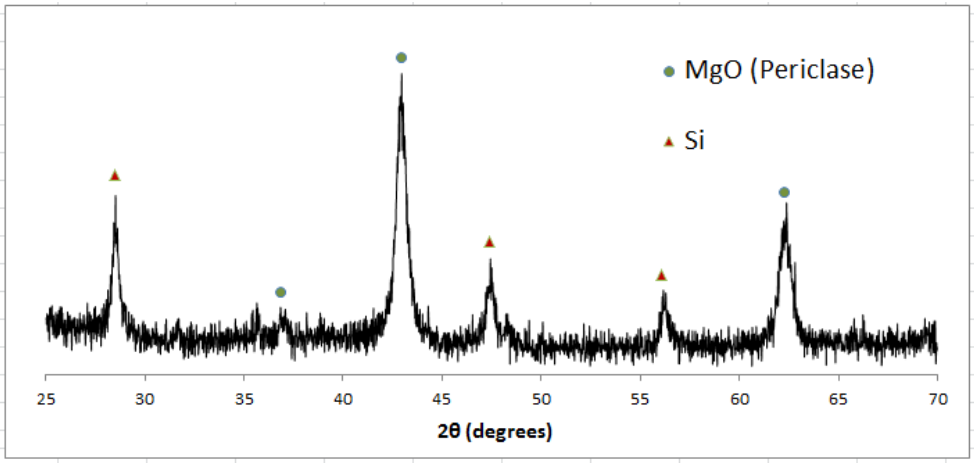

Figure 30: XRD pattern of nanowires after oxidation at 625°C for 4 hours.

Following complete oxidation of the Mg_2Si nanowires to form a MgO/Si composite, the nanowires were washed with hydrochloric acid in order to remove the MgO phase. Electron micrographs of the residual solid after MgO dissolution reveal that the resulting silicon is highly porous, and that the structure of the porous silicon is inherited from the initial dense silicon starting product (Figure 31a-c). Electron diffraction confirms that the nanowires consist of single phase, polycrystalline silicon (Figure 31d).

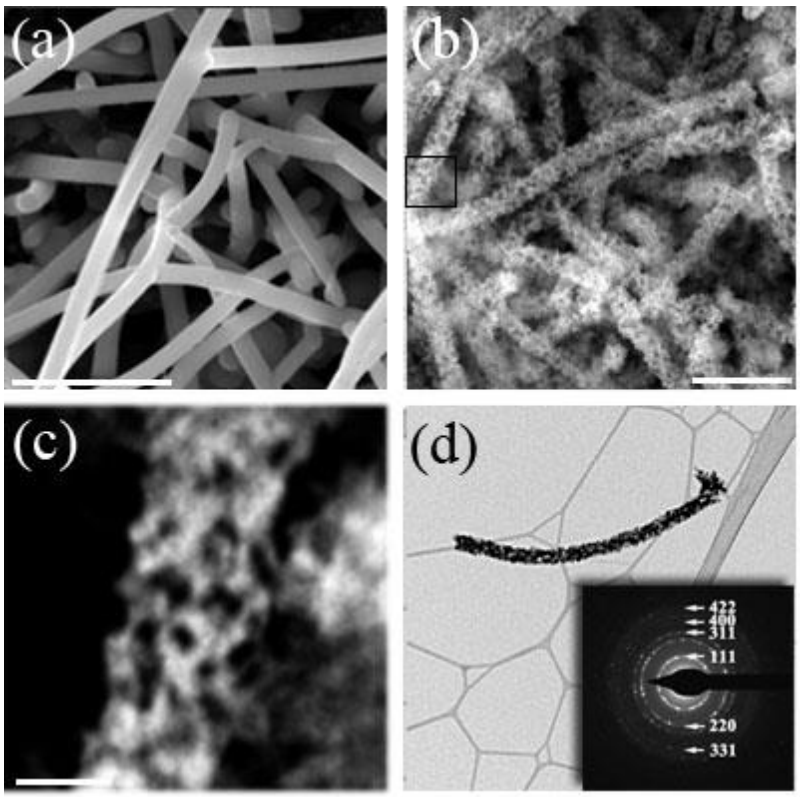

Figure 31: SEM images of (a) as grown, dense SiNW's before any reaction; (b) porous SiNW's after silicidation, selective oxidation, and dissolution of MgO; (c) higher magnification image of porous NW; (d) TEM image and electron diffraction pattern confirming single phase Si; Scalebars are 1 μm for (a) and (b), and 200 nm for (c). Selective oxidation was carried out at 625ºC for 4 hours and Mg was removed by washing with 1M hydrochloric acid for 1 hour.

Figure 31(a-d) demonstrates the complete conversion of dense silicon nanowires into porous silicon replicas. In order to examine the versatility of the porosification process to structures of various geometries and sizes, magnesium extraction via selective oxidation was attempted from the dense Mg_2Si nanospheres and microspheres fabricated in chapter 1. In both cases, magnesium extraction resulted in porous silicon structures which maintained the overall shape of the Mg_2Si (Figure 32).

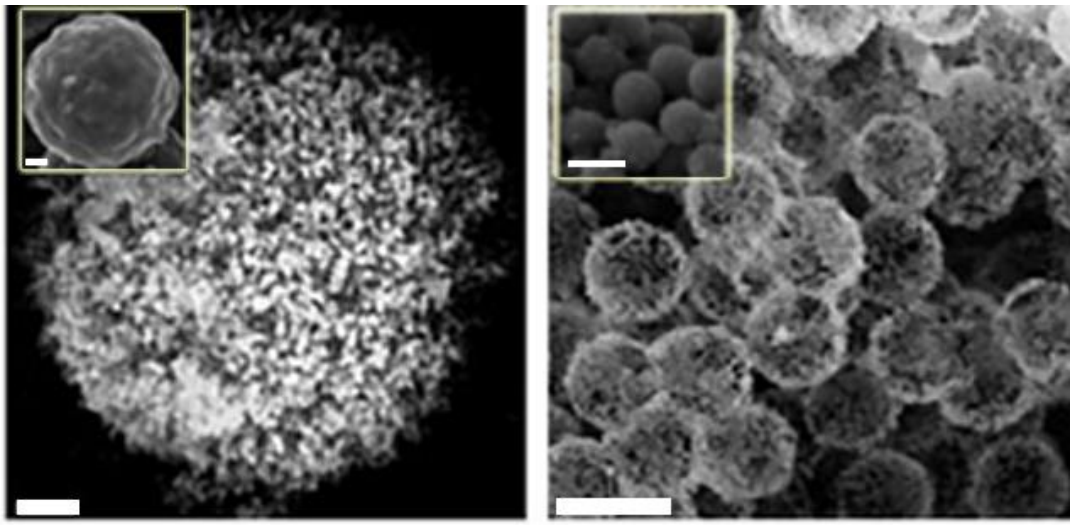

Figure 32: SEM images of porous silicon microsphere (~1.5 μm diameter, left) and nanospheres (~250 nm diameter, right) fabricated via selective extraction of Mg from dense Mg_2Si templates (insets). All scale bars are 200 nm. Selective oxidation was carried out at 625°C for 4 hours, and MgO was removed via reaction with hydrochloric acid (1M, 1 hour).

1.13 Discussion & Limitations of Selective Oxidation

In a theoretically "perfect" selective leaching process, the sacrificial component (in this case, Mg) is removed completely under conditions in which the noble component (in this case, Si) is completely immobile. From a thermodynamic standpoint, the introduction of porosity leads to a large density of high energy surfaces. If the mobility of the atoms which make up the noble component is sufficiently fast and otherwise unimpeded during selective leaching conditions, the noble component would be expected to rearrange in such a way as to minimize internal surfaces and push free volume to the exterior of the structure (i.e., shrinkage).

Selective oxidation of Mg_2Si required temperatures in excess of ~525°C. As a comparison, the crystallization of amorphous silicon has been observed at temperatures as low as 470°C and occurs rapidly at temperatures greater than ~600°C[80,81], suggesting at least moderate mobility of silicon atoms at these temperatures. During oxidation of the

Mg_2Si, an MgO phase is grown which is dispersed within the material's structure and which inhibits shrinkage of the surrounding silicon framework. The porosity is introduced into the structure when the MgO/Si composite is dissolved in acid at room temperature, when silicon atoms are essentially immobile. Nitrogen adsorption and desorption isotherms of the starting Si-powder and the resulting porous-Si fabricated via conversion to Mg_2Si and selective oxidation are shown in Figure 33. After the porosification process, a substantially larger volume of N_2 was adsorbed, and BET-analyses revealed nearly an order of magnitude increase in specific surface area (111 m^2/g after porosification) compared to the starting product (11.2 m^2/g).

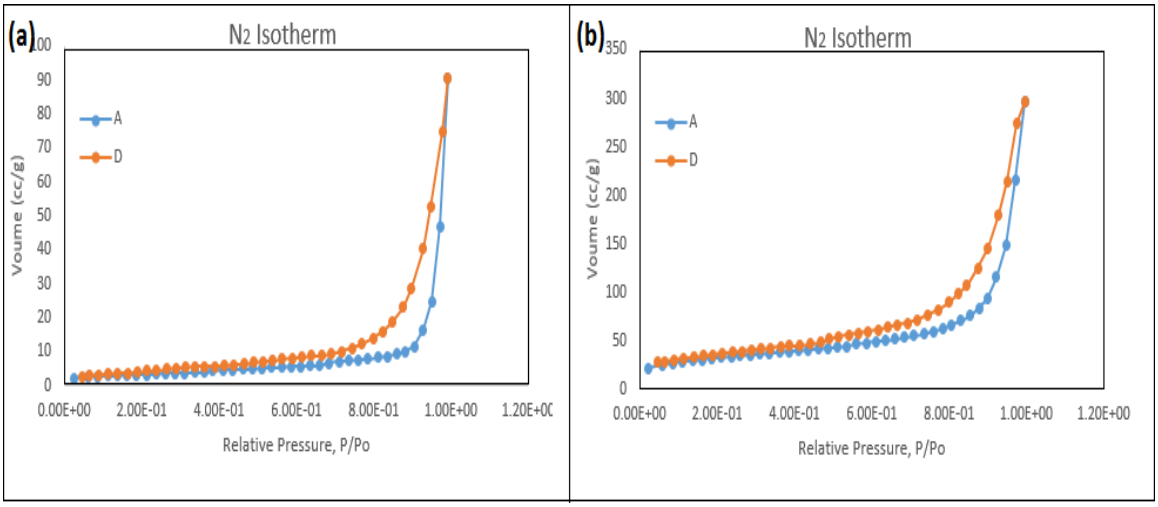

Figure 33: N2 adsorption and desorption isotherms for (a) starting Si-powder before reaction and (b) porous-Si powder produced via porosification process.

Pore-size distribution curves based on BJH desorption of the porous product revealed a broad size distribution with an average pore size of 24.8 nm (Figure 34). This value corresponds very closely with the average MgO crystallite size determined from Scherrer analysis of the XRD patterns after oxidation (approximately 20 nm).

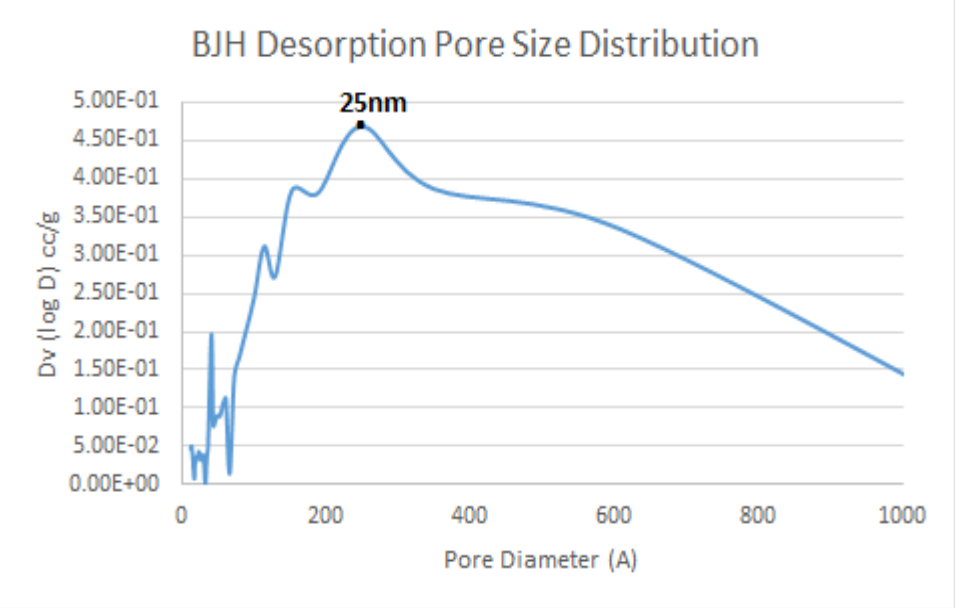

Figure 34: BJH calculated pore size distribution (based on desorption curve in Figure 33b) of porous Si produced via selective extraction of Mg from Mg_2Si.

Theoretically, control over pore sizes in the final porous-Si structure could therefore be achieved by exploiting nucleation and growth kinetics of the MgO phase during oxidation of Mg_2Si. Oxidation conditions favoring a high nucleation rate and slow growth rate of the oxide will lead to a large number of small crystallites, while conditions favoring rapid growth rates and limited nucleation will result in the formation of a smaller number of large oxide clusters. After dissolution of the oxide phase, high nucleation and low growth rates would be expected to yield a large number of pores of small sizes, whereas fast growth and low nucleation would result in a smaller number of pores with a larger average size.

In theory, adjusting both oxygen activity and temperature could affect nucleation and growth kinetics of MgO growth. High oxygen partial pressures during oxidation could result in a larger degree of supersaturation which should favor nucleation of a large

number of oxide particles within the material (leading to a large number of smaller crystallites). Low oxygen partial pressures, with limited supersaturation of oxygen in the silicide, may result in nucleation of oxide crystals at only at a few high energy sites and could lead to a smaller number of large crystallites. In order to test the effects of oxygen pressure on the resulting morphology of the MgO during oxidation of Mg_2Si, various oxygen partial pressures were examined from between 0.10 and 1 atm. Partial pressure control was achieved using two digital mass flow controllers (Netzch Intsruments LLC), one connected to pure O_2 and one connected to high-purity N_2 (AirGas), to control the ratio of O_2/N_2 flowing through the oxidation furnace. Control over the MgO crystal size could not be achieved by varying oxygen partial pressure during oxidation between 0.10 to 1 atm. This is likely due to the extremely low oxygen pressure (1E-54 atm) necessary to drive the oxidation of magnesium in Mg_2Si[78]. Even the lowest oxygen pressure evaluated (0.10 atm) was *much* higher than the pressure needed to drive the reaction, and so it was likely that a level of supersaturation necessary for nucleation of the oxide phase is easily achieved at even the lowest pressure which could be evaluated.

Another potential method of controlling pore characteristics is to vary the initial silicide composition. Extensive research into porous carbon produced via extraction of metals from a number of metal carbides (*carbide-derived-carbon*, discussed previously) has shown that even slight modification in the chemical composition of the starting carbide results in significant differences in resulting surface area, porosity, pore size, etc. While only extraction of Mg from Mg_2Si was fully evaluated in this study, there are almost certainly other silicides (especially other group II silicides, see Table 3) which satisfy the necessary criteria for use in selective leaching. It is quite likely that

modification of the silicide composition would allow for some control of pore properties in the resulting porous silicon after selective leaching. However, attempts to evaluate selective leaching of other group II-silicides (Ca_2Si or Sr_2Si) were impeded due to the existence of several binary silicide compounds and the difficulty of selectively growing only the dimetal silicide species. Recently, the single-phase growth of both Ca_2Si and Sr_2Si via gas/solid reactions was reported[82]. Although the growth was demonstrated only on Si wafers, it is possible that a similar strategy could be used to selectively grow single phase Ca_2Si and Sr_2Si nano- and microstructures for selective leaching. In addition to the use of binary group-II silicides for selective leaching, ternary silicides have been identified in the Mg-Ca-Si system ($Mg_2Ca_{2-x}Si$) [83,84]. Use of a ternary silicide with a carefully selected composition could allow for enhanced control of pore properties in the resulting porous silicon after selective leaching of the non-silicon components.

While selective extraction of Mg from Mg_2Si has been shown to yield highly porous structures for a variety of geometries across a large size range, there are some limitations to the porosification process developed here, especially with regard to substrate material (silicon nanowires used in this study were grown onto a stainless steel substrate, while silicon spheres were freestanding particles). The choice of substrate materials, if one is necessary, is limited to those which: (a) don't react with magnesium at temperatures utilized to form Mg_2Si; (b) don't react with oxygen at temperatures utilized to selectively oxidize Mg_2Si; and (c) don't react with acidic solutions utilized to dissolve the MgO from the MgO/Si composite. Stainless steel is an ideal substrate for the process. Both silicon and silica glass, common substrates used for silicon nanostructure growth, present problems since they will react with magnesium during conversion of the Si

structure into Mg_2Si. If either of these substrates are utilized, it is necessary to either limit reaction times so as to avoid unwanted reaction with the substrate, or to somehow shield the substrate during the silicidation step.

1.14 Conclusion

A process for introducing porosity into dense silicon structures has been designed consisting of two basic steps: (1) conversion of the as-grown silicon structure into a metal silicide with a larger volume, followed by (2) selective extraction of the metal from the metal silicide to generate porosity. Alkaline earth metal silicides were identified as appropriate sacrificial silicides due to the high reactivity of alkaline earth metals relative to silicon and the large atomic radius of alkaline earth metals. A variety of single phase Mg2Si nano- and microstructures were fabricated via gas/solid silicidation of silicon templates. Various methods for the shape-preserving, selective leaching of magnesium atoms from Mg_2Si were developed and evaluated. Selective oxidation of Mg_2Si to form an MgO/Si composite, followed by dissolution of MgO in acidic solution, led to generation of silicon structures with substantial porosity. The complete conversion of dense silicon nanowires into porous silicon replicas was demonstrated for the first time. The versatility of the porosification process was evaluated via synthesis of silicon spheres of varying sizes, from 150 nm to 1.5 μm diameters. In all cases, porous-silicon structures could be fabricated with shapes inherited from the initial, dense silicon template. Control over pore size was not achieved, but future techniques to potentially allow for control of pore characteristics were discussed.

1.15 References

[1] Dancil, Keiki-Pua S., Douglas P. Greiner, and Michael J. Sailor. "A porous silicon optical biosensor: detection of reversible binding of IgG to a protein A-modified surface." *Journal of the American Chemical Society* 121.34 (1999): 7925-7930.

[2] DeLouise, Lisa A., and Ben L. Miller. "Trends in porous silicon biomedical devices: tuning microstructure and performance trade-offs in optical biosensors." *Proceedings of SPIE*. Vol. 5357. 2004.

[3] Park, Ji-Ho, et al. "Biodegradable luminescent porous silicon nanoparticles for in vivo applications." *Nature materials* 8.4 (2009): 331-336.

[4] Ge, Mingyuan, et al. "Porous doped silicon nanowires for lithium ion battery anode with long cycle life." *Nano letters* 12.5 (2012): 2318-2323.

[5] Xia, Zhixuan, et al. "Highly Sensitive SOI Optical Sensors with Porous Si." *Integrated Photonics Research, Silicon and Nanophotonics*. Optical Society of America, 2012.

[6] Thakur, Madhuri, et al. "Inexpensive method for producing macroporous silicon particulates (MPSPs) with pyrolyzed polyacrylonitrile for lithium ion batteries." *Nature Scientific Reports* 2 (2012).

[7] Park, Ji-Ho, et al. "Biodegradable luminescent porous silicon nanoparticles for in vivo applications." *Nature materials* 8.4 (2009): 331-336.

[8] Uhlir, A. "Electrolytic Shaping of Germanium and Silicon." *The Bell System Technical Journal*, 35 (1956):

[9] Turner, Dennis R. "Electropolishing silicon in hydrofluoric acid solutions." Journal of the electrochemical Society 105.7 (1958): 402-408.

[10] Theunissen, M. J. J. "Etch Channel Formation during Anodic Dissolution of N-Type Silicon in Aqueous Hydrofluoric Acid." *Journal of the Electrochemical Society* 119.3 (1972): 351-360.

[11] Lehmann, V., and Ulrich Gösele. "Porous silicon formation: A quantum wire effect." *Applied Physics Letters* 58 (1991): 856.

[12] Canham, L_T. "Silicon quantum wire array fabrication by electrochemical and chemical dissolution of wafers." *Applied Physics Letters* 57 (1990): 1046.

[13] Smith, R. L., and S. D. Collins. "Porous silicon formation mechanisms." *Journal of Applied Physics* 71.8 (1992): R1-R22.

[14] Sailor, Michael J. *Porous silicon in practice: preparation, characterization and applications*. John Wiley & Sons, 2012.

[15] Thakur, Madhuri, et al. "Inexpensive method for producing macroporous silicon particulates (MPSPs) with pyrolyzed polyacrylonitrile for lithium ion batteries." *Scientific reports* 2 (2012).

[16] Hofmann, S., et al. "Gold catalyzed growth of silicon nanowires by plasma enhanced chemical vapor deposition." *Journal of Applied Physics* 94.9 (2003): 6005-6012.

[17] Gerberich, W. W., et al. "Superhard silicon nanospheres." *Journal of the Mechanics and Physics of Solids* 51.6 (2003): 979-992.

[18] Pool, Rebecca. "All optical communication comes of age." *SPIE Newsroom* (2010).

[19] Qu, Yongquan, et al. "Electrically conductive and optically active porous silicon nanowires." *Nano letters* 9.12 (2009): 4539-4543.

[20] Hochbaum, Allon I., et al. "Single crystalline mesoporous silicon nanowires." *Nano letters* 9.10 (2009): 3550-3554.

[21] Li, Xiuling. "Micro/Nano Lithography MacEtch: anisotropic metal-assisted chemical etching defies the textbooks."

[22] Zhong, Xing, et al. "Unveiling the formation pathway of single crystalline porous silicon nanowires." *ACS applied materials & interfaces* 3.2 (2011): 261-270.

[23] Raney, M. Method of producing finely divided nickel. U.S. Patent 1628190 (1927).

[24] Fouilloux, Pierre. "The nature of raney nickel, its adsorbed hydrogen and its catalytic activity for hydrogenation reactions (review)." *Applied catalysis* 8.1 (1983): 1-42.

[25] Adkins, Homer, and Harry R. Billica. "The preparation of Raney nickel catalysts and their use under conditions comparable with those for platinum and palladium catalysts." *Journal of the American Chemical Society* 70.2 (1948): 695-698.

[26] Pavlic, A. A., and Homer Adkins. "Preparation of a Raney nickel catalyst." *Journal of the American Chemical Society* 68.8 (1946): 1471-1471.

[27] Erlebacher, Jonah, et al. "Evolution of nanoporosity in dealloying." *Nature* 410.6827 (2001): 450-453.

[28] Ding, Yi, Y-J. Kim, and Jonah Erlebacher. "Nanoporous gold leaf:"Ancient technology"/advanced material." *Advanced materials* 16.21 (2004): 1897-1900.

[29] Yamashita, Hiromi, et al. "Catalysis by amorphous metal alloys. Part 3.—Catalytic activity of raney copper catalysts prepared from amorphous $Cu_{62}Zr_{38}$ powder." *J. Chem. Soc., Faraday Trans. 1* 82.3 (1986): 707-714.

[30] Pugh, D. V., A. Dursun, and S. G. Corcoran. "Formation of nanoporous platinum by selective dissolution of Cu from $Cu_{0.75}Pt_{0.25}$." *Journal of materials research* 18.1 (2003): 216-221.

[31] Okada, Kiyoshi, et al. "Water vapor sorption on mesoporous gamma-alumina prepared by the selective leaching method." *Journal of Porous Materials* 4.4 (1997): 253-260.

[32] Temuujin, Jadambaa, Kiyoshi Okada, and Kenneth JD MacKenzie. "Preparation of porous silica from vermiculite by selective leaching." *Applied Clay Science* 22.4 (2003): 187-195.

[33] Okada, Kiyoshi, et al. "Preparation of microporous silica from metakaolinite by selective leaching method." *Microporous and mesoporous materials* 21.4 (1998): 289-296.

[34] Shinoda, Tomotaka, Makoto Onaka, and Yusuke Izumi. "Proposed models of mesopore structures in sulfuric acid-treated montmorillonites and K10." *Chemistry Letters* 7 (1995): 495-496.

[35] Zhang, Zhonghua, et al. "Ultrafine nanoporous $PdFe/Fe_3O_4$ catalysts with doubly enhanced activities towards electro-oxidation of methanol and ethanol in alkaline media." *Journal of Materials Chemistry A* (2013).

[36] Temuujin, Jadambaa, Kiyoshi Okada, and Kenneth JD MacKenzie. "Preparation of porous silica from vermiculite by selective leaching." *Applied Clay Science* 22.4 (2003): 187-195.

[37] Yushin, Gleb, Y. Gogotsi, and A. Nikitin. "Carbide derived carbon." *CRC Press: Boca Raton, FL* (2006): 237-280.

[38] Presser, Volker, Min Heon, and Yury Gogotsi. "Carbide-Derived Carbons–From Porous Networks to Nanotubes and Graphene." *Advanced Functional Materials* 21.5 (2011): 810-833.

[39] *O. Hutchins, US Patent 1271713, 1918.*

[40] Boehm, H. P., and H. H. Warnecke. "Structural parameters and molecular sieve properties of carbons prepared from metal carbides." *Carbon* 13.6 (1975): 548.

[41] Gogotsi, Yury G., In-Deok Jeon, and Michael J. McNallan. "Carbon coatings on silicon carbide by reaction withchlorine-containing gases." *J. Mater. Chem.* 7.9 (1997): 1841-1848.

[42] Gogotsi, Yury, et al. "Nanoporous carbide-derived carbon with tunable pore size." *Nature materials* 2.9 (2003): 591-594.

[43] Gogotsi, Yury, et al. "Tailoring of nanoscale porosity in carbide-derived carbons for hydrogen storage." *Journal of the American Chemical Society* 127.46 (2005): 16006-16007.

[44] Dash, Ranjan, et al. "Titanium carbide derived nanoporous carbon for energy-related applications." *Carbon* 44.12 (2006): 2489-2497.

[45] Chmiola, John, et al. "Monolithic carbide-derived carbon films for micro-supercapacitors." *Science* 328.5977 (2010): 480-483.

[46] Korenblit, Yair, et al. "High-rate electrochemical capacitors based on ordered mesoporous silicon carbide-derived carbon." *Acs Nano* 4.3 (2010): 1337-1344.

[47] Nyce, Gregory W., et al. "Synthesis and characterization of hierarchical porous gold materials." *Chemistry of materials* 19.3 (2007): 344-346.

[48] Ersoy, Daniel A., Michael J. McNallan, and Yury Gogotsi. "Carbon coatings produced by high temperature chlorination of silicon carbide ceramics." *Material Research Innovations* 5.2 (2001): 55-62.

[49] The electrochemical delithiation of lithiated silicon has been intensely studied, as it represents a major limitation for the use of silicon anodes in Li-ion batteries. In principle, this reaction can be thought of as a selective leaching process since it involves selective extraction of Li atoms from Li-Si compounds and results in the production of porous silicon as the only remaining solid phase. The claim that "no selective leaching process for formation of porous silicon has been described" is therefore not strictly true. It is plausible that porous silicon could be produced through incorporation of dense silicon into the anode of a Li-ion battery, followed by a complete cycle of lithiation-delithiation, followed by removal of the (now porous) silicon anode and dissolution of any residual binder or electrolyte material. However, such method as a means of producing porous silicon would be severely limited, impractical, and inefficient.

[50] Kirkendall, E. O., and A. D. Smigelskas. "Zinc diffusion in alpha brass." *Aime Trans* 171 (1947): 130-142.

[51] Fan, Hong Jin, Ulrich Gösele, and Margit Zacharias. "Formation of nanotubes and hollow nanoparticles based on Kirkendall and diffusion processes: a review." *Small* 3.10 (2007): 1660-1671.

[52] Chen, L. J. "Metal silicides: An integral part of microelectronics." JOM 57.9 (2005): 24-30.

[53] d'Heurle, F. M., and C. S. Petersson. "Formation of thin films of $CoSi_2$: Nucleation and diffusion mechanisms." *Thin Solid Films* 128.3 (1985): 283-297.

[54] *Powder Diffraction File* Card No. 27–1402 for Si, Card No. 45–946 for MgO, Card No. 35–0773 for Mg_2Si (International Center on Diffraction Data, Newtown Square, Pennsylvania); ⟨www.icdd.com⟩.

[55] Paul, Aloke, et al. "The Kirkendall effect in multiphase diffusion." *Acta Materialia* 52.3 (2004): 623-630.

Van Dal, M. J. H., et al. "Formation of Co–Si intermetallics in bulk diffusion couples. Part I. Growth kinetics and mobilities of species in the silicide phases." *Intermetallics* 9.5 (2001): 409-421.

[56] *Powder Diffraction File* Card No. 01-076-1748 for FeSi, Card No. 26-1141 for Fe_2Si (International Center on Diffraction Data, Newtown Square, Pennsylvania);

[57] Cordero, Beatriz, et al. "Covalent radii revisited." *Dalton Transactions* 21 (2008): 2832-2838.

[58] Detavernier, Christophe, et al. "Mixing entropy and the nucleation of silicides: Ni-Pd-Si and Co-Mn-Si ternary systems." *Journal of materials research* 18.7 (2003): 1668-1678.

[59] Schmitt, Andrew L., et al. "Synthesis and applications of metal silicide nanowires." *Journal of Materials Chemistry* 20.2 (2010): 223-235.

[60] Lefenfeld, Michael, James L. Dye, and Scott Calabrese Barton. "Sodium Silicide and Alkali Metal-Silica Gel for Convenient Hydrogen Production."

[61] Ropp, Richard C. *Encyclopedia of the Alkaline Earth Compounds*. Access Online via Elsevier, 2012.

[62] Ohring, Milton. *Materials science of thin films*. Academic press, 2001; and Chu, W. K., et al. "Implanted noble gas atoms as diffusion markers in silicide formation." *Thin Solid Films* 25.2 (1975): 393-402.

[63] Ogilvie, J. F. "Aspects of the Chemical Bond 1996." *Conceptual Perspectives in Quantum Chemistry*. Springer Netherlands, 1997. 127-143.

[64] Palenzona, A., and M. Pani. "The phase diagram of the Sr–Si system." *Journal of alloys and compounds* 373.1 (2004): 214-219.

[65] Hatton, Benjamin, et al. "Assembly of large-area, highly ordered, crack-free inverse opal films." *Proceedings of the National Academy of Sciences* 107.23 (2010): 10354-10359.

[66] Stöber, Werner, Arthur Fink, and Ernst Bohn. "Controlled growth of monodisperse silica spheres in the micron size range." *Journal of colloid and interface science* 26.1 (1968): 62-69.

[67] Okamoto, H. "Mg-Si (Magnesium-Silicon)." *Journal of Phase Equilibria and Diffusion* 28.2 (2007): 229-230.

[68] Manfrinetti, P., M. L. Fornasini, and A. Palenzona. "The phase diagram of the Ca–Si system." *Intermetallics* 8.3 (2000): 223-228.

[69] Itkin, V. P., and C. B. Alcock. "The Si-Sr (Silicon-Strontium) system." *Journal of Phase Equilibria* 10.6 (1989): 630-634.

[70] Yinye, Yang, and Xie Quan. "Growth Characteristics of Calcium Silicides Films from the Deposited Ca Films at the Different Sputtering Ar Pressure." *Computer Science and Computational Technology, 2008. ISCSCT'08. International Symposium on*. Vol. 1. IEEE, 2008.

[71] Lu, Kuo-Chang. *Nano-silicide Formation Through Point Contact Reaction, Nickel-silicon/silicon/nickel-silicon and Platinum-silicon/silicon/platinum-silicon Nanowire Heterostructures for Nanodevices*. ProQuest, 2008.

[72] Walker, Perrin, and William H. Tarn, eds. *CRC handbook of metal etchants*. CRC press, 1990.

[73] Nandi, K. C., et al. "A novel and inexpensive method of production of silanes from rice husk and their gas chromatographic analyses." *Solar energy materials* 22.2 (1991): 161-167.

U.S. Patent No. 2,915,368. 1 Dec. 1959.; Aas, Helge Hakonsonn. "Process for refining technical grade silicon and ferrosilicon by continuous extraction."

Popova, O. I. "Regularities in the variation of the chemical properties of silicide powders." *Powder Metallurgy and Metal Ceramics* 21.3 (1982): 209-213.

[74] Baranek, Philippe, Joël Schamps, and Isabelle Noiret. "Ab initio studies of electronic structure, phonon modes, and elastic properties of Mg2Si." *The Journal of Physical Chemistry B* 101.45 (1997): 9147-9152.

[75] Fitzmaurice, Jonathan C., et al. "Synthesis of Metal Silicide Powders by Thermolysis of Metal Chlorides with Magnesium Silicide." *Phosphorus, Sulfur, and Silicon and the Related Elements* 101.1-4 (1995): 47-55.

[76] Murray, J. L., and A. J. McAlister. "The Al-Si (aluminum-silicon) system." *Bulletin of Alloy Phase Diagrams* 5.1 (1984): 74-84.

[77] Tani, Jun-ichi, Masanari Takahashi, and Hiroyasu Kido. "Fabrication of oxidation-resistant β-$FeSi_2$ film on Mg_2Si by RF magnetron-sputtering deposition." *Journal of Alloys and Compounds* 488.1 (2009): 346-349.

[78] Outokumpu, H. S. C. "Chemistry for Windows." *Chemical Reaction and Equilibrium Software with Extensive Thermochemical Database. Version* 4 (1993).

[79] Rhines, Frederick N. "A metallographic study of internal oxidation in the alpha solid solutions of copper." *AIME TRANS* 137 (1940): 246-286.

[80] Csepregi, L., et al. "Reordering of amorphous layers of Si implanted with P, As, and B ions." *Journal of Applied Physics* 48 (1977): 4234.

[81] Olson, G. L., and J. A. Roth. "Kinetics of solid phase crystallization in amorphous silicon." *Materials Science Reports* 3.1 (1988): 1-77.

[82]Hu, Junhua, et al. "Optical and electronic properties of M_2Si (M= Mg, Ca, Sr) grown by reactive deposition technique." *International Journal of Modern Physics B* 24.19 (2010): 3693-3699.

[83] Wu, Hui, et al. "Structure and hydrogenation properties of the ternary alloys $Ca_{2-x}Mg_xSi$ ($0 \leq x \leq 1$)." *Journal of Alloys and Compounds* 446 (2007): 101-105.

[84] Gröbner, Joachim, Igor Chumak, and Rainer Schmid-Fetzer. "Experimental study of ternary Ca–Mg–Si phase equilibria and thermodynamic assessment of Ca–Si and Ca–Mg–Si systems." *Intermetallics* 11.10 (2003): 1065-1074.

Part II: Shape-Preserving Chemical Transformations of SiO_2 Photonic Structures

Overview

Part I of this thesis described the conversion of dense silicon structures into porous replicas. Such a porosification process can be considered a *shape-preserving* ***physical*** *transformation,* since the goal of the process is to maintain both the initial overall shape (spheres, nanowires, etc.) and the chemical composition (silicon) of the starting material while introducing some modification into the physical structure (i.e., the introduction of pores). In this chapter, a variety of *shape-preserving* ***chemical*** *transformations* are described, in which the goal is to completely maintain the shape and morphology of the initial material while changing its chemical composition.

Several shape preserving chemical transformations of silica or silicate materials have been previously reported for a wide range of shapes with feature sizes ranging from the macro- to the nanoscale. In general, such transformations involve either (a) reduction of the SiO_2 under exposure to a metallic element with a higher oxidation potential than silicon, or (b) a metathetic displacement reaction between SiO_2 and a metal halide. An early example of the first type of reaction is the reaction between mullite ($Al_6Si_2O_{13}$)[85] or other silicates[86] and liquid aluminum, in which Si^{+4} is reduced to Si^0 while Al is oxidized to Al^{+3} via reaction 3.1.

$$3Al_6Si_2O_{13}(s) + 8Al(l) \rightarrow 13Al_2O_3(s) + 6Si(l) \qquad (3.1)$$

When liquid metal is used for the reduction of silica, as in equation 3.1, the process is known as reactive metal penetration (RMP) or reactive infiltration. These types

of liquid/silica reactions require dunking the silicate preform into a molten liquid metal, allowing time for infiltration and reaction, removing the reacted product from the liquid, and polishing to remove condensed, excess metal from the part's surface. Such liquid/solid shape-preserving reactions are applied to macroscale performs (i.e., those with features of several mm to cm in size).

For micro- or nanoscale structures, **gas**-based reactions (as opposed to liquid infiltration) are preferred due to the capability of a reactant gas to easily penetrate narrow openings and react uniformly with a nanostructured solid. For example, in a gas/silica reaction, the initial SiO_2 material is exposed to an atmosphere containing a reactive vapor at elevated temperatures. Following the initial gas-based reaction, secondary reactions (such as selective removal of product phases or further metathesis reactions) can be utilized to ultimately yield the desired product. One of the most well studied shape-preserving gas/silica reactions is the magnesiothermic reduction of a SiO_2 preform into a MgO/Si composite replica (reaction 3.2)[87].

$$SiO_2(s) + 2Mg(g) \rightarrow 2MgO(s) + Si(s) \qquad (3.2)$$

Selective removal of MgO via acid leaching yields a single phase Si replica[87] of the initial SiO_2 material. The shape of the frustules is maintained throughout the reaction, and, under appropriate reaction conditions, even very fine nanoscale features are well-preserved (Figure 35).

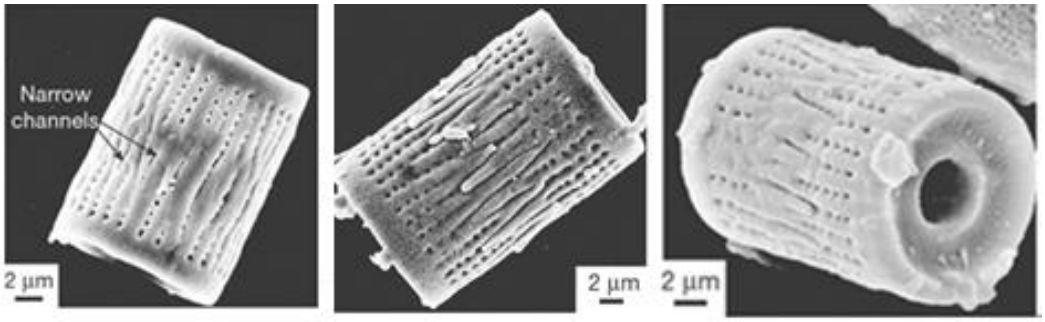

Figure 35: Conversion of a diatom frustule from SiO_2 (left) into an MgO/Si composite (middle) and a single phase Si replica (right). Preservation of very fine, nanoscale features can be observed.[87]

In addition to reduction reactions involving SiO_2, other shape preserving reactions have been reported which utilize a metathetic displacement reaction between SiO_2 and gaseous metal halide. Table 5 provides an overview of reported materials which have been fabricated via shape-preserving gas/solid reactions of SiO_2 structures.

Table 5: Overview of Previously Reported Shape Preserving Gas / SiO_2 Reactions

MgO	Magnesiothermic reduction, dissolution of Si	88
Si	Magnesiothermic reduction, dissolution of MgO	89
Mg_2Si/MgO Composite	Magnesiothermic reduction, excess Mg	90
TiO_2 or $TiOF_2$	Reaction with TiF_4 gas	91
ZrO_2	Reaction with $ZrCl_4$ gas	92

In the following two chapters, a series of sequential shape preserving reactions will be explored on SiO_2 based photonic materials, with the goal of maintaining the photonic structure while changing the chemical composition of the material. The magnesiothermic reduction of silica, shown in reaction 3.2, will serve as the initial reaction step for all the processes developed in the following chapters.

Chapter 2: Conversion of SiO_2 Photonic Crystals into High-Index Mg_2Si Replicas

2.1 Summary

In the past decade, highly ordered, periodic structures known as photonic crystals have attracted significant attention due to their extraordinary ability to manipulate light. For materials possessing a complete three dimensional photonic bandgap, propagation of light of a given energy range is forbidden at all incident angles. Fabrication of periodic photonic structures in three dimensions is particularly challenging. Recently, a lithography-free method has been developed based on the sol-gel deposition of SiO_2 around a matrix of self-assembled polystyrene spheres. This process allows for the relatively cheap fabrication of wide-area, low-defect density, three dimensional photonic structures of SiO_2. Unfortunately, the refractive index of SiO_2 is well below the threshold necessary for a material to possess a complete photonic bandgap in the visible and near-IR range. In this chapter, the shape-preserving transformation of both synthetic and biologically-derived SiO_2 photonic structures into Mg_2Si replicas possessing a significantly higher refractive index is explored.

2.2 Background of Photonic Crystals and Photonic Bandgaps

The concept of utilizing highly ordered, periodic materials as a means to manipulate light propagation was first proposed in the late 1980s[93]. Inspired by semiconductors, in which the periodic variation in electrical potential created by the crystal lattice results in the formation of electronic bandgaps, it was suggested that structures containing a periodic variation in the dielectric constant, with a periodicity on the order of the optical wavelength, could be used to form materials with photonic

bandgaps. Such *photonic crystals*, with complete bandgaps in the near-IR or visible region, are expected to have significant applications in the development of all-optical integrated circuits[94].

In order to possess a complete three dimensional bandgap, in which propagation of a certain frequency of light is prohibited in all directions, several criteria must be satisfied: (a) the material must possess an extremely well-ordered periodicity similar to the wavelength of light with limited defects[95]; (b) the material must possess a relatively large refractive index ($n>2.85$ for an inverse opal structure)[96]; and (c) the material must be transparent at the wavelength of interest, in order to minimize losses due to absorption. Note that the first criteria is structural, while the second two depend on the intrinsic chemical composition of the material.

Since their conception 27 years ago, significant advances have been made in both the theoretical understanding and the practical fabrication of photonic crystals. Nevertheless, there exist only a few methods capable of producing large-area, low defect density photonic crystals possessing a complete band-gap. Silicon ($n >3.4$ for near-IR wavelengths) based 3D photonic crystals have been fabricated via a variety of layer-by-layer lithographic methods[97]. However, due to the complexity of 3D photonic structures, lithographic methods are time-consuming and expensive. A more cost effective technique for the fabrication of silicon photonic crystals is based on colloidal self-assembly of silica spheres to form an opal template, followed by chemical vapor deposition of Si in the voids between the spheres and finally dissolution of the silica. Although such an approach avoids costly lithography, it still requires a specially-modified CVD instrument

and yields photonic crystals with relatively small domain sizes on the order of approximately 100 um[98].

While large-scale and cost-effective fabrication of wide area **silicon** photonic crystals with controllable defects is difficult, fabrication of **silica** photonic structures is much more straightforward. A number of methods based on self-assembly of silica spheres (to form direct opals) or latex spheres (followed by infiltration with a liquid sol-gel SiO_2 precursor to form inverse opals) have been utilized. Colloidal self-assembly of spheres via spin-coating[99], evaporative deposition[100], or sedimentation[101] has been used to fabricate wafer-scale SiO_2 based photonic crystals, although uncontrolled cracks, domain boundaries, and other defects were typically observed[102]. Recently, our collaborators at Harvard University have developed a co-assembly method in which a colloidal template of latex spheres is deposited in a tetraethoxy silane (TEOS) precursor matrix[103]. Firing the samples at 500^{o}C in air for several hours results in pyrolysis of the latex spheres conversion of the deposited TEOS matrix into an inverse opal of SiO_2 (Figure 36).

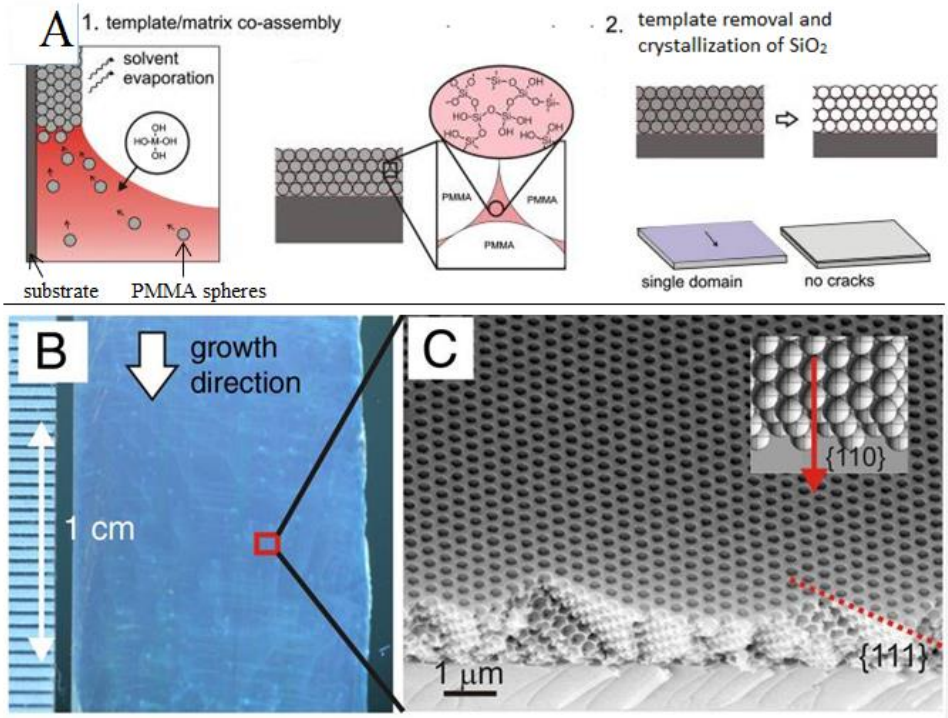

Figure 36[103]: (a) Schematic for synthesis of crack free, wide-area SiO_2 photonic crystals via coassembly of latex spheres in a TEOS matrix; (B) optical image of the photonic crystal; (c) SEM image of corresponding crystal.

Crack-free, large area inverse opal films have been fabricated using the coassembly method illustrated in Figure 36. Furthermore, both line and point defects can be controllably introduced through use of a topologically patterned substrate (Figure 37)[104]. The controlled introduction of such defects is essential to the development of all-optical integrated circuits, as they allow for effective waveguiding (analogous, for example, to copper traces on a silicon circuit in an electrical circuit) and photon trapping[105].

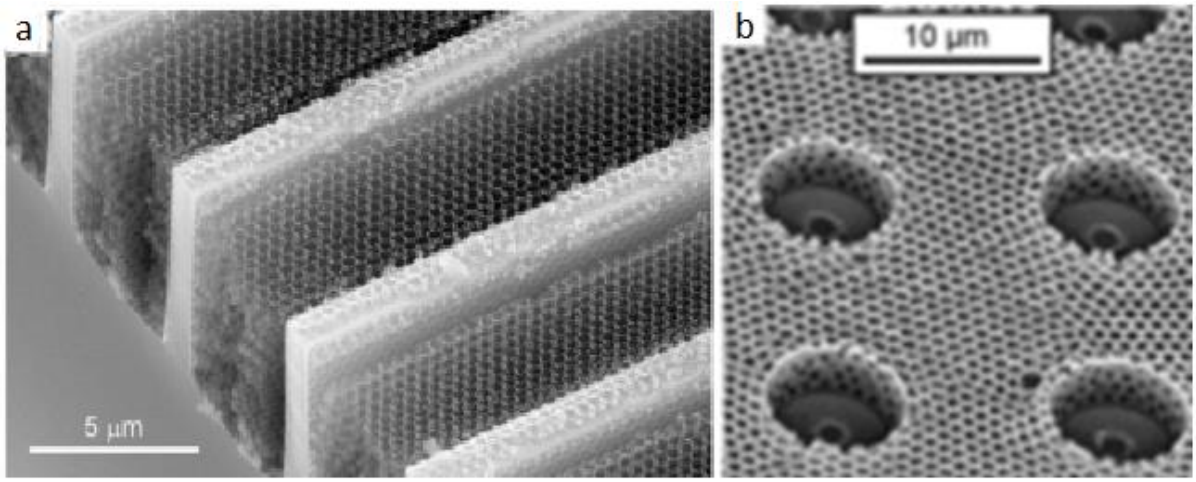

Figure 37[104]: Controlled introduction of defects into SiO_2 photonic crystals via a modified coassembly method.

In order for a material to possess a complete 3D photonic bandgap, both the structural and chemical requirements discussed previously must be satisfied. SiO_2 based materials satisfying the **structural** requirements have been fabricated using low-cost, large-scale, and versatile methods. Unfortunately, these materials fail to satisfy the **chemical** criteria for a material possessing a complete photonic bandgap since the refractive index of SiO_2 (n~1.5) at visible and near-IR wavelengths is well below the threshold necessary to achieve a complete photonic bandgap. As a result, SiO_2 photonic crystals possess only partial or pseudo-bandgaps, in which forbidden bands exist only in certain propagation directions (as opposed to a complete 3D bandgap for all propagation directions).

2.3 Motivation and Approach

The shape-preserving chemical transformation of a SiO_2 photonic crystal into a replica with a different chemical composition could potentially be used to overcome the inherent chemical limitations of SiO_2 (namely, its low refractive index) while exploiting

the advantageous techniques which exist for fabrication of complex, three dimensional periodic SiO_2 structures. The transformation of 3D silica structures into silicon replicas (see Figure 35) was first reported in 2007. Silicon is an obvious choice for photonic crystals, since it is transparent in the near infrared region of the spectrum and possesses a near-IR index of refraction (n~3.4) sufficient for complete photonic bandgaps[114]. As a result, a number of groups have proposed the use of a magnesiothermic reduction to convert SiO_2 photonic crystals with a partial bandgap into silicon replicas with a complete bandgap[106] via reactions 3.3 and 3.4.

$$\mathbf{SiO_2(s)} + 2Mg(g) \rightarrow 2MgO/Si(s) \qquad (3.3)$$

$$2MgO/Si(s) + 4HCl(a) \rightarrow 2MgCl_2(a) + 2H_2(g) + \mathbf{Si(s)} \qquad (3.4)$$

While initially such a route may seem like a promising method to fabricate high index photonic crystals, deeper investigation reveals a significant problem with this approach. Initial exposure of SiO_2 preforms to Mg vapor results in the formation of an intermixed 2MgO/Si composite material. Due to the molar volumes of amorphous SiO_2 (~27 cc/mol)[107], MgO (11.3 cc/mol)[108], and Si (12.1 cc/mol)[108], this initial conversion of SiO_2 into a 2MgO/Si composite will result in a slight volume expansion of ~26%. The resulting composite will be comprised of ~65% by volume MgO and ~35% by volume Si. Dissolution of the MgO to form single phase silicon results in highly porous silicon (~65 vol% porosity)[109]. This porosity is unavoidable and results in a significant decrease in the refractive index relative to dense Si to well below the threshold of ~2.85 necessary for a complete photonic bandgap (Figure 38).

Table 6: Molar Volumes of Relevant Materials[107,108]

Material	**Volume (cc per mole of Si)**
SiO_2	27.4
2MgO/Si Composite	34.6
Si	12.1
Mg_2Si/2MgO Composite	62.0
Mg_2Si	39.5

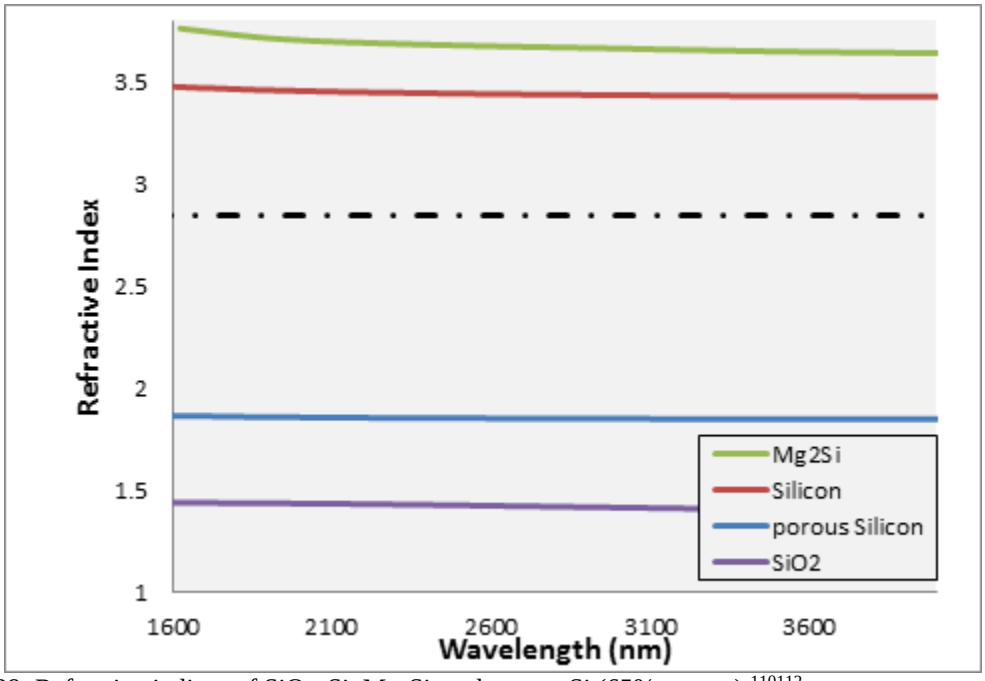

Figure 38: Refractive indices of SiO_2, Si, Mg_2Si, and porous Si (65% porous).[110112]

Like silicon, magnesium silicide (Mg_2Si) also satisfies the chemical requirements for a photonic crystal with a complete bandgap in the IR: Mg_2Si is transparent in the near infrared with an absorption edge at approximately 1770 nm (Figure 39)[111] and it has a high refractive index (n>3.6), even higher than that of dense silicon, within this frequency range (Figure 38)[112].

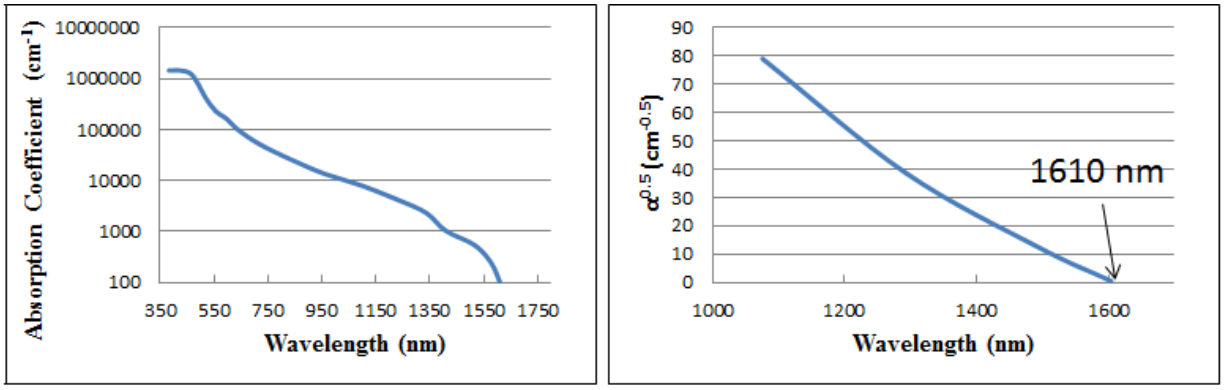

Figure 39: Wavelength-dependent absorption of bulk Mg_2Si, showing transparency above approximately 1.6 μm.[111]

Furthermore, since the volume of Mg_2Si is larger than that of either SiO_2 or 2MgO/Si, a shape preserving transformation of dense SiO_2 into Mg_2Si is expected to result in a fully dense product (Table 6). As previously discussed, conversion of SiO_2 into silicon via a 2MgO/Si composite intermediate results in silicon which is approximately 65% porous by volume. A secondary reaction with magnesium to convert the porous silicon into Mg_2Si is expected to result in volume expansion of the structure and in filling of the residual porosity. Theoretically, conversion of 83% of the porous silicon intermediate into Mg_2Si is necessary to fully fill the residual porosity and yield a dense product, while complete conversion is expected to lead to a slight swelling of the structure. A shape preserving transformation of SiO_2 photonic structures into Mg_2Si replicas could therefore be utilized to potentially fabricate wide area 3D photonic crystals with complete bandgaps in the near IR.

Previously, the conversion of complex SiO_2 shapes into Mg_2Si/MgO composite replicas was demonstrated via reaction 3.5[113].

$$SiO_2(s) + 4Mg(g) \rightarrow 2MgO(s) + Mg_2Si(s) \qquad (3.5)$$

This reaction is similar to the magnesiothermic reduction of SiO_2 to form a MgO/Si composite replica, but occurs when an excess amount of magnesium is used relative to the stoichiometry of reaction 3.2. While the product contains Mg_2Si as desired, it is not single phase Mg_2Si but rather an intermixed composite of MgO and Mg_2Si. Due to the low refractive index of MgO (n=1.7 at 2 μm[114]), its presence will significantly reduce the overall refractive index of the composite material and there is no reported etchant for the selective dissolution of the MgO phase while retaining the Mg_2Si phase. Furthermore, the volume difference between the starting SiO_2 and the resulting Mg_2Si/2MgO composite is large (an increase of approximately 126%)[108]. This volume difference results in substantial swelling of the structure after complete reaction. Figure 40 shows the product of the reaction carried out on a diatom frustule-- while the overall shape of is maintained, significant swelling and degradation of fine features and surface morphology was observed.

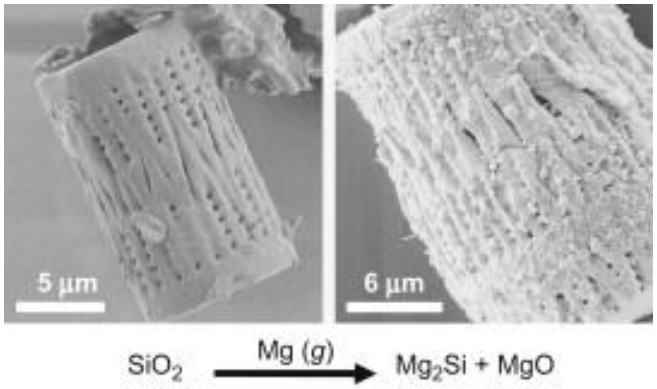

Figure 40: Degradation of fine features observed during conversion of SiO_2 into an Mg_2Si/MgO composite[113].

Even if the MgO could be selectively dissolved from the Mg_2Si/MgO composite, the structure of the resulting porous Mg_2Si would be substantially altered from that of the starting SiO_2 . Furthermore, the Mg_2Si would contain significant residual porosity (~37%

by volume) following dissolution of the MgO, resulting in a decreased effective refractive index to ~2.6 using a simple parallel effective medium approximation[115]. The direct reactive conversion of SiO_2 into Mg_2Si/MgO is therefore undesirable as a method of transforming SiO_2 into dense Mg_2Si if maintaining structural features and dimensions is important (as is the case for photonic crystals).

An alternative route for the transformation of SiO_2 into dense Mg_2Si replicas is proposed here, based on two successive steps: (1) conversion of SiO_2 into porous Si, followed by (2) a secondary reaction of the porous silicon in magnesium vapor to form Mg_2Si (reactions 3.6 - 3.8).

$$SiO_2(s) + 2Mg(g) \rightarrow \mathbf{2MgO/Si(s)} \quad (3.6)$$

$$\mathbf{2MgO/Si(s)} + 4HCl(a) \rightarrow 2MgCl_2(a) + 2H_2(g) + \mathbf{porous\text{-}Si(s)} \quad (3.7)$$

$$\mathbf{porous\text{-}Si} + 2Mg(g) \rightarrow \mathbf{Mg_2Si(s)} \quad (3.8)$$

The volume expansion upon conversion of SiO_2 into the 2MgO/Si composite is only about 26% (as compared to 126% for conversion into 2MgO/Mg_2Si). As discussed previously, the conversion of SiO_2 into porous silicon via a 2MgO/Si composite intermediate has been demonstrated on a number of structures with excellent shape and fine feature preservation. Subsequent exposure of porous Si to magnesium vapor is expected to result in formation of the Mg_2Si, as discussed in the chapter 1 of this thesis. Since the molar volume of Mg_2Si (39.5 cc)[108] is slightly larger than the volume 2MgO/Si composite (34.6 cc)[108], the final Mg_2Si product is expected to be fully dense (that is, all the porosity generated by dissolution of MgO from the MgO/Si composite is expected to be filled in after reaction with Mg(g) to form Mg_2Si).

Simulations using the known refractive index of Mg_2Si were conducted by Dr. Dr. Nicolas Vogel (Harvard University) in order to optimize the inverse opal design for a complete bandgap at 2 μm, at which Mg_2Si is transparent. A 1D-layer model approximation was used to simulate reflectance behavior, and the calculated reflection bands for inverse opals of various hole radii are shown in Figure 41.

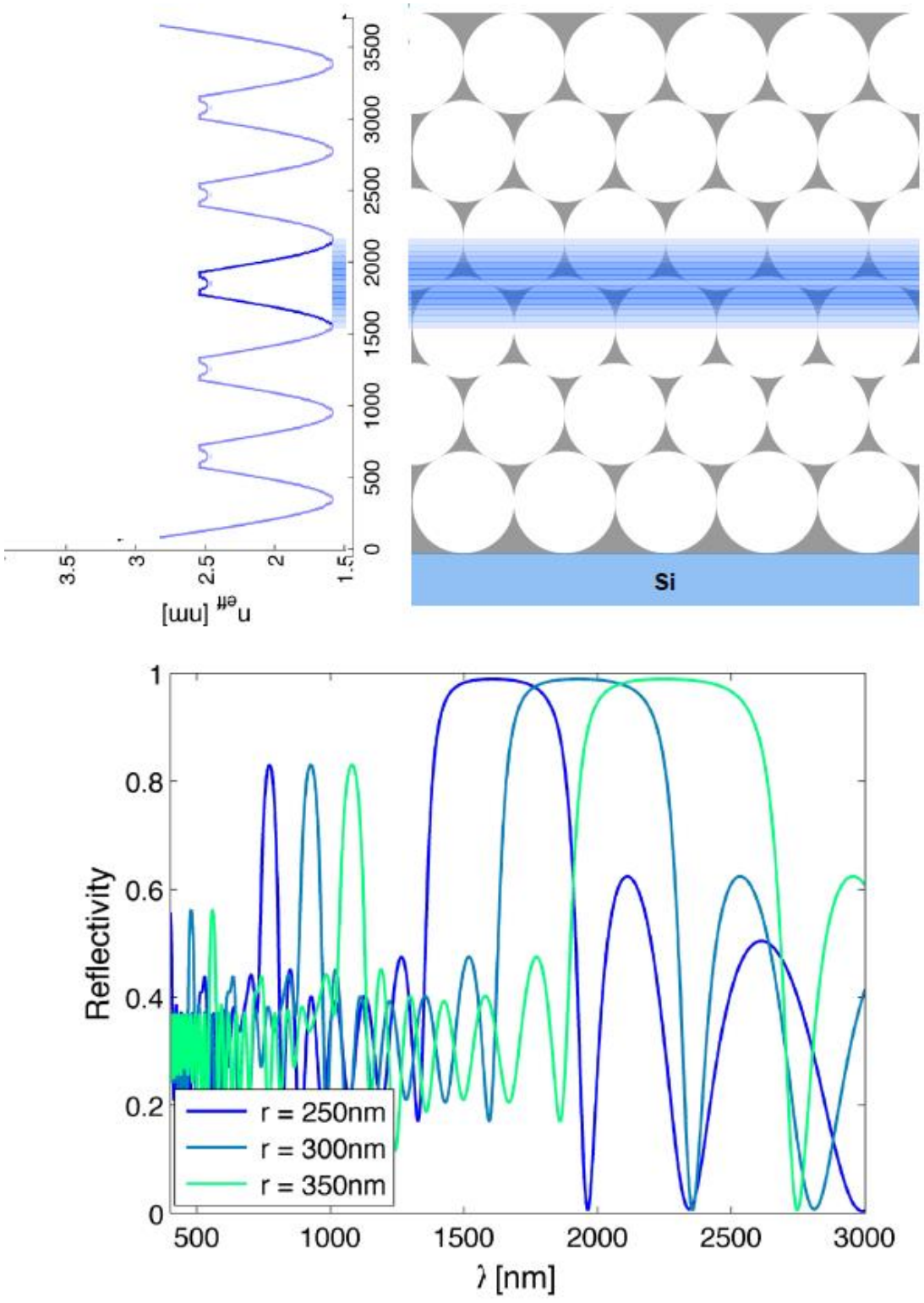

Figure 41: 1-D layer approximation model (top) and calculated reflectance bands (bottom) for Mg_2Si inverse opals of various hole radii (courtesy of Dr. Vogel, Harvard University).

These simulations suggest that air holes of 300 nm radius in an Mg_2Si matrix should lead to a relatively wide and complete photonic bandgap centered near a wavelength of 2 μm. Larger air holes lead to a wider bandgap at higher wavelengths, while smaller air holes shift the bandgap to lower wavelengths. The bandgap could potentially be tuned by using various inverse opal geometries (although there is a lower wavelength limit of approximately 1.6 μm, below which the optical absorption by Mg_2Si becomes significant, Figure 39).

2.4 Experimental Methods

SiO_2 inverse opals were synthesized following previously published methods[103] by Nicolas Vogel via coassembly of 610 nm diameter polystyrene spheres in a TEOS-containing solution. A firing step at 500^{o}C in air for two hours was used to pyrolize the spheres and generate dense wall SiO_2. The resulting inverse opal structures had domain sizes of several hundred square microns (Figure 42). With optimization of synthesis conditions, it is likely that better quality structures could be obtained (i.e., larger domain sizes with fewer defects). However, for the purposes of evaluating the shape-preserving transformation of SiO_2 into Mg_2Si, the synthesized inverse opals were of sufficient quality and no further optimization related to SiO_2 inverse opal growth was conducted. Small sections, approximately 1cm^2, of the inverse opal samples were used for each conversion. A flow-through reactor setup was utilized in which the SiO_2 inverse opals were placed in a stainless steel tube furnace at a position "downstream" from a bed of 500 mg of Mg_2Si

powder (Alfa-Aesar, 99.5%). Ultra high purity argon was passed through a titanium-getter and then through the furnace at a flow rate of 300mL/minute. Reaction temperatures between 750°C-850°C for periods of 6-24 hours were utilized. After completion of the initial magnesiothermic reduction, the inverse opals or were removed and washed with 1M HCl to remove MgO and yield por-Si replicas. Subsequent conversion to Mg_2Si was carried out in a similar flow-through reactor, except utilizing Mg powder (-325 mesh, Alfa-Aesar, 99%) in place of Mg_2Si powder and reaction temperatures of 550-650°C. For diatom conversions, cleaned diatom frustules were drop-coated from an ethanolic suspension onto silicon substrates, and magnesiothermic reduction of the frustules into por-Si replicas was carried out in a flow-through reactor exactly as described previously for the inverse opals. For conversion into Mg_2Si, The substrate containing the diatom frustules was placed face up in a graphite crucible approximately 1 cm deep. A small piece of polished magnesium foil (GalliumSource L.L.C, 99.95%, 1.0mm thick) was placed on top of the crucible approximately 1 cm above the sample, and the crucible was placed in the furnace with Ti-gettered Argon.

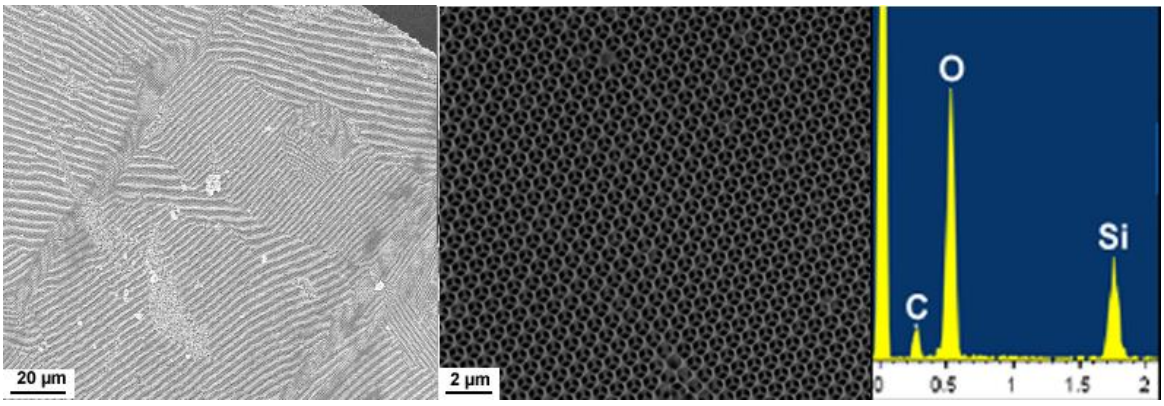

Figure 42: Wide area view (left) showing various domains and magnified view (middle) of a single domain. EDS (right) is consistent with SiO_2.

2.5 Results and Discussion

The shape-preserving magnesiothermic reduction of SiO_2 has been previously demonstrated in the literature for numerous structures, including inverse opals[103]. The procedure used here is similar to the magnesiothermic reduction method as originally reported, with a few modifications. The first step of the process involves exposure of the SiO_2 structure to magnesium vapor at elevated temperature (T>~600^{o}C). There are two possible reaction products which can form depending of the partial pressure of the magnesium vapor. In a certain magnesium partial pressure range (*i.e.*, between ~3E-015 to ~5E-6 atm at 800^{o}C) only a 2MgO/Si composite is observed (reaction 3.9), while at higher magnesium pressures a 2MgO/Mg_2Si composite is observed (reaction 3.10).

$$SiO_2 + 2Mg(g) \rightarrow Si + 2MgO \quad (3.9)$$

$$SiO_2 + 4Mg(g) \rightarrow Mg_2Si + 2MgO \quad (3.10)$$

As discussed previously, formation of the Mg_2Si/2MgO composite results in significant loss of shape and is undesirable. Therefore, the magnesium partial pressure during the reaction must be maintained at a high enough level to allow for reaction 3.9, but below the level necessary drive reaction 3.10. The equilibrium partial pressure of Mg vapor produced via vaporization of the pure metal is thermodynamically sufficient to form the undesirable Mg_2Si/2MgO product at all temperatures (Figure 43)[117].

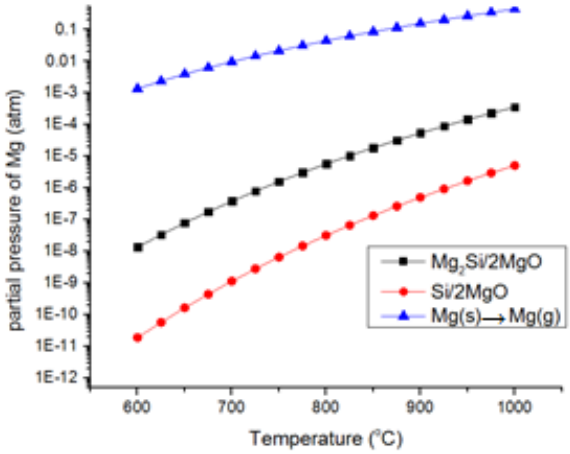

Figure 43: Equilibrium magnesium partial pressures produced via vaporization of Mg, and pressures necessary to drive magnesiothermic reduction reactions 3.9 and 3.10.[117]

Instead of using pure magnesium as the vapor source, the vaporization of an alloy can be utilized to obtain lower magnesium partial pressures. In this case, Mg_2Si powder is used as the magnesium source. Evaporation of magnesium from $Mg_2Si(s)$ results in a reduced magnesium partial pressure as compared to evaporation of magnesium from pure Mg(s,l). When Mg_2Si is used as the Mg(g) source, only the 2MgO/Si product is observed without any formation of the unwanted $2MgO/Mg_2Si$ product. Figure 44 demonstrates the conversion of the SiO_2 inverse opal into a 2MgO/Si composite, followed by removal of the MgO phase to yield single phase silicon.

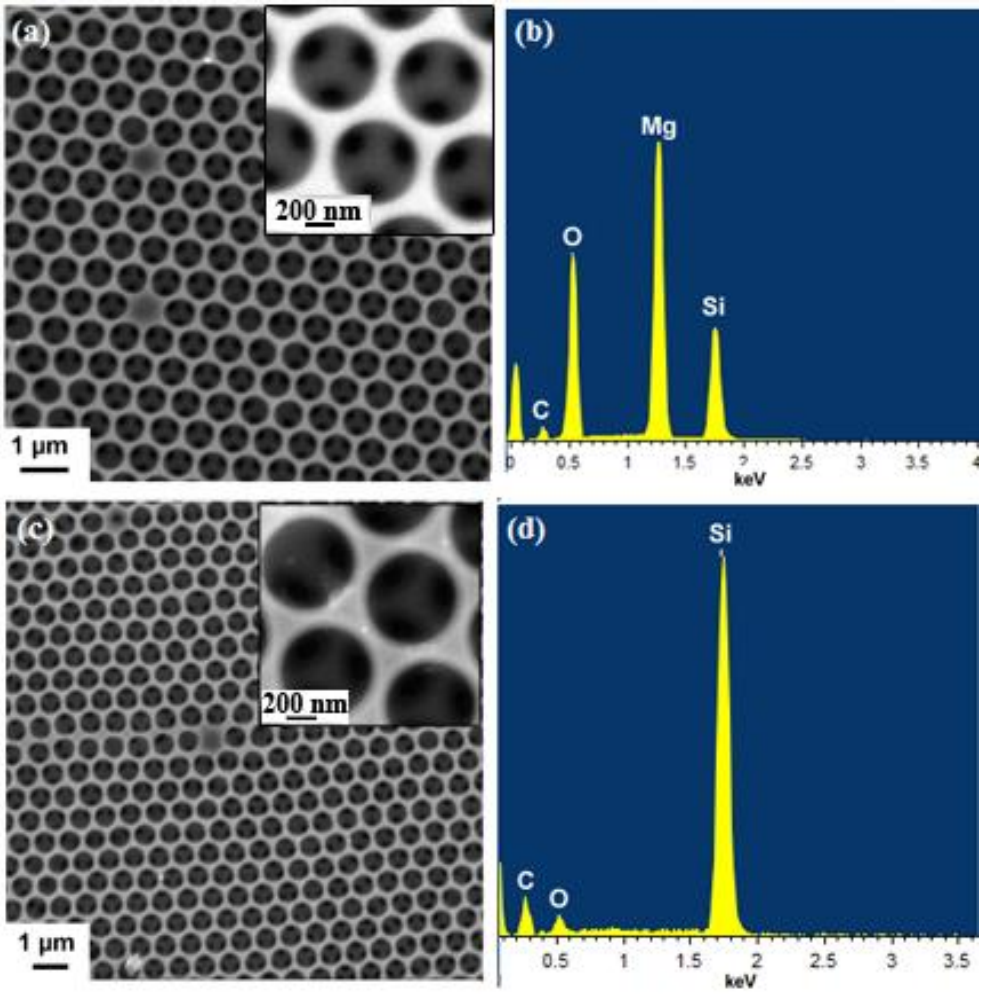

Figure 44: (a) SEM image of inverse opal after exposure to Mg(g) at 800°C for 12 hours to form MgO/Si composite; (b) EDX analysis of the inverse opal after reaction; (c) SEM image of the same inverse opal after dissolution of MgO in hydrochloric acid; (d) EDX analysis after dissolution of MgO.

Shape preservation of the inverse opals was excellent, and no changes to the periodic structure of the photonic could be observed from top-down imaging after reaction or the acid wash treatment. EDX analysis after the acid wash treatment showed little residual oxygen, confirming nearly complete magnesiothermic reduction. Subsequent exposure to hydrofluoric acid (30% w/w) for 10 minutes was utilized to remove any unreacted SiO_2 or SiO_2 which formed during the MgO dissolution in aqueous hydrochloric acid solution.

Conversion of the porous Si replica inverse opals into Mg_2Si is, in theory, straightforward. Mg_2Si is the only thermodynamically stable compound in the Mg-Si system and it is a line compound[116]. Therefore, no manipulation of magnesium vapor pressure is necessary in order to ensure constant stoichiometry or selective growth of the desired Mg_2Si compound. The partial pressure of magnesium vapor above pure Mg metal is sufficient to drive the reaction at all temperatures between 500-1000°C (Figure 45)[117].

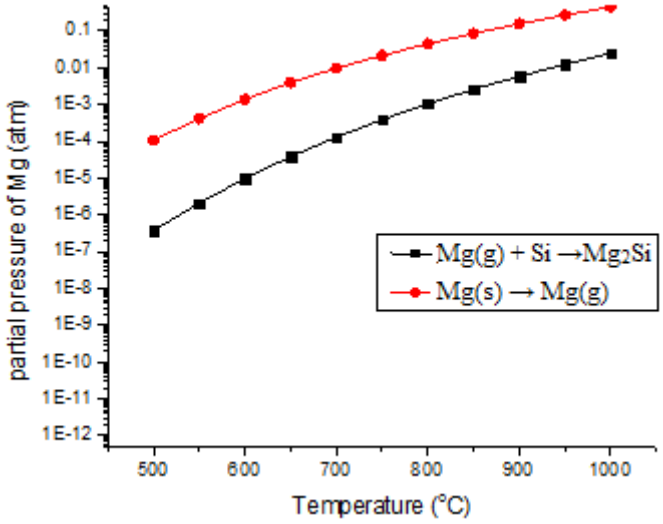

Figure 45: Equilibrium magnesium partial pressure necessary to drive Mg_2Si formation, and Mg(g) pressure generated via vaporization from pure Mg metal.[117]

Since the inverse opals are synthesized on a silicon substrate, prolonged exposure to magnesium vapor will result in undesired reaction of the substrate. Therefore, attempts were made to limit reaction conditions (i.e., temperature and time) to allow for complete reaction of the inverse opal while minimizing reaction of the substrate. In practice, the inverse opal tended to react much faster under less aggressive conditions than the substrate, likely because the silicon-replica inverse opals are highly porous (micro/mesopores are present due to magnesiothermic conversion[87], plus the larger primary pores inherent to the inverse opal structure).

A variety of reaction conditions were evaluated in both open atmospheres (i.e. pure flowing Ar or 4%/96% H_2/Ar mixtures) and closed atmospheres (i.e., iron crucibles welded under argon atmosphere, or glass ampoules sealed under static vacuum), using various magnesium sources (foil, granules, powder, etc.). In all cases, Mg_2Si formation was observed under sufficient temperatures and times. However, the techniques tended to vary in the uniformity of the reaction and the presence of contaminants (especially oxygen).

The most promising results were observed using a flow-through reactor as described in the experimental section. The reaction temperature had a significant effect on the morphology of the resulting Mg_2Si. The general inverse-opal structure could be observed at all temperatures, however higher temperatures resulted in significant coarsening of the Mg_2Si opal walls and degradation of the initial structure (i.e., faceting, distortion, and/or swelling of the sidewalls of inverse opal, see Figure 46). Decreasing the conversion temperature led to significantly improved shape-preservation, as shown in Figure 46.

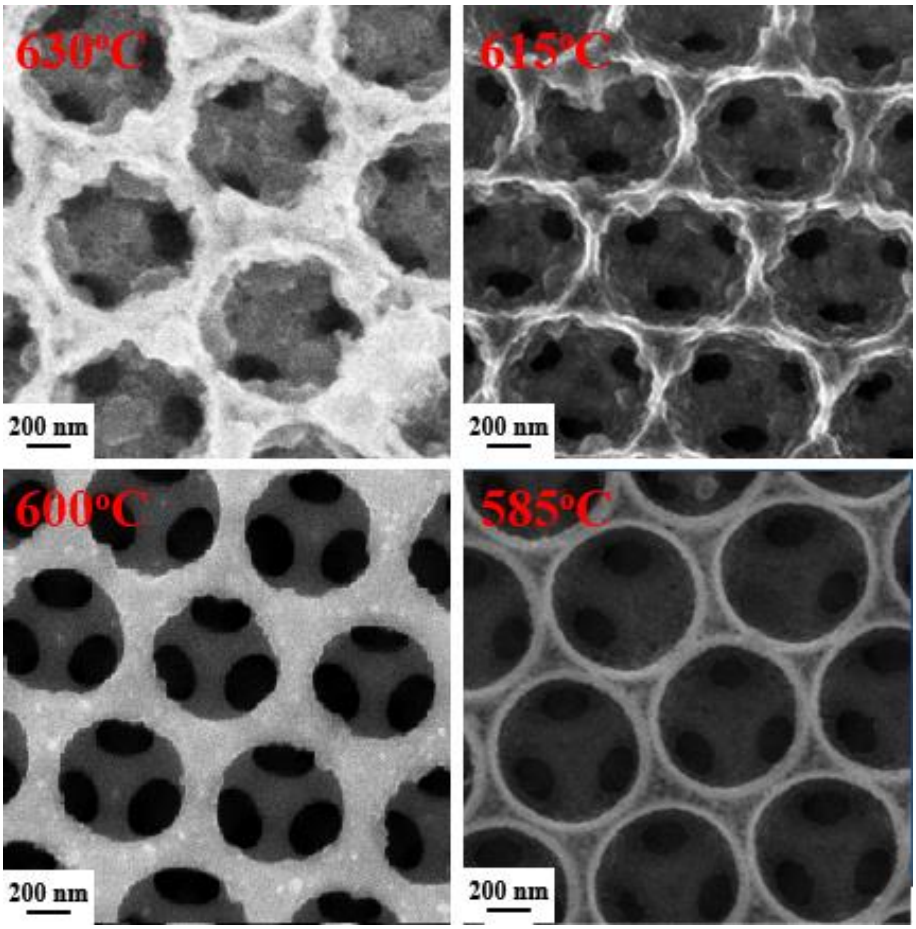

Figure 46: Inverse opal morphologies observed after conversion into Mg_2Si at various reaction temperatures for 4 hours.

Reaction temperatures of 585ºC resulted in very good shape preservation with negligible changes to the inverse opal structure. The main observable physical change between the as-synthesized SiO_2 inverse opals and the Mg_2Si replicas is a slight roughening of the initially smooth walls. This is consistent with the transformation of initially amorphous SiO_2 into nanocrystalline Mg_2Si. SEM images of the inverse opals at various magnifications after reduction to form Si replicas followed by subsequent exposure to magnesium vapor to form Mg_2Si replicas are shown in Figure 47. EDX analysis confirms the formation of Mg_2Si. The Mg:Si peak ratios in the EDX spectrum are similar to those for commercially available pure Mg_2Si powder (Alfa-Aesar, 99.5%

purity), suggesting nearly complete conversion of the silicon inverse opal replicas into Mg_2Si replicas. EDX analysis also indicates the presence of oxygen which, as will be discussed later, was unavoidable.

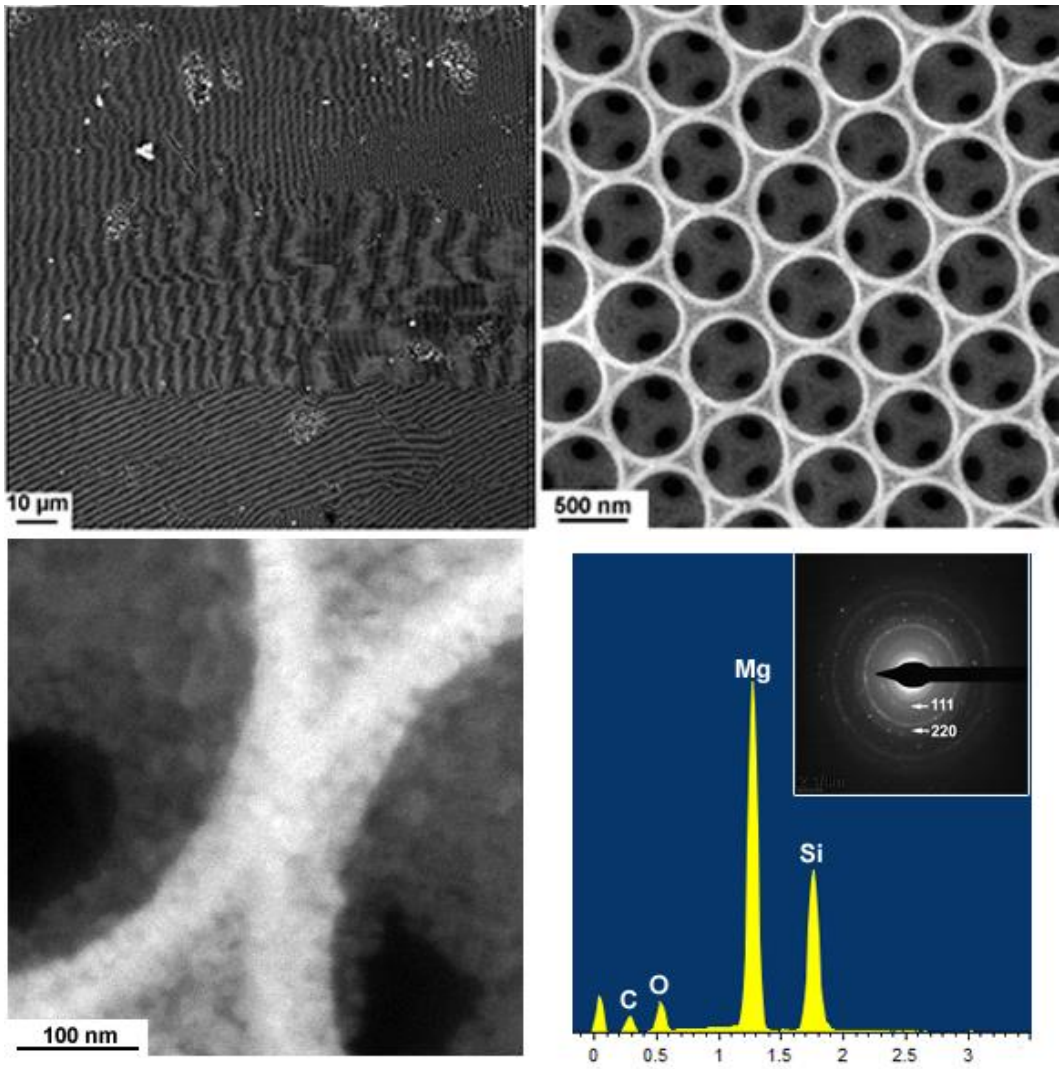

Figure 47: SEM images of as synthesized Mg_2Si inverse opals at various magnifications, as well as EDX spectra consistent with Mg_2Si and electron diffraction confirming Mg_2Si for reaction at 585°C for 2 hours.

TEM imaging further confirms the very strong shape retention after conversion to Mg_2Si (Figure 48). Quantitative analysis of 50 different pores observed in SEM images revealed a mean pore size of 624 nm with a standard deviation of 10.83 nm before in the as-received opals before reaction (slightly larger than, but still consistent with, the 610 nm

size which was expected). After reaction, mean pore size was determined to be 604 nm with a standard deviation of 24.93 nm. The slightly smaller pore size suggests some swelling of the opal walls, which is expected given the molar volume difference. The larger standard deviation was due, in part, to a higher density of defects or distortions in the opal structure after reaction.

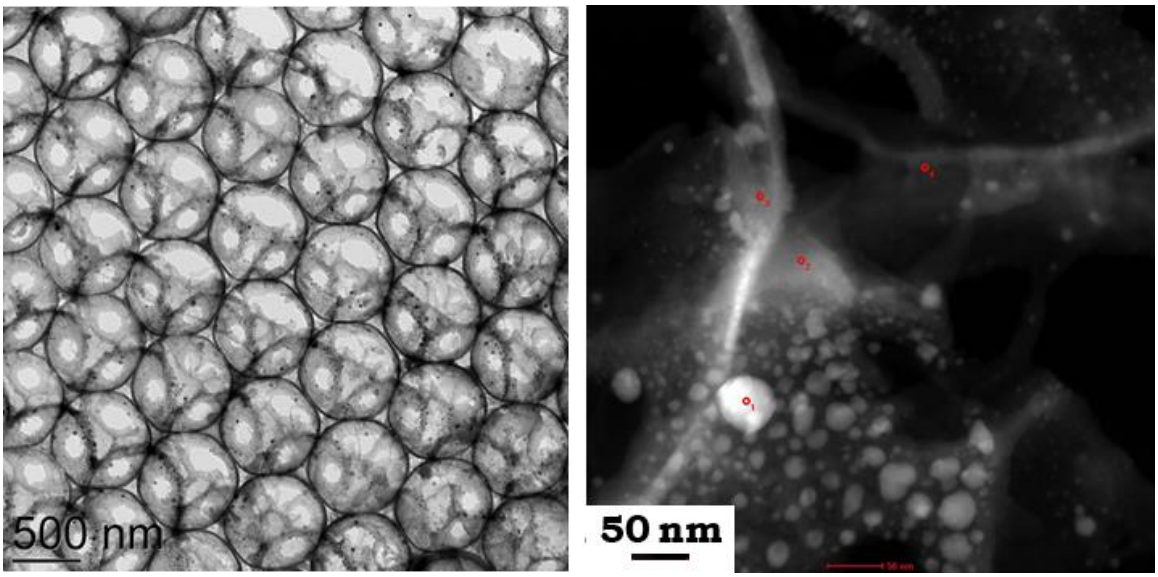

Figure 48: TEM images of inverse opals after conversion to Mg_2Si, confirming strong shape preservation of the inverse opal (left) and nanocrystalline character of the Mg_2Si (right).

2.6 Conversion of Biologically Derived SiO_2 Photonic Structures

In addition to synthetic photonic crystals, there are a number of natural, biologically-derived materials which possess photonic crystal-like structures and properties[118]. One example is the frustule of the diatom species *Coscinodiscus wailesii*, which is composed mostly of SiO_2 (with varying minor dopants depending on growth environment) arranged in a radially symmetric, intricate periodic pattern. Interrogation of light transmission through in-house cultured *Coscinodiscus wailesii* frustule, carried

out by our collaborators at the University of Arizona, reveals sharp diffraction patterns consistent with a 3D photonic structure (Figure 49).

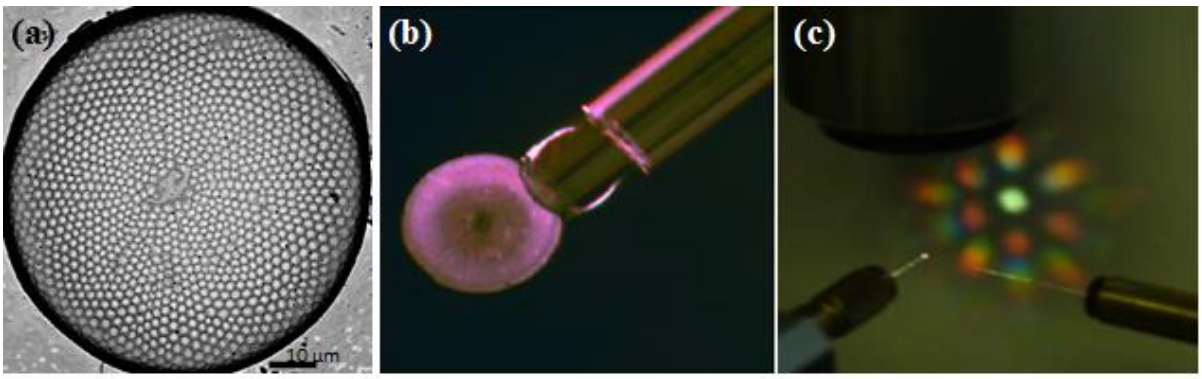

Figure 49: (a) SEM image of C. wailesii diatom frustule; (b) micrograph of frustule attached to an optical fiber; (c) diffraction pattern caused by light transmission through the frustule (unpublished, courtesy of Dr. Robert Norwood, University of Arizona).

Although there is less control over the structure obtained from the diatom frustule versus synthetic photonic crystals, diatoms can be grown relatively cheaply and in very large numbers. Such frustules have been proposed for use as light filters and surface enhanced Raman devices for ultrasensitive sensing[119]. In the long term, there is hope that understanding the genetic mechanism behind frustule growth will allow for manipulation of the frustule shape via genetic engineering[120]. However, similar to synthetic SiO_2 photonic crystals, the diatom frustules show only pseudo, or incomplete, photonic bandgaps. Finite difference time domain simulations of diatom frustules converted into Mg_2Si suggest that such material should possess a wide, complete bandgap centered at approximately 1.8 µm (Figure 50).

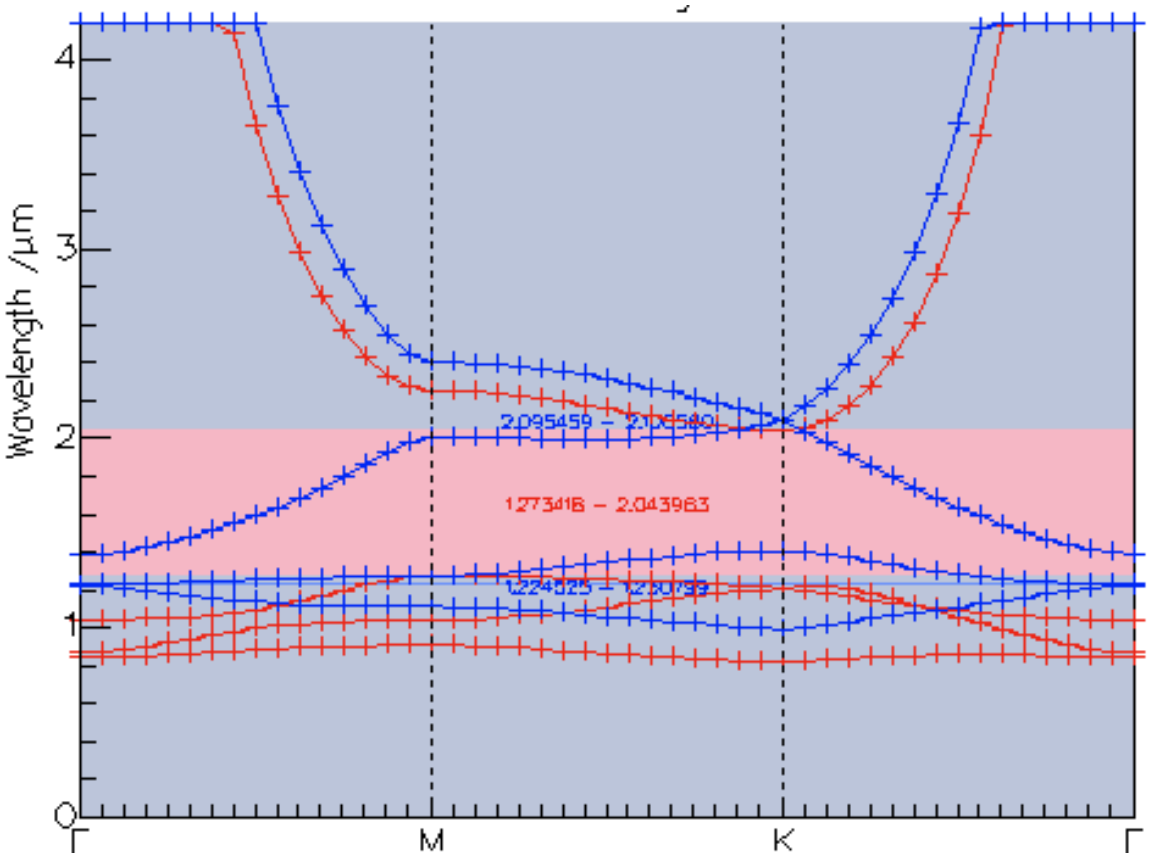

Figure 50: Simulation of in-plane light transmission through a Mg_2Si replica of a Coscinodiscus wailesii frustule. The light pink region is the bandgap.

Therefore, the SiO_2 to Mg_2Si transformation demonstrated previously in this chapter on synthetically fabricated inverse opals was evaluated on biologically derived diatom frustules. Such transformation may potentially yield naturally inherited photonic crystals with complete bandgaps in the near infrared. As cultured (in-house, courtesy Dr. Yunnan Fang) starting diatom frustules before reaction are shown in Figure 51.

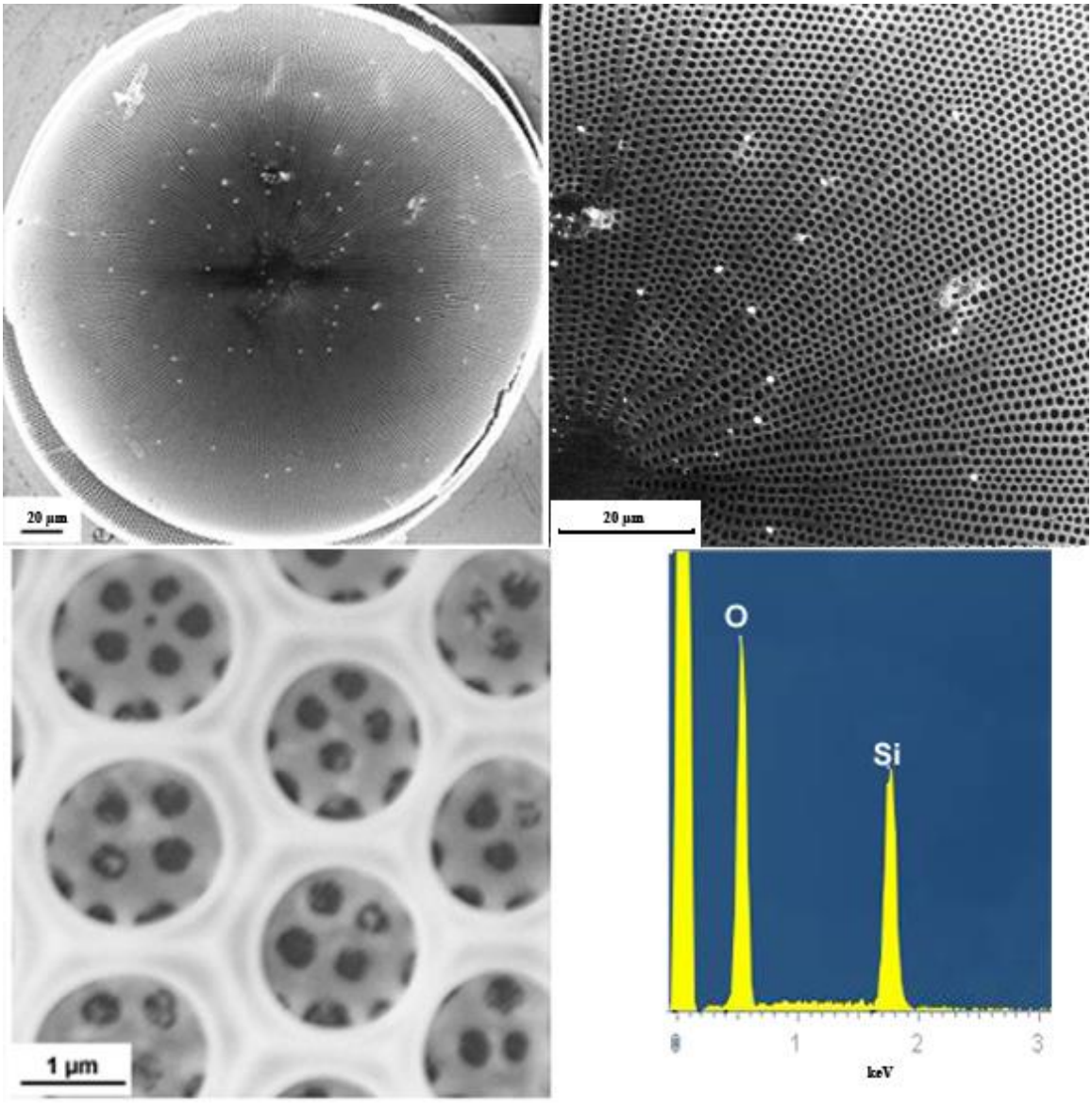

Figure 51: As-grown diatom frustules before reaction at various magnification, as well as EDX spectra confirming SiO_2.

Cleaned diatom frustules were drop-coated from an ethanolic suspension onto silicon substrates, and magnesiothermic reduction of the frustules was carried out in a flow-through reactor as described previously for the inverse opals and in the experimental section. Images and EDX spectra of the reduced frustules, before and after dissolution of MgO in HCl, are shown in Figure 52. Following the reaction, the EDX spectrum clearly

indicates the presence of a large amount of Mg in addition to the Si and O from the starting frustule, consistent with formation of a 2MgO/Si product. After washing in hydrochloric acid to remove the MgO, the only major remaining peak in the EDX spectra is Si with a very small amount of residual O, suggesting nearly complete reaction for the times and temperatures used. Some fractured or deformed diatom frustules could be observed. However, a large number of diatom frustules were found intact and maintained their starting photonic crystal-like structure. TEM imaging and electron diffraction of the frustules after removing the MgO confirmed they were composed of single phase, polycrystalline, porous silicon (CuO is present in the electron diffraction pattern due to sputtering of copper finger for TEM sample preparation).

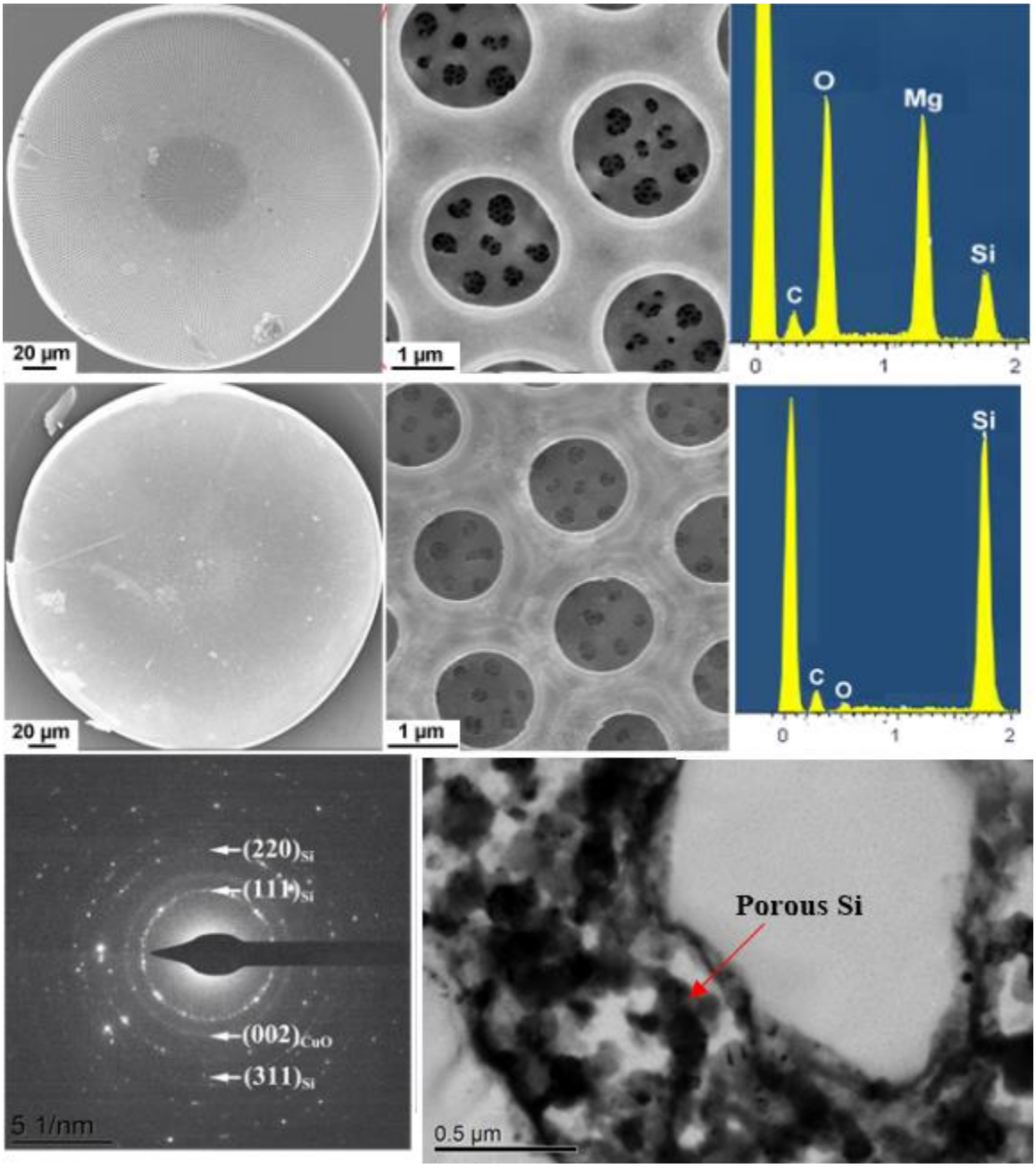

Figure 52: Top row: SEM images and EDX spectrum of diatom frustules after exposure to Mg(g) at 800ºC for 16 hours to form a 2MgO/Si composite. Middle row: SEM images and EDX spectrum of frustules after exposure to hydrochloric acid (3M, 2 hours) to remove MgO and yield single phase Si. Bottom row: Electron diffraction pattern confirming Si and TEM image of porous-Si replica.

The porous silicon frustules replicas were subsequently exposed to magnesium vapor using a similar setup to that described previously for inverse opals. Reaction times of 580ºC for 4 hours using vaporization of pure magnesium metal as the vapor source

were sufficient for complete reaction to form Mg_2Si replicas as determined by EDX and electron diffraction. No residual crystalline silicon peaks were observed by electron diffraction, suggesting complete reaction of the porous-silicon intermediate. The atomic ratio determined by the relative intensities of Mg:Si peaks in the EDX spectrum was consistent with fully converted, oxygen-contaminated Mg_2Si. As with the inverse opals, the walls of the polycrystalline Mg_2Si replicas showed some surface texture, especially when compared to the smooth walls of the initial amorphous SiO_2 .

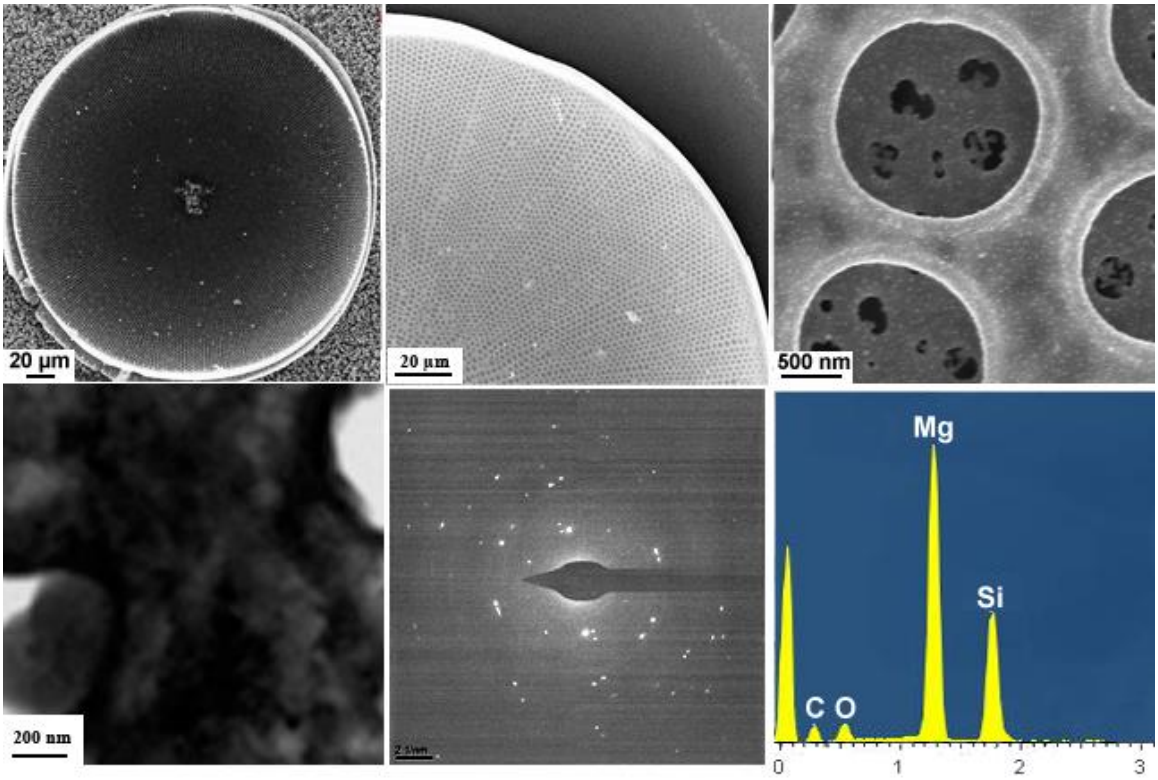

Figure 53: Top row: SEM images of Mg_2Si diatom frustules after reaction of por-Si replicas with Mg(g) at 580°C for 2 hours. Bottom row: TEM image of dense Mg_2Si diatom wall, electron diffraction pattern confirming the presence of Mg_2Si and EDX spectrum consistent with Mg_2Si with a small oxygen contamination.

2.7 Limitations and Future Direction

For the inverse opal samples, after some optimization of reaction conditions, high fidelity shape preservation could be achieved. A few cracks and large area defects could

be found in wide-area views after conversion; however, the as-fabricated initial SiO_2 inverse opals also contained some cracks and defects and so it could not be determined whether these cracks were formed by the conversion process or were present initially. In higher magnification views of single domains, very little change to the photonic structure was observed and a slight roughening of the sidewalls was the only major observable morphological change. A few times, sections of the inverse opal lifted-off the substrate during the hydrochloric acid wash. However, this was rare and, in general, the inverse opal maintained adherence to the substrate throughout the conversion process. While top-down imaging of the opal structure suggested high fidelity shape preservation, more detailed microscopic characterization (*i.e.*, TEM or SEM observation of cross sections of the opal structure) is necessary and underway to evaluate any swelling, shrinkage, or change of structure in the z-direction of the opal structure.

The diatom frustules appeared more prone to cracking and degradation than the inverse opals. After both the initial magnesiothermic reduction to form Si replicas, and the subsequent silicidation reaction to form Mg_2Si replicas, a large number of cracked, broken, or otherwise damaged frustules or fragments of frustules could be observed in the microscope. It is difficult to quantify what percentage of frustules remained intact since, even in the initial samples before any reaction, some frustules were cracked or broken during growth or washing steps. The adherence of the frustules to the substrate also presented some problems. Since the frustules were drop-coated onto the substrate before reaction, a number of the reacted frustules tended to come off the substrate during exposure to the hydrochloric acid solution. Nevertheless, due to the large number of individual frustules which were present on a single substrate, intact and crack-free

frustules could always be located (even if a significant portion of the initial frustules were either cracked or came off the substrate during washing) .

Quantitative optical evaluation of the Mg_2Si inverse opals and diatom frustule replicas is underway by collaborators (Dr. Joe Perry at Georgia Tech and Dr. Robert Norwood at University of Arizona, respectively). Optical testing of as-converted inverse opals can be performed directly on the substrate and is relatively straightforward. Evaluation of the frustules replicas, on the other hand, requires lifting the frustules off the substrate and attaching them to a fiber (see Figure 49). The frustules also had to be removed from the substrate in order to conduct TEM analyses. This was accomplished by placing a small amount of epoxy onto the tip of a needle and using a micromanipulator to bring the needle tip into contact with a frustule. Removing the frustule replicas from the substrate usually resulted in fracture of the frustule, and it was difficult to remove an entire frustule without breaking it. Although intact frustules replicas could be found on the substrate after conversion to Mg_2Si with excellent shape preservation, it appears that such replicas may be very mechanically fragile. Such fragility may inhibit the practical use of frustules replicas fabricated via the conversion process developed in this study. It should be noted, however, that attachment of frustules to a needle or fiber requires a significant degree of individual skill.

Another major issue concerning both the inverse opal and diatom samples is the presence of oxygen in the final Mg_2Si product. Since oxygen was not present in the silicon replicas, its introduction must come during the conversion to Mg_2Si. Oxygen contamination is a common issue for the synthesis of many magnesium-based composites[121]. Use of ultra high purity argon (oxygen content ~1 ppm, H_2O content ~2

ppm) without additional gettering as the reaction atmosphere resulted in substantial O_2 contamination (oxygen levels higher than 20% were observed). EDS mapping indicated that the oxygen is observed uniformly throughout the structure (Figure 54), while the lack of any oxide phases in the electron diffraction pattern (Figure 53) suggests such oxygen is present as an amorphous phase.

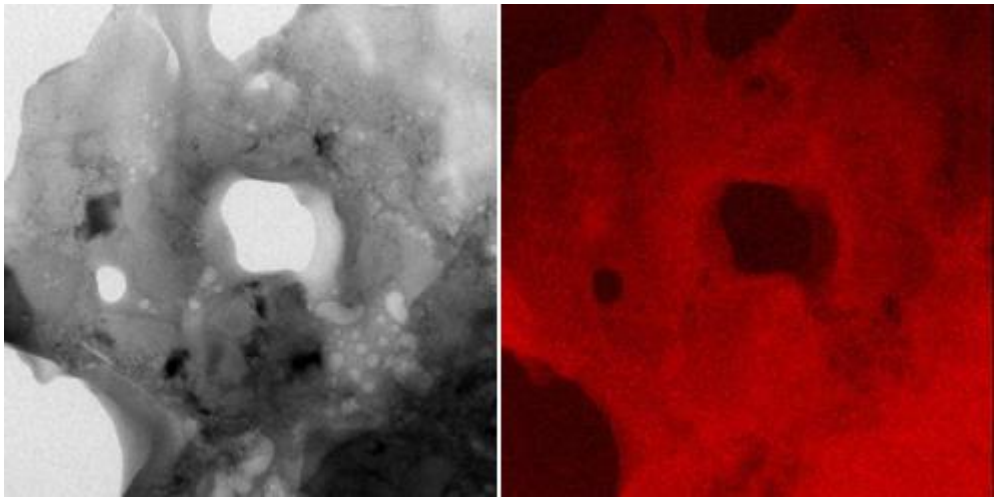

Figure 54: TEM image (right) and oxygen mapping via EFTEM (red represents oxygen) of an oxygen contaminated Mg_2Si frustule replica after reaction of por-Si replica with Mg(g) at 580^oC for 2 hours.

Attempts to mitigate oxygen contamination included utilization a titanium getter with an oxygen sensor to lower initial oxygen levels below 1E-17 atm and passage of argon over a heated mixture of Ti powder to further reduce oxygen and water content, as outlined in the experimental section. While such measures helped somewhat, oxygen levels of approximately 10% were still often observed in the final Mg_2Si replica. Because oxides (either MgO or magnesiosilicates) have refractive indices much lower than Mg_2Si, the inclusion of oxygen in the photonic structure is undesirable, since it will lower the overall effective refractive index of the material. Carrying out the conversion to Mg_2Si under vacuum conditions (<1E-5 torr) resulted in higher levels of oxygen than under

argon atmospheres. In order to further reduce oxygen contamination, it may help to sinter the silicon replicas after magnesiothermic reduction in order to increase the silicon grain size, decrease surface area, and perhaps decrease reactivity. Alternatively, in the synthesis of MgB_2 films, specialized reactor designs and the use of high hydrogen gas pressures have been shown to inhibit oxygen contamination in resulting films, and similar strategies may be applicable to Mg_2Si synthesis in order to further mitigate oxygen contamination[122].

2.8 Conclusions

A method for the conversion of intricate, three dimensional SiO_2 structures into Mg_2Si replicas was successfully developed and demonstrated on both synthetically fabricated photonic templates (inverse opals) and biologically derived photonic templates (frustules of the *Coscinodiscus wailesii* diatom). In each case, the structure of the resulting Mg_2Si was inherited from the starting SiO_2 material. Some oxygen contamination was observed in the final Mg_2Si product. Due to the significant increase in refractive index on conversion from SiO_2 to Mg_2Si, the Mg_2Si photonic crystals may show complete photonic bandgaps in three-dimensions in the near infrared. Optical testing of each type of photonic structure is underway.

2.9 References

[85] Breslin, M. C., et al. "Alumina/Aluminum Co-continuous Ceramic composite (C4) Materials Produced by Solid/Liquid Displacement Reactions: Processing Kinetics and Microstructure." *18th Annual Conference on Composites and Advanced Ceramic Materials-A: Ceramic Engineering and Science Proceedings, Volume 15*. No. 4. John Wiley & Sons, 2009.

Fahrenholtz, William G., et al. "Near-Net-Shape Processing of Metal-Ceramic Composites by Reactive Metal Penetration." *Journal of the American Ceramic Society* 79.9 (1996): 2497-2499.

[86] Saiz, Eduardo, and Antoni P. Tomsia. "Kinetics of Metal-Ceramic Composite Formation by Reactive Penetration of Silicates with Molten Aluminum." *Journal of the American Ceramic Society* 81.9 (1998): 2381-2393.

[87] Bao, Zhihao, et al. "Chemical reduction of three-dimensional silica micro-assemblies into microporous silicon replicas." *Nature* 446.7132 (2007): 172-175.

[88] Sandhage, Kenneth H., et al. "Novel, Bioclastic Route to Self-Assembled, 3D, Chemically Tailored Meso/Nanostructures: Shape-Preserving Reactive Conversion of Biosilica (Diatom) Microshells." *Advanced Materials* 14.6 (2002): 429-433.

[89] Richman, Erik K., et al. "Ordered mesoporous silicon through magnesium reduction of polymer templated silica thin films." *Nano letters* 8.9 (2008): 3075-3079.

[90] Szczech, Jeannine R., and Song Jin. "Mg_2Si nanocomposite converted from diatomaceous earth as a potential thermoelectric nanomaterial." *Journal of Solid State Chemistry* 181.7 (2008): 1565-1570.

[91] Unocic, Raymond R., et al. "Anatase assemblies from algae: coupling biological self-assembly of 3-D nanoparticle structures with synthetic reaction chemistry." *Chem. Commun.* 7 (2004): 796-797.

Sandhage, Kenneth H., et al. "Inorganic preforms of biological origin: Shape-preserving reactive conversion of biosilica microshells (diatoms)." *Handbook of Biomineralization:. Biomimetic and bioinspired chemistry* 2 (2007).

[92] Shian, Samuel, et al. "Three-Dimensional Assemblies of Zirconia Nanocrystals Via Shape-Preserving Reactive Conversion of Diatom Microshells." *Journal of the American Ceramic Society* 89.2 (2006): 694-698.

[93] Yablonovitch, Eli. "Inhibited spontaneous emission in solid-state physics and electronics." *Physical review letters* 58.20 (1987): 2059.

[94] Joannopoulos, John D., Pierre R. Villeneuve, and Shanhui Fan. "Photonic crystals: putting a new twist on light." *Nature* 386.6621 (1997): 143-149.

Vlasov, Yurii A., et al. "On-chip natural assembly of silicon photonic bandgap crystals." *Nature* 414.6861 (2001): 289-293.

[95] Vlasov, Yu A., et al. "Manifestation of intrinsic defects in optical properties of self-organized opal photonic crystals." *Physical Review E* 61.5 (2000): 5784.

[96] Busch, Kurt, and Sajeev John. "Photonic band gap formation in certain self-organizing systems." *Physical Review E* 58.3 (1998): 3896.

[97] Ullal, Chaitanya K., et al. "Photonic crystals through holographic lithography: Simple cubic, diamond-like, and gyroid-like structures." *Applied Physics Letters* 84.26 (2004): 5434-5436.

Cumpston, Brian H., et al. "Two-photon polymerization initiators for three-dimensional optical data storage and microfabrication." *Nature* 398.6722 (1999): 51-54.

[98] Blanco, Alvaro, et al. "Large-scale synthesis of a silicon photonic crystal with a complete three-dimensional bandgap near 1.5 micrometres." *Nature* 405.6785 (2000): 437-440.

[99] Jiang, Peng, and Michael J. McFarland. "Large-scale fabrication of wafer-size colloidal crystals, macroporous polymers and nanocomposites by spin-coating." *Journal of the American Chemical Society* 126.42 (2004): 13778-13786.

[100] Jiang, P., et al. "Single-crystal colloidal multilayers of controlled thickness." *Chemistry of Materials* 11.8 (1999): 2132-2140.

Wong, Sean, Vladimir Kitaev, and Geoffrey A. Ozin. "Colloidal crystal films: advances in universality and perfection." *Journal of the American Chemical Society* 125.50 (2003): 15589-15598.

[101] Holland, Brian T., Christopher F. Blanford, and Andreas Stein. "Synthesis of macroporous minerals with highly ordered three-dimensional arrays of spheroidal voids." *Science* 281.5376 (1998): 538-540.

[102] Chabanov, Andrey A., Yoonho Jun, and David J. Norris. "Avoiding cracks in self-assembled photonic band-gap crystals." *Applied physics letters* 84.18 (2004): 3573-3575.

McLachlan, Martyn A., et al. "Thin film photonic crystals: synthesis and characterisation." *Journal of Materials Chemistry* 14.2 (2004): 144-150.

[103] Hatton, Benjamin, et al. "Assembly of large-area, highly ordered, crack-free inverse opal films." *Proceedings of the National Academy of Sciences* 107.23 (2010): 10354-10359.

[104] Mishchenko, Lidiya, et al. "Patterning Hierarchy in Direct and Inverse Opal Crystals." *small* 8.12 (2012): 1904-1911.

[105] Tétreault, Nicolas, et al. "Dielectric planar defects in colloidal photonic crystal films." *Advanced Materials* 16.4 (2004): 346-349.

Massé, Pascal, et al. "Tailoring planar defect in three-dimensional colloidal crystals." *Chemical physics letters* 422.1 (2006): 251-255.

[106]Moon, Jun Hyuk, and Shu Yang. "Chemical aspects of three-dimensional photonic crystals." *Chemical reviews* 110.1 (2009): 547-574.

Ibisate, Marta, Dolores Golmayo, and Cefe López. "Silicon direct opals." *Advanced Materials* 21.28 (2009): 2899-2902.

Pallavidino, Luca, et al. "Synthesis of amorphous silicon/magnesia based direct opals with tunable optical properties." *Optical Materials* 33.3 (2011): 563-569.

Gallego-Gómez, Francisco, et al. "Light Emission from Nanocrystalline Si Inverse Opals and Controlled Passivation by Atomic Layer Deposited Al_2O_3." *Advanced Materials* 23.44 (2011): 5219-5223.

Mishchenko, Lidiya, et al. "Colloidal co-assembly route to large-area high-quality photonic crystals." *SPIE OPTO*. International Society for Optics and Photonics, 2011.

[107] Mackenzie, John D. "Glasses from melts and glasses from gels, a comparison." *Journal of Non-Crystalline Solids* 48.1 (1982): 1-10.

[108] *Powder Diffraction File* Card No. 27–1402 for Si, Card No. 45–946 for MgO, Card No. 35–0773 for Mg_2Si (International Center on Diffraction Data, Newtown Square, Pennsylvania); ⟨www.icdd.com⟩.

[109] Bao, Zhihao. "Conversion of 3-D nanostructured biosilica templates into non-oxide replicas." (2008).

[110] Wolfe, William L. *Handbook of optics*. Vol. 2. McGraw-Hill, 2001.

[111] Kato, Takashi, Yuichiro Sago, and Hiroyuki Fujiwara. "Optoelectronic properties of Mg_2Si semiconducting layers with high absorption coefficients." *Journal of Applied Physics* 110.6 (2011): 063723-063723.

[112] McWilliams, D., and D. W. Lynch. "Indexes of Refraction of Mg_2Si, Mg_2Ge, and Mg_2Sn." *JOSA* 53.2 (1963): 298_1-299.

[113] Szczech, Jeannine R., and Song Jin. "Mg_2Si nanocomposite converted from diatomaceous earth as a potential thermoelectric nanomaterial." *Journal of Solid State Chemistry* 181.7 (2008): 1565-1570.

[114] Van Stryland, E., D. Williams, and W. Wolfe. *Handbook of Optics*. Ed. Michael Bass. McGraw-Hill, 1996.

[115] Garahan, Anna, et al. "Optical Properties of Nanocomposite Thin-Films." *ASME 2006 International Mechanical Engineering Congress and Exposition*. American Society of Mechanical Engineers, 2006.

[116] Okamoto, H. "Mg-Si (Magnesium-Silicon)." *Journal of Phase Equilibria and Diffusion* 28.2 (2007): 229-230.

[117] Barin, Ihsan, et al. *Thermochemical data of pure substances*. Vol. 6940. Weinheim: VCH, 1993.

[118] Vukusic, Pete, and J. Roy Sambles. "Photonic structures in biology." *Nature* 424.6950 (2003): 852-855.

[119] Norwood, R. A. "Biological and biologically inspired photonic materials and devices." *SPIE NanoScience+ Engineering*. International Society for Optics and Photonics, 2013.

[120] Kröger, Nils. "Prescribing diatom morphology: toward genetic engineering of biological nanomaterials." *Current opinion in chemical biology* 11.6 (2007): 662-669.

[121] Janakiraman, Narayanan, et al. "Synthesis and phase evolution of Mg–Si–C–N ceramics prepared by pyrolysis of magnesium-filled poly (ureamethylvinyl) silazane precursor." *Journal of Materials Chemistry* 16.39 (2006): 3844-3853.

Zhai, H. Y., et al. "Superconducting magnesium diboride films on Si with $T_{c0}\sim$ 24 K grown via vacuum annealing from stoichiometric precursors." *Applied Physics Letters* 79.16 (2001): 2603-2605.

[122] Rowell, John. "Magnesium diboride: Superior thin films." *Nature Materials* 1.1 (2002): 5-6.

Zeng, Xianghui, et al. "In situ epitaxial MgB_2 thin films for superconducting electronics." *Nature materials* 1.1 (2002): 35-38.

Chapter 3: Conversion of SiO2 Photonic Crystal Fibers into IR-Transparent Replicas

3.1 *Summary*

Hollow core photonic crystal fibers (HC-PCF's) are a relatively new class of optical fibers which consist of a hollow core surrounded by a two dimensional photonic crystal. Such fibers have a remarkable ability to concentrate very high intensities of light in a small area, and have attracted attention in a variety of fields. Fabrication of SiO_2 photonic crystal fibers is relatively straightforward using well-developed stack-and-draw techniques. Unfortunately, the transparency range of SiO_2 is limited to wavelengths of approximately 2 μm or less. Significant effort has been put into adapting current fabrication methods to allow for the production of photonic crystal fibers composed of alternate materials which show enhanced transparency over a wider range of IR wavelengths. However, only limited success has resulted from these efforts and the fabrication of near- to mid-IR-transparent photonic crystal fibers still represents a substantial challenge. In this chapter, the shape-preserving conversion of SiO_2 photonic crystal fibers into infrared transparent MgF_2 replicas is explored.

3.2 *Background of Photonic Crystal Fibers*

Optical fibers were first theoretically described in the 1960's, initially developed in the 1970's, and by the end of the 20th century formed the foundation of the global communication network[123]. Traditional optical fibers are based on a principle known as *total internal reflection*, in which a high-index fiber core is surrounded by a lower-index cladding. Due to the refractive index contrast between the core and the cladding, when light contained in the core of the fiber strikes the core/cladding interface below a certain

angle, it is nearly completely reflected back into the core[124]. As a result, light is contained in the solid core of the fiber and can travel long distances in low absorption media, even if the fiber is curved up to a certain critical radius. These type of optical fibers, known as *step-index fibers*, revolutionized the field of telecommunications, and, in 2009, Dr. Charles Kao was awarded the Nobel Prize for his contributions to their development.

In the 1990's, an alternative mechanism for waveguiding through a fiber was proposed by Dr. Philip Russell[125]. Russell described a fiber consisting of a hollow air-core surrounded by a two dimensional photonic crystal (Figure 55). Russell suggested that illumination of a fiber consisting of a hollow core/photonic crystal cladding with light of a wavelength in the photonic crystal's forbidden range would result in complete containment of the light in the core of the fiber. It was theorized that the photonic crystal cladding would completely reflect incident light rays back into the core. In conventional step-index fibers, the low-loss limit is determined by scattering and absorption of the solid glass core[126]. Guiding light through a *hollow* core could potentially allow for significantly higher energy densities and extremely low losses without any intrinsic material limitations[127]. Such fibers are known as HC-PCF (*hollow core photonic crystal fibers)* or HC-PBG fibers (*hollow core photonic bandgap fibers).*

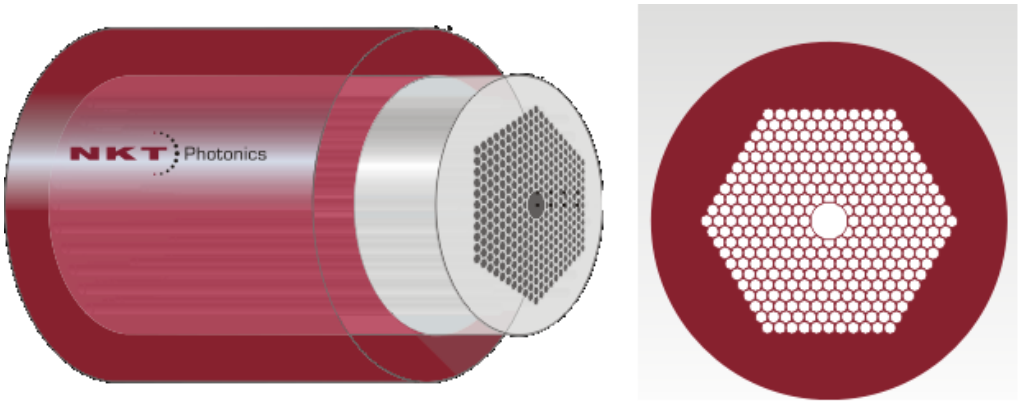

Figure 55: Schematic (from NKT Photonics)[128] of HC-PCF showing hollow core surrounded by photonic crystal cladding.

Hollow-core photonic crystal fibers have successfully been fabricated by a variety of groups using a *stack and draw* method, in which tubes are stacked in the desired pattern to create a macroscopic preform which is then heated to ~2000^{o}C and drawn down to fiber (Figure 56)[129]. HC-PCF's with various core and cladding geometries can be purchased commercially from several companies at lengths of several meters.

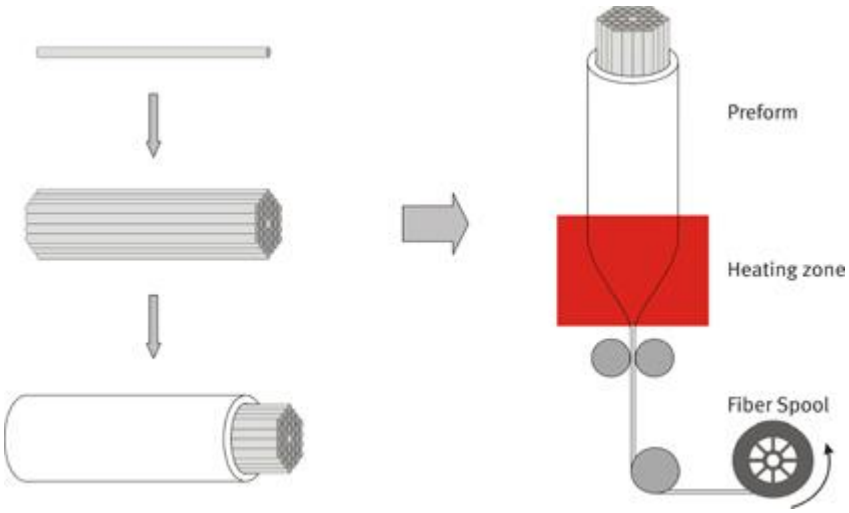

Figure 56[130]: Stack and draw method for fabrication of hollow core PCF's with various axial geometries.

Due to their complexity and high fabrication cost relative to conventional fibers, HC-PCF's do not appear likely to replace step-index fibers in the field of

telecommunications. However, there are numerous specialized applications in fields *outside* of traditional telecommunications that have driven research into HC-PCF's. The most substantial impacts of HC-PCF's are for applications which require the interaction of light with matter, particularly gases. As light in an HC-PCF is concentrated nearly entirely in the hollow-core, filling the core with a gas allows for maximizing the overlap between light and gas in a very small cross-sectional area over a nearly arbitrary length—HC-PCF's can therefore serve as nearly perfect spectroscopic gas-cells. The effective laser-matter interactions observed with HC-PCF's are several orders of magnitude larger than for conventional laser or gas-cell systems[131].

There are a number of fields which have exploited the significantly enhanced light-matter interaction capability of HC-PCFs. An example is Raman spectroscopy of molecular gases, in which the interaction of molecular vibrations of the gas with pulses of laser light causes a shift in the observed wavelength of the laser. Conventional Raman scattering measurements require high power lasers (>1MW) to achieve Raman threshold (above which a major fraction of the laser power is converted into the Stokes frequency)[132]. Utilization of an HC-PCF filled with hydrogen gas allowed for use of a laser 100 times less powerful than conventional techniques to reach the Raman threshold[133]. For similar reasons, HC-PCFs have also been used as near-infrared spectroscopic gas sensors[134]. More exotic quantum phenomena which rely on laser-matter interactions, such as atom and particle guidance via laser power,[135] electromagnetically induced transparency,[136] and supercontinuum generation have also benefited from the use of HC-PCFs.[137]

3.3 *Motivation and Approach*

Nearly all functional HC-PCF's, including all commercially available fibers, are fabricated from silica glass. While silica is transparent in the visible region of the spectrum, it absorbs strongly at wavelengths above approximately 2.4 μm (Figure 57). There is a demand for HC-PCF's which can operate in the mid-infrared, above the usable wavelength for SiO_2. For gas sensing, a field in which HC-PCF's have shown promise (as discussed in the previous section), a number of hazardous gases of interest in sensing fields show strong absorption bands in the mid-IR region of ~3-8 μm (for example, NO, N_2O and NO_2, CO and CO_2, N_2O, and CH_4 among many others)[138]. Infrared transparent HC-PCF's could also have medical applications. The Er:YAG laser, with emission of 2.9 μm, has been utilized for a variety of surgical applications including bone and tissue-cutting[139]. HC-PCF's have been proposed as a method to allow for flexible delivery of such laser with very high power densities, which could significantly increase the usefulness of Er:YAG for surgical applications. In addition, the US Naval Research Laboratory has recognized a need for a delivery system capable of very high laser power transmission in the 2-5μm range for missile defense[140] and has invested heavily in HC-PCF's as a potential solution.

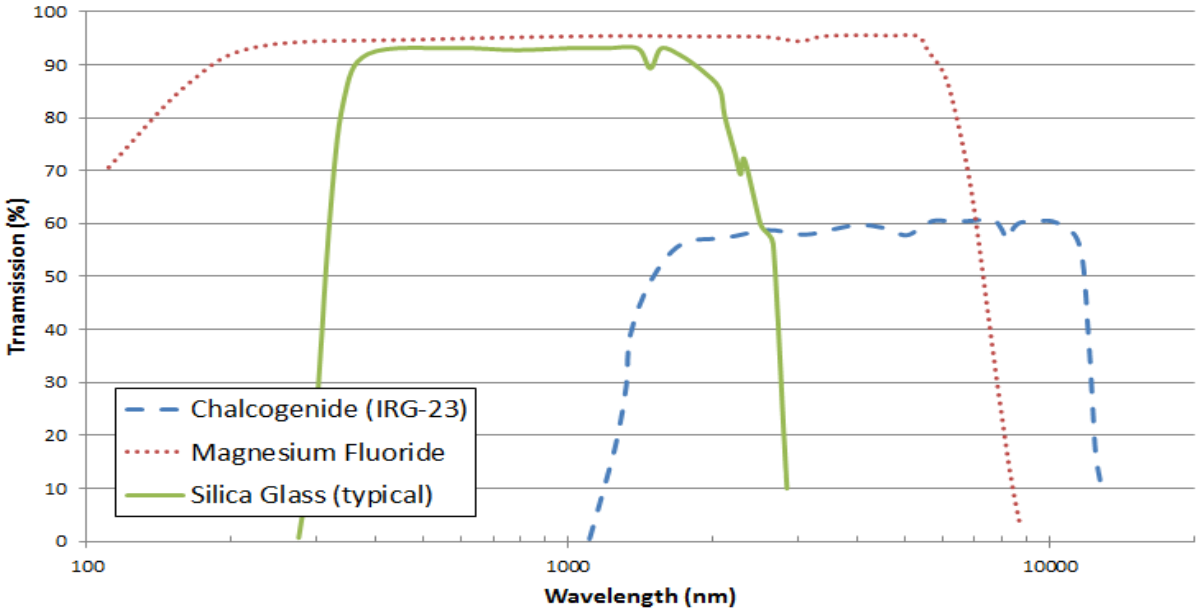

Figure 57: IR transparency of various materials (shown for 10mm thick samples)[141].

There has, therefore, been a recent focus on the development of optical fibers from materials which are transparent in the mid-IR. The overwhelming majority of these efforts have focused on the direct fabrication of hollow core fibers made of chalcogenide glasses, which have usable transmission ranges of approximately 1-11 µm depending on the exact composition[142]. One source estimates that the US Naval Research Laboratory has spent $30 million over the past 10 years developing chalcogenide fibers[143]. However, fabrication routes for chalcogenide fibers are substantially less advanced than for silica fibers. The stack and draw method used for fabrication of SiO_2 HC-PCF's is difficult with chalcogenide glasses due to the similarity between the drawing temperature and the crystallization temperature, and development of alternate methods (such as extrusion or casting) lag well behind silica fiber fabrication capabilities[144] and are relatively time-consuming and expensive[145]. Furthermore, the refractive index of chalcogenide glasses (n = 2.4-2.7)[146] is significantly higher than silica glass (n ~ 1.46), and simulations have

suggested that the band-gap on which SiO_2 HC-PCFs are based is lost for refractive indices larger than ~2[146]. While it may be possible to exploit a different type of bandgap, such fibers would require modified designs and substantially higher air-fractions.

An ideal material for mid-IR compatible HC-PCF's for sensing, medical, and military applications needs to satisfy several criteria. First, it should show a high transparency value over a relatively large wavelength range in the mid-IR. For sensing applications, in which the fiber will presumably be exposed to atmospheres containing various gases, the fiber material should be chemically inert and not react under exposure to such vapors. For medical and military applications, in which very high power densities are desirable, the fiber material should have a high melting point so that localized thermal heating caused by such high power densities does not result in melting or undesirable sintering or appreciable alterations in grain structure (thermal damage has been observed in fibers based on low melting polycrystalline silver halides, for example)[147].

One potential candidate which satisfies these criteria is magnesium fluoride, MgF_2. Magnesium fluoride is highly transparent over a wavelength range of 0.12–7 μm[148], is relatively stable and unreactive (including showing high resistance to water, oxygen, and a number of organic and halogen vapors[149]), has a relatively high melting point (T_m=1,263ºC), and is resistant to thermal and mechanical shock[150]. Due to these properties, MgF_2 is commonly used as an inert and transparent window for various spectroscopic applications[151]. The refractive index of MgF_2 is between 1.3-1.4 at wavelengths of 1-7 μm[114]. However, photonic crystal fibers of MgF_2 (or, in fact, MgF_2 based fibers of any type) have never been reported, presumably because there is no method for their fabrication.

In this chapter, the shape preserving transformation of SiO_2 hollow-core photonic crystal fibers into MgF_2 replicas is proposed and investigated. The transformation involves a two-step process in which fibers are first converted into MgO replicas, followed by conversion of MgO into MgF_2. The conversion of SiO_2 structures into MgO has been demonstrated previously[88], and has involved reaction with Mg(g) at temperatures $\geq$ 900°C. As with a standard magnesiothermic reduction, exposure of SiO_2 to magnesium gas results in the formation of MgO and reduction of silicon. Due to the high reaction temperatures utilized, the reduced silicon dissolved in a Mg-Si liquid product which migrated out of the solid structure to leave single phase MgO as the only solid phase product (reaction 4.1):

$$\mathbf{SiO_2\,(s)} + (2+x)Mg(g) \rightarrow \mathbf{2MgO(s)} + \{xMg\text{–}Si\}(l) \qquad (4.1)$$

In the reaction shown, {xMg-Si} refers to silicon dissolved in a magnesium rich, Mg-Si liquid[88]. This reaction has been demonstrated previously to yield MgO diatom frustule replicas. In this chapter, a similar reaction will be investigated for use on HC-PCF's to form MgO replicas of photonic crystal fibers. Furthermore, it is well known that exposure of MgO to hydrofluoric acid yields MgF_2 (reaction 4.2)[152].

$$\mathbf{MgO(s)} + 2HF(a) \rightarrow \mathbf{MgF_2(s)} + H_2O(l) \qquad (4.2)$$

Since the resulting MgF_2 is highly insoluble in water (0.013 g/100 mL)[153], it is possible that the magnesium fluoride product will retain the structure of the initial MgO (although this has not been demonstrated previously). Such a two-step process incorporating reactions 4.1 and 4.2 could therefore, in theory at least, be used to convert

SiO_2 photonic crystal fibers into MgF_2 replicas which maintain photonic behavior but possess high transparency in the near to mid-IR. The volume of the two moles of MgF_2 produced (39.6 cc)[154] is slightly larger than the volume of one mole of starting SiO_2 (~28 cc), and so the MgF_2 product is expected to be fully dense (which is desirable, since porous structures can act as scattering centers). Theoretically, conversion of a SiO_2 template into an MgO replica, via a 2MgO/Si intermediate, will result in MgO with approximately 35% residual porosity due to molar volume differences. Partial conversion of ~70% (molar basis) of the MgO into MgF_2 is sufficient to fill the residual porosity, while complete conversion of MgO to MgF_2 should, theoretically, lead to some swelling of the structure.

It is known that MgO produced via the shape-preserving transformation of SiO_2 templates is polycrystalline. After exposure to HF acid, the resulting MgF_2 will almost certainly be polycrystalline. Since grain boundaries can scatter light, polycrystalline materials generally show reduced optical transparency relative to single crystal materials (the transparency values shown in Figure 57 are for single crystal or amorphous materials). However, this affect is much more pronounced for lower wavelengths of light (i.e., the visible or UV) and large grains; in the mid infrared-region, grain boundaries have been shown to have little effect on transparency for MgF_2 materials, especially for grains less than <500 nm or so in size (Figure 58)[155].

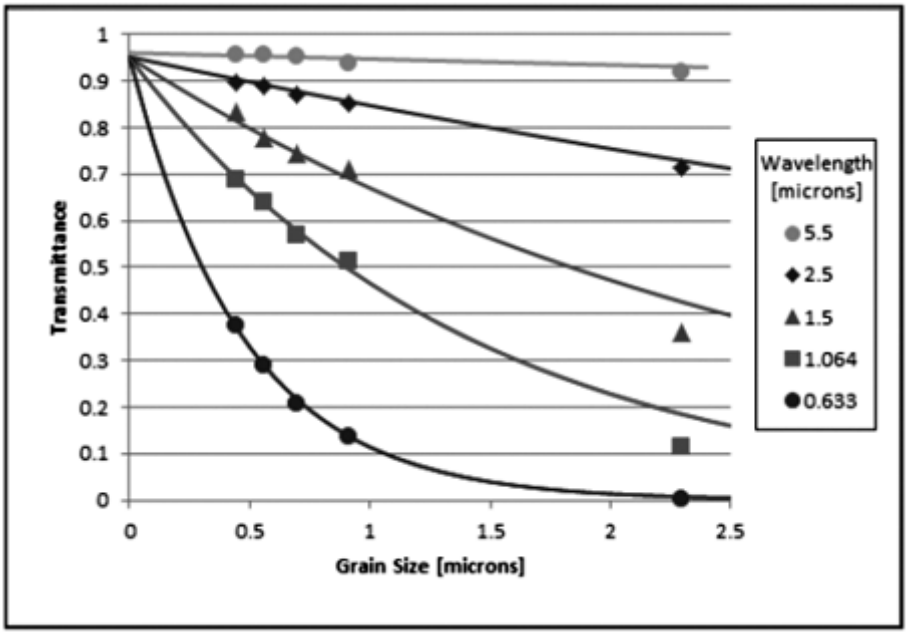

Figure 58[155]: Effect of grain size on optical transmittance of polycrystalline MgF_2 at various wavelengths.

Due to the additional complexity and processing steps associated with the shape-preserving transformation, fabrication of multi-meter long MgF_2 photonic crystal fibers (such as those required for telecommunications) via such a process will require further process development for scale-up. However, as discussed previously, such a process may find more immediate use in specialized areas, such as gas or Raman sensing or short-haul, high power medical delivery systems, where shorter lengths of fiber are sufficient (enhanced Raman sensing, for example, has utilized photonic crystal fibers as short as a few centimeters[156].

3.4 *Experimental Methods*

Hollow-core photonic crystal fibers made of SiO_2 were purchased from Thorlabs (New Jersey, USA). The fibers consist of a 14.5 $^{+}/_{-}$ 2 µm hollow core, surrounded by a photonic crystal with outer diameter of 73 µm, a dense silica cladding with outer

diameter of 155 μm, and finally a polyacrylate coating with outer diameter of 275 μm. The outer polyacrylate coating serves to enhance flexibility of the fiber, and its removal was necessary in order to cleave the fibers for further processing. The polyacrylate was removed from the fiber via immersion in neat sulfuric acid at 190^{o}C for 30 seconds. The fiber was then cleaved into 5 cm sections, using special handling methods so as not to damage the photonic structure during cleavage[157]. The dense outer SiO_2 layer was removed prior to reaction by placing a small amount of nail polish (Sally Hansen, Double Duty) on each end of the fiber to prevent liquid infiltration into the hollow core, and then immersing the fibers into hydrofluoric acid (30% w/w) for 120 minutes. Following removal of most of the dense silica cladding, the remaining fiber was washed with acetone to remove the nail polish and then heated at 200^{o}C for one hour to remove any residual acetone. Lengths (3-5 cm) of the fibers were then placed in an iron boat (approximately 2 cm x 6 cm, McMaster-Carr, 98%), completely immersed in approximately 5 mm deep Mg2Si powder bed (Alfa-Aesar, 99.5%), and sealed in a welded iron tube in the glove-box (<0.01 ppm O_2). The tube was heated at 5^{o}C/minute to 650^{o}C-850^{o}C for periods of 4-24 hours. After reaction and cooling, the tubes were removed from the furnace and opened, and the reacted fiber was carefully removed from the powder bed. The Si-phase of the reacted fibers was etched via exposure to a KOH:H_2O:IPA (1:2:0.005 w/w) solution, which was carried out in a foil-covered stainless steel tray at 70^{o}C with constant stirring for four hours. The resulting MgO fibers were immersed in aqueous hydrofluoric acid (40% w/w) for various times at room temperature. In order to observe cross-sections via SEM, the fiber was cleaved at least 1 cm away from the exposed end and mounted onto an SEM stub. All XRD analysis was

conducted by grinding several lengths of the fiber using a mortar and pestle into a powder, and using a standard powder diffraction sample holder in a Panalytical Alpha-1 diffractometer.

3.5 *Results*

A cross section of the HC-PCF after removal of the polyacrylate is shown in Figure 59a. At this stage, the fiber still contains the dense silica cladding which serves only to mechanically protect the inner photonic structure from scratches or damage and has no function with respect to waveguiding. This dense outer layer impeded the reactive conversion. Figure 59b shows a fiber cross-section after removal of the dense silica cladding and ready for conversion.

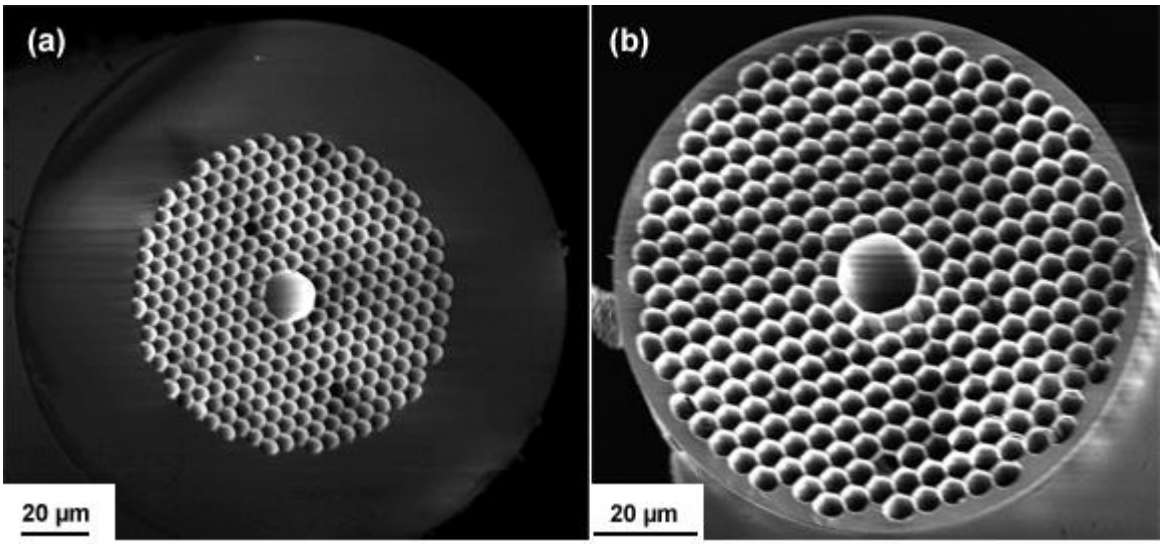

Figure 59: (a) As-purchased HC-PCF (HC2000, Thorlabs) and (b) Similar fiber after removal of most of the thick outer SiO_2 layer in HF.

The one-step shape-preserving conversion of SiO_2 directly into MgO, in which the silicon atoms diffuse out of the structure as a liquid (reaction 4.1) while the MgO is formed, was evaluated first. Such a one-step conversion of SiO_2 into MgO has involved

temperatures ≥900°C for several hours. Attempts at carrying out this one-step conversion on the photonic crystal fibers resulted in severe bending and fracture of the fibers along their length, as well as significant deformation of the axial photonic structure, as shown in Figure 60. The strain point (at which viscosity $\eta=10^{14.5}$ poise) of fused silica is between 820°C-990°C depending on exact composition and dopants[158] (Thorlabs was contacted in order to determine the exact strain point of the HC-PCFs used; however, the information was unavailable). Stresses induced by the reaction at high temperatures near the strain point of the fiber were likely responsible for the bending of the fibers and deformation of the photonic structure.

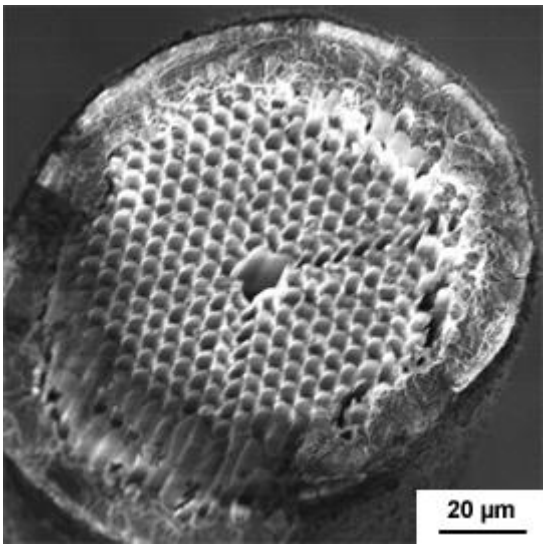

Figure 60: Axial cross-section displaying significant distortion of the photonic structure after exposure of the SiO_2 PCF to Mg(g) formed via vaporization of pure Mg metal at 900°C for 1 hour.

Lowering the reaction temperature precluded the use of the one-step conversion process by inhibiting formation of the silicon-rich liquid. However, a two-step conversion of SiO_2 into MgO has been demonstrated at lower temperatures via initial formation of a 2MgO/Si composite intermediate, followed by etching of the Si in a potassium hydroxide

solution[159] (reactions 4.3 and 4.4). MgO is both insoluble and inert in KOH solutions (reaction 4.5), while Si forms soluble silicates.

$$\mathbf{SiO_2(s)} + 2Mg(g) \rightarrow \mathbf{2MgO(s) + Si(s)} \quad (4.3)$$

$$\mathbf{2MgO/Si(s)} + 4KOH(a) \rightarrow [SiO_4]^{4-}(a) + 4K^{+}(a) + 2H_2(g) + \mathbf{2MgO(s)} \quad (4.4)$$

$$MgO + 2KOH \rightarrow K_2O + Mg(OH)_2 \qquad \triangle G(25^oC)=+175kJ \quad (4.5)$$

In order to conduct the reaction shown in equation 4.3, a 3-5 cm long section of photonic crystal fiber (after removal of the acrylate coating and the dense SiO_2 cladding) was immersed into a powder bed of Mg_2Si and sealed in an iron ampoule under argon atmosphere. Mg_2Si was used as the magnesium source for reasons discussed in chapter 3. The iron ampoule was heated at 10^oC/minute to temperatures between 650^oC – 850^oC. After reaction, the fiber changed from translucent to an opaque black. Most fibers retained their lengths. However a few times (<10% of the time) the fibers fractured during reaction. It is likely that such fibers had some pre-existing microcracks or surface flaws, perhaps caused by handling of the fibers with tweezers before reaction.

The integrity of the photonic structure after conversion to form the MgO/Si composite (reaction 4.3) was highly dependent on the reaction temperature (Figure 61). At a reaction temperature of 850^oC for 6 hours, significant damage (i.e., voids and cracks) to the photonic structure was generally observed. Lowering the temperature, even accounting for the longer reaction times required for complete conversion, resulted in enhanced shape preservation and reduced macro-defect formation. At a reaction temperature of 750^oC for 10 hours, the sidewalls of the photonic structure were generally maintained, although some distortion of the periodic photonic structure was observed.

Reducing the temperature further, to 700°C for 12 hours, generally resulted in high fidelity shape retention of the photonic crystal with no appreciable deformation (in some samples, the photonic structure was significantly damaged or fractured even after reaction at lower temperatures. However, in general, lowering the reaction temperature resulted in stronger shape preservation for most samples).

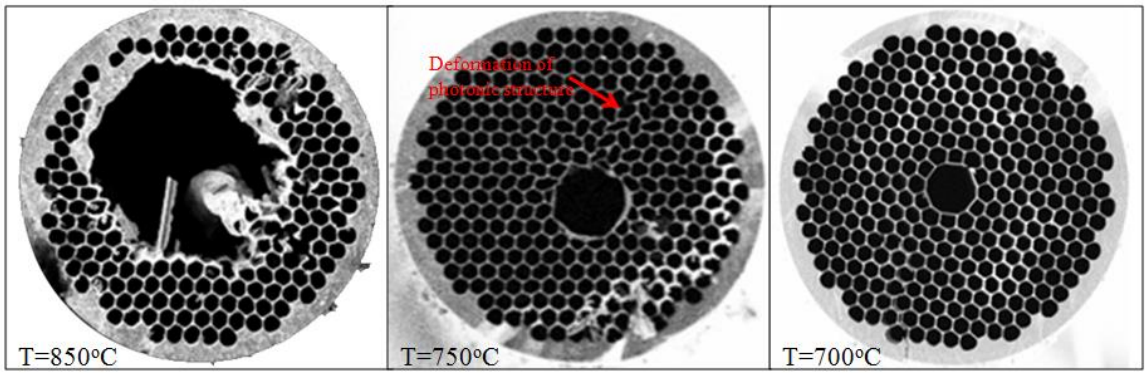

Figure 61: Cross-section of fibers at various reaction temperatures showing increased loss of photonic structure with increased reaction temperature (12 hour reaction time).

EDX mapping of silicon and magnesium after reaction at 700°C revealed that, for times insufficient for complete reaction, the Mg:Si ratio near the outside of the fiber was significantly higher than the corresponding Mg:Si ratio at the inner part of the fiber, close to the hollow core (Figure 62 shows EDX spectra for a reaction time of 6 hours). Various cross-sections cut from different locations along the length of the fiber showed no significant difference in chemical composition at different longitudinal positions. These observations suggest that the reaction occurred radially—starting at the outside of the fiber diameter and moving inwards towards the core— as opposed to longitudinally. Increasing the fiber length, therefore, was not expected to increase the time necessary for complete reaction (increasing the fiber radius would be expected to increase the required reaction times).

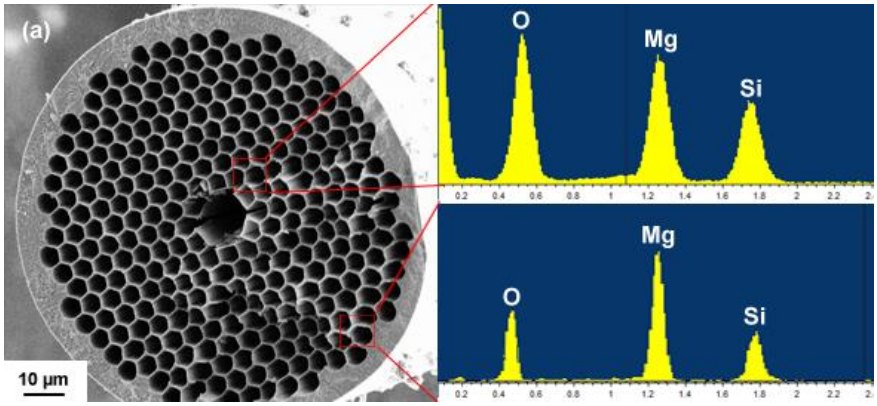

Figure 62: Cross section and EDX spectra for a 5 cm fiber partially reacted at 700ºC for 6 hours. The outer portion of the photonic structure of the fiber is fully reacted, while the inner sections are only partially reacted.

Completely reacted fibers showed a constant Mg:Si ratio across the axis of the fiber with peaks that corresponded approximately to atomic ratios of roughly 2:1 (Figure 63). The XRD pattern confirmed the presence of MgO and Si, with no observable amorphous hump which could be attributed to unreacted SiO_2.

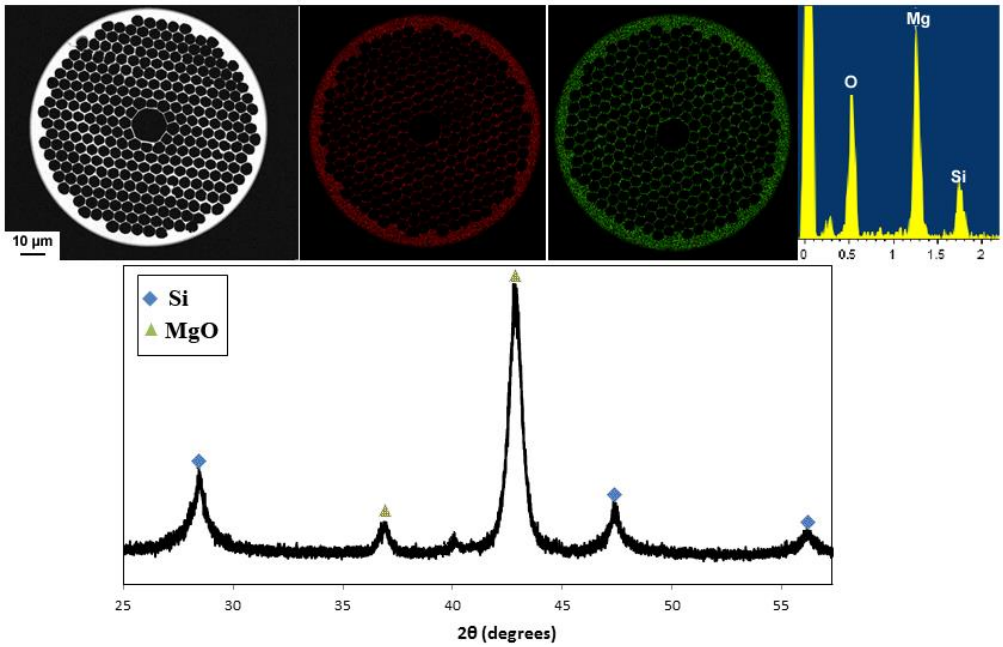

Figure 63: EDX mapping of Si (red) and Mg (green) across a sample reacted at 700°C for 12 hours shows a uniform ratio of Mg:Si across the sample, suggesting complete reaction. XRD (bottom) shows no amorphous hump associated with unreacted SiO_2.

Following complete conversion of the fibers into MgO/Si composite replicas, the silicon phase was selectively removed via exposure to a KOH:H_2O:IPA (1:2:0.005 w/w) solution[160]. During etching, bubbles of H_2 gas could be observed forming on the surface of the fiber. The addition of a small amount of isopropanol served to reduce the surface tension of the solution in order to allow for more facile detachment of the hydrogen gas bubbles, leading to a more controlled and uniform etch[161]. Etch times of 4 hours were sufficient to completely remove the silicon phase.

Cross-sectional SEM images confirmed that the photonic structure remained fully intact after dissolution of Si from the MgO/Si composite (Figure 64). Unfortunately, the fibers were very prone to breaking along their length (as discussed later in the *limitations* section of this chapter) during both the etch process itself and during physical removal of the fibers from the solution. EDX spectroscopy revealed peaks associated only with Mg

and O (as well as a C peak, which is the result of the vacuum oil used in the SEM contaminating the EDX measurements), and an absence of a peak associated with Si (which shows up at 1.8 keV). The XRD pattern confirmed the removal of the silicon phase to form a single-phase MgO replica.

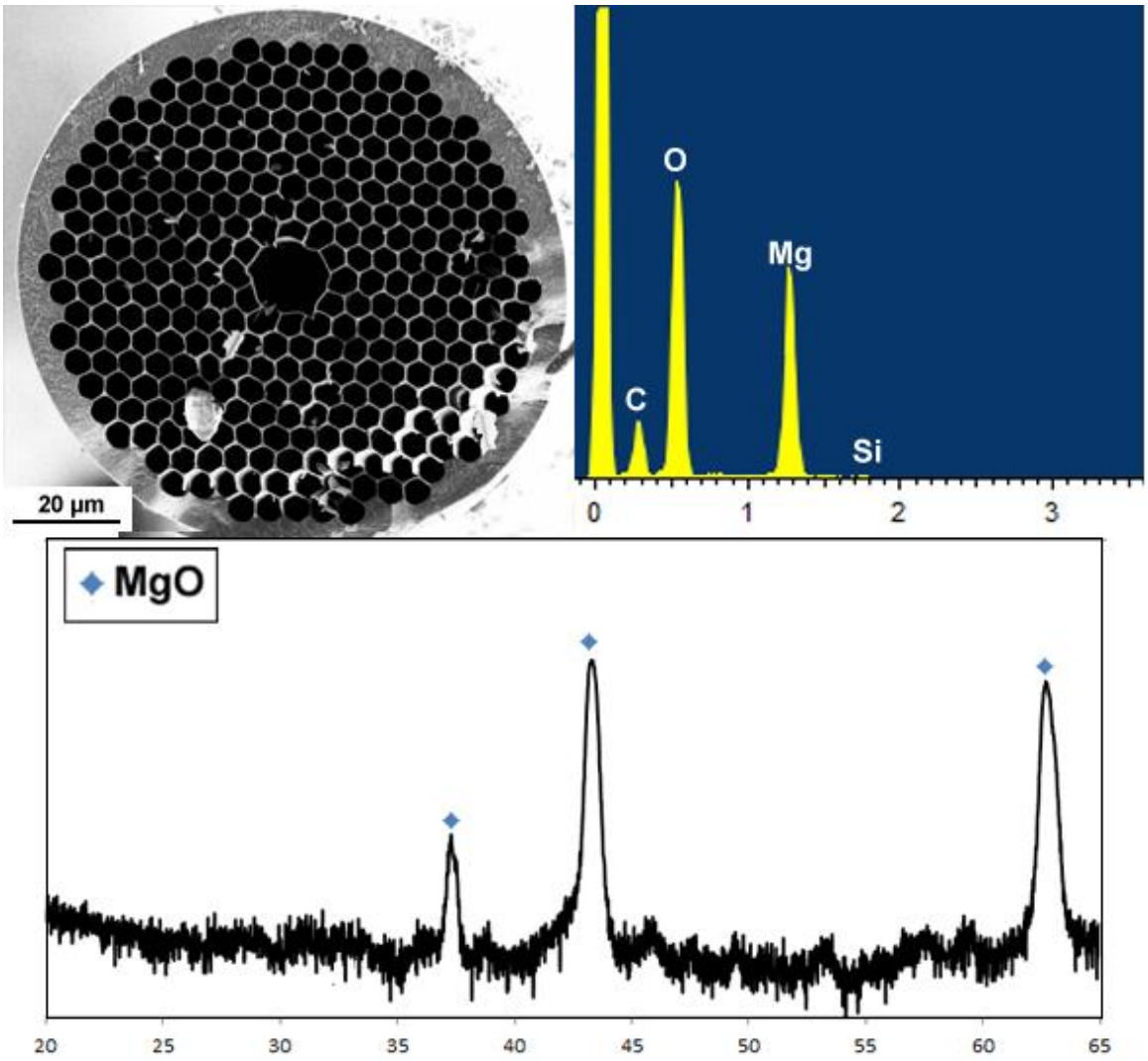

Figure 64: (a) Cross-section of fiber after removal of Si in a KOH solution as described in text for 4 hours; (b) EDX spectra confirming loss of Si and consistent with MgO; (c) XRD pattern confirming nanocrystalline MgO.

Exposure of MgO to solutions of hydrofluoric acid is known to result in the formation of MgF_2[162] at the solid-liquid interface. Since MgF_2 is highly insoluble in

water, bulk MgO is generally considered corrosion resistant in hydrofluric acid solutions, since the initial MgF_2 layer that forms can serve as a passivating layer to inhibit further reaction. One previous study estimated the corrosion rate of bulk MgO in 20 M aqueous HF at 90^{o}C to be extremely slow, with a rate of around 15 μm/year (1.7 nm/hour)[163]. Since the walls of the photonic crystal structure were approximately 500 nm thick and they were exposed to the liquid on two sides, penetration distances of about 250 nm on each side were necessary for complete conversion into MgF_2. Assuming a rate of 15 μm/year, long reaction times of around 147 hours (~6 days) should be required for complete reaction.

In practice, complete or nearly complete reaction to form MgF_2 was observed after much shorter reaction times. This is likely because, whereas the corrosion rate in the cited study utilized hot isostatically pressed MgO, which presumably was near-fully dense with large crystal sizes, the MgO fiber replicas utilized here were porous and nanocrystalline. Before dissolution of the Si-phase, the 2MgO/Si composite intermediate was comprised of 35 vol% silicon[154]. Removal of the Si-phase, therefore, is theoretically expected to result in a MgO replica comntaining approximately 35% porosity (since the etching was conducted out at 70^{o}C, no densification of the MgO was likely to occur). This porosity clearly would be expected to increase the solid-liquid interfacial area and therefore increase the reaction rate. In addition to the porosity, the polycrystalline nature off the MgO (49 nm mean grain size) would be expected to allow for enhanced reaction rates since grain boundaries represent both short-circuit pathways for diffusion as well as high energy interfaces[164]. In practice, immersing the fibers in concetrated hydrofluoric

acid (40% w/w, 22.6 M) at 70°C overnight (16 hours) was sufficient for nearly complete reaction.

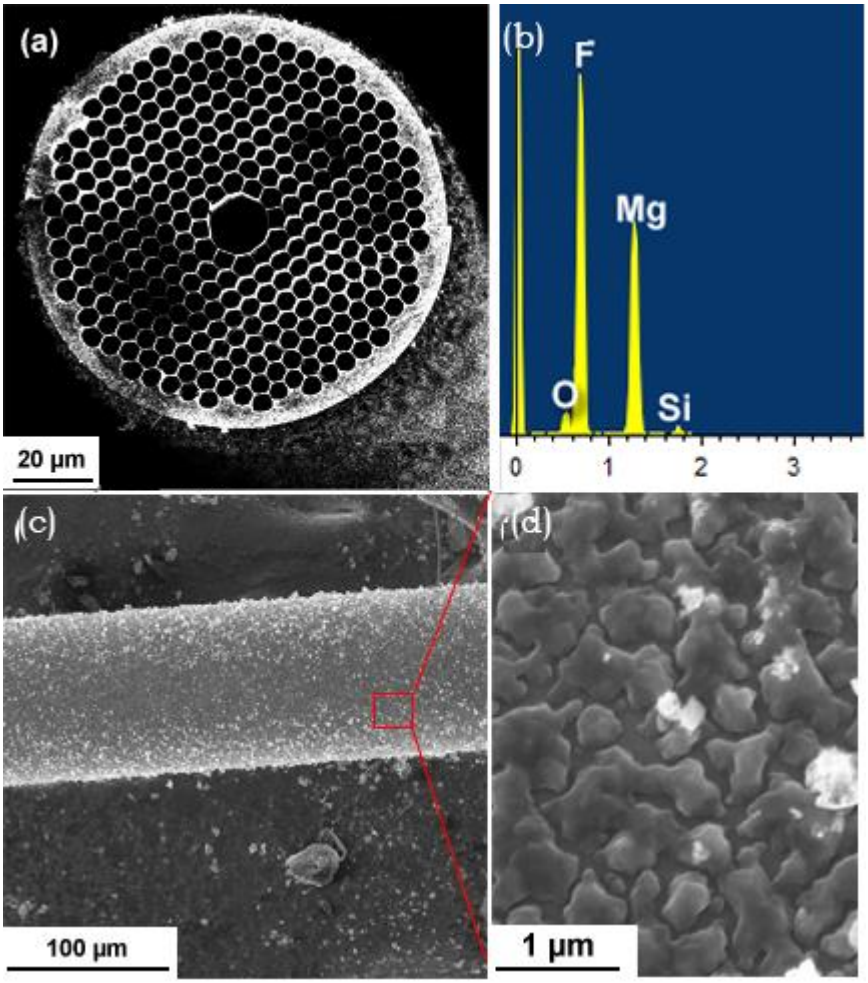

Figure 65: (a) Cross section of fiber after exposure to HF acid overnight; (b) EDX spectra of the fiber consistent with MgF_2 and trace levels of O and Si; (c) top-down view of the outside of the fiber, showing surface roughness; and (d) magnified view of the outer surface of the fiber.

An SEM image of a cross-section of fiber after reaction with HF to form MgF_2 is shown in Figure 65a. The photonic structure is clearly maintained with minimal distortion of the initial shape. As can be seen, the outer surface of the fiber develops significant roughness during the reaction. Figure 65c-d further reveals the roughness of the outer surface. As discussed in the previous chapter, the MgO replica before exposure

to hydrofluoric acid was approximately 35% porous. Porosity is undesirable for optical applications, since pores can act as scattering centers. Due to the large molar volume of MgF_2 (19.8 cc/mol) compared with MgO (11.3 cc/mol), the residual porosity was expected to be completely filled upon conversion of MgO to MgF_2.

A variety of chemical analyses of the fibers confirmed nearly complete reaction to MgF_2, with some trace MgO still present. The EDX spectrum (Figure 65b) shows large peaks associated with F and Mg, and indicates only trace amounts of residual Si and O. Both electron diffraction and X-ray diffraction (Figure 66) confirm the presence of MgF_2 as the major crystalline phase. The XRD pattern shows small peaks which are associated with trace, residual MgO, as well as some small, unidentified peaks.

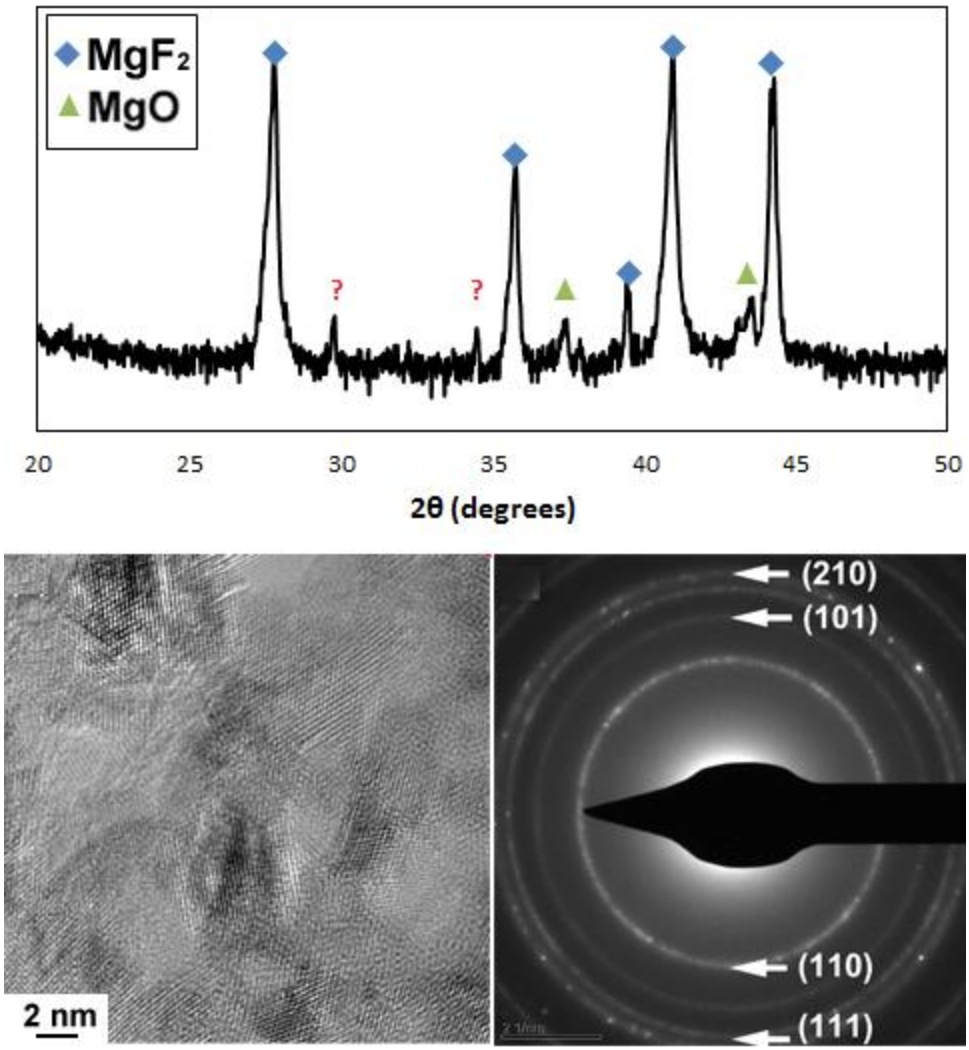

Figure 66: XRD pattern obtained from the converted fibers, confirming the conversion to MgF_2 (top); and TEM and electron diffraction of converted fiber (bottom).

A magnified view of the photonic structure is shown in Figure 67. Some microroughness can be observed on the surface of the MgF_2. It has been suggested that scattering due to surface roughness is one of the significant causes of attenuation in hollow core photonic crystal fibers, and that the surface roughness of the photonic structure determines the theoretical minimum possible attenuation value that can be achieved[165]. Roughness at the air/solid interface is therefore undesirable. It is possible

that systematic optimization of the reaction conditions could allow for conversion resulting in smoother surfaces.

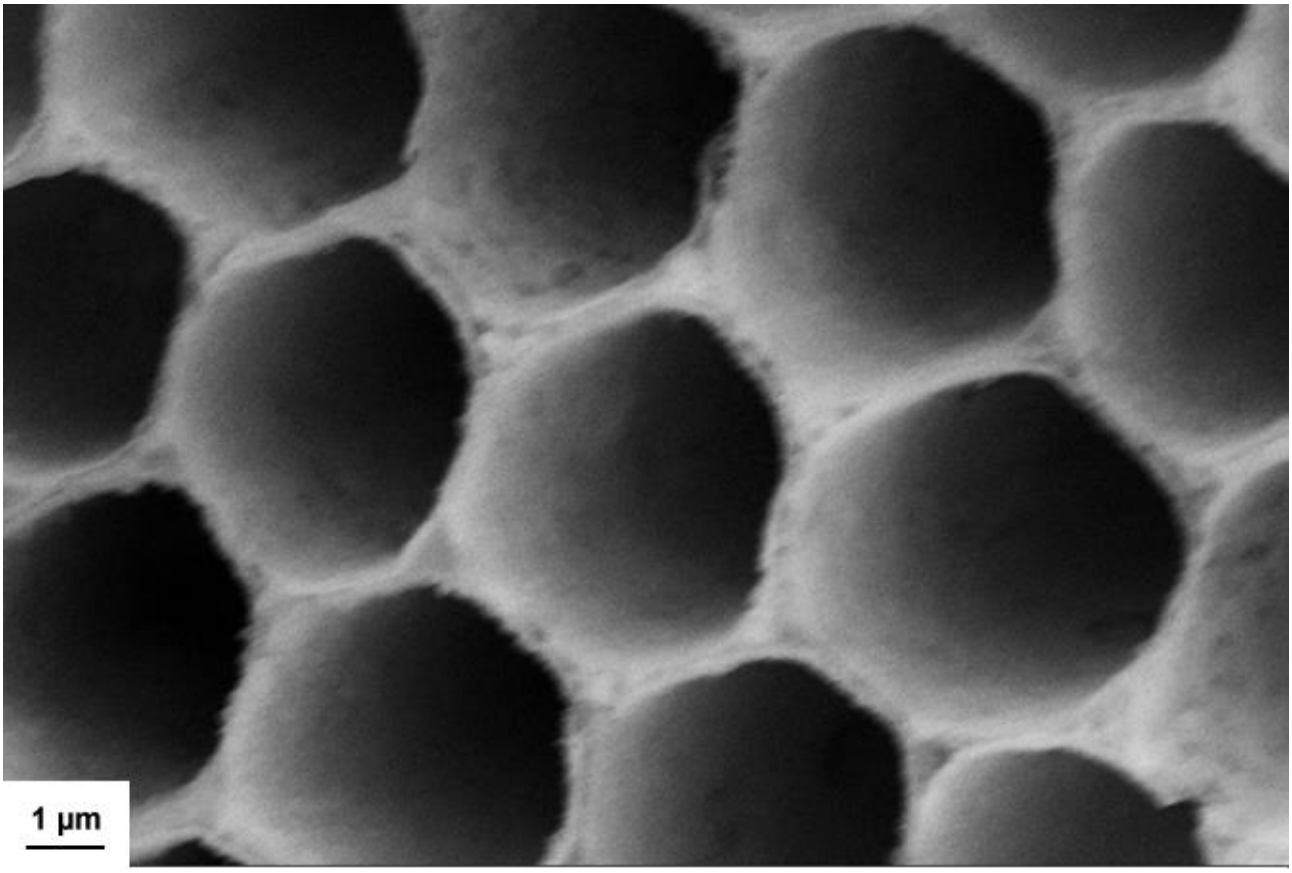

Figure 67: Magnified view of photonic structure showing some localized distortions of circular pores as well as surface texture after immersion in HF acid (40% w/w) for 16 hours at 70°C.

3.6 *Limitations and Future Directions*

The major limitation precluding both further academic investigation as well as practical application of MgF_2 photonic crystal fibers fabricated using the shape-preserving method developed in this study is the extreme mechanical fragility of the fibers. As purchased HC-PCFs are clad with a 120 µm thick layer of polyacrylate surrounding a 80 µm thick layer of dense silica. Both of these layers exist purely to allow for mechanical robustness and to protect the fragile inner photonic structure which

provides the actual functionality of the fiber. In order to carry out reactions on the fibers, the first step was to remove the polyacrylate as well as the dense silica. The resulting fiber consisted only of the hollow core, the photonic crystal, and a small (<5 μm) residual layer of dense SiO_2 (see Figure 59). The photonic crystal was made of a honeycomb structure comprised of >90% air with 500 nm ceramic walls providing the only structural integrity. Even **before** any further reactions, after removal of the outer protecting layers the fibers become very mechanically fragile. Routine handling with tweezers could easily cause fracture of the fiber, and extreme care was necessary. In order to avoid direct contact of the fiber with tweezers, sections of fiber were generally placed onto a piece of metal foil and the foil was moved.

Breakage during routine handling could be avoided with sufficient care. A few times (<10% of the time), fibers broke during the initial gas/solid reaction to form the 2MgO/Si intermediate. It is likely that these fibers already had some microcracks or surface flaws (perhaps from prior handling) which made them more susceptible to fracture during the reaction. However, the large majority of the time, the initial reaction was straightforward and MgO/Si composite fibers of relatively long lengths (5-10 cm, longer fibers were not tried) could be obtained.

The main source of cracking, which was unavoidable, occurred during etching of the Si-phase in the potassium hydroxide solution. There are likely two reasons for this. First, removal of the Si resulted in an MgO replica which was 35% porous, and was therefore even more fragile and prone to breaking than the initial fiber. Second, the etching step required that the solution be stirred in order to remove hydrogen gas bubbles from the surface and to dissolve the K_2SiO_3 product to allow for further reaction. The

stirring was catastrophic for the fibers. Immersion of fibers into the stirred solution always resulted in fracture of the initial fiber into several pieces of smaller lengths. These smaller pieces could be retrieved from the solution, cleaved to obtain a cross sectional SEM image and utilized for further reaction into MgF_2. However, the sections were far too short for incorporation into an actual optical system even for academic purposes, much less for potential practical use. Various methods were attempted in order to mitigate fracture of the fibers. For example, samples were attached to a piece of stainless steel foil via a small amount of epoxy at each end in order to prevent free movement of the fiber in the solution. However, in all cases the surface tension and agitation of the liquid resulted in breakage of the fragile fibers.

If this method is to be explored further, it is necessary to utilize an alternative method for silicon etching from the MgO/Si intermediate. Fortunately, the MEMS and semiconductor industries have developed a wide variety of "dry" etching processes for silicon. In a dry etching process, the sample is either bombarded with ions or exposed to a reactive vapor[166]. Utilization of a dry silicon etch could be employed to overcome the difficulties associated with prolonged immersion of the fragile fibers into a stirred solution. Similarly, instead of relying on immersion into hydrofluoric acid, the conversion of MgO into MgF_2 can also be accomplished via a gas/solid (or "dry") process. The conversion of MgO into MgF_2 has been observed upon exposure of MgO to various fluoride containing gasses (i.e., CCl_2F_2 [167]). Combining a dry silicon etch with a gas-phase reaction to form MgF_2 allows for the possibility of an all-dry process to convert SiO_2 into MgF_2 (reactions 4.5-4.7).

$$SiO_2(s) + Mg(g) \rightarrow 2MgO(s) + Si(s) \quad (4.5)$$

$$Si(s) + 2Cl_2(g) \rightarrow SiCl_4(g) \quad (4.6)$$

$$MgO(s) + CCl_2F_2(g) \rightarrow MgF_2(s) + {}^1/_2CO_2(g) + {}^1/_2CCl_4(g) \quad (4.7)$$

A "one-pot" conversion method can be envisioned in which the SiO_2 photonic crystal fiber is loaded into a reaction chamber in a furnace and exposed to a series of gasses at different conditions until it is completely reacted to form a MgF_2 replica, without the need for intermediate handling or any exposure to liquids. While such a one-pot scheme is admittedly speculative, the individual steps involved have all been demonstrated to some extent. In any case, the replacement of liquid/solid processes with gas/solid alternatives is likely necessary if the shape-preserving conversion of SiO_2 photonic crystal fibers into MgF_2 replicas is to be investigated further.

3.7 *Conclusion*

The conversion of SiO_2 hollow-core photonic crystal fibers into MgF_2 replicas was demonstrated. The resulting MgF_2 fibers maintained the complex two dimensional periodic structure of the initial starting SiO_2 fibers. The MgF_2 fibers may possess a greatly enhanced transparency range in the mid-IR as compared to the starting SiO_2 samples. Such a method could conceivably allow for fabrication of very high power, low loss hollow-core fibers which could operate in the near-IR and are expected to have significant sensing, military, and medical applications. Unfortunately, the fibers were extremely mechanically fragile and were prone to breaking, especially during prolonged immersion into stirred liquids. Replacement of the liquid/solid etching and reaction steps

with gas-based alternatives is likely necessary in order to obtain lengths of fiber suitable for further academic investigation or practical use.

3.8 *References*

[123] Hecht, Jeff. *City of light: the story of fiber optics*. Oxford University Press, 2004.

[124] Goff, David R., and James G. Stewart. *Fiber optic reference guide: a practical guide to the technology*. Ed. Kimberly S. Hansen. Boston: Focal Press, 1999.

[125] Russell, Philip. "Photonic crystal fibers: a historical account." *IEEE LEOS Newsletter* 21.10 (2007): 11-15.

[126] Ohashi, Masaharu, Kazuyuki Shiraki, and Katsusuke Tajima. "Optical loss property of silica-based single-mode fibers." *Lightwave Technology, Journal of* 10.5 (1992): 539-543.

[127] Birks, Timothy A., et al. "Photonic crystal fibres: An endless variety." *IEICE transactions on electronics* 84.5 (2001): 585-592.

Roberts, P., et al. "Ultimate low loss of hollow-core photonic crystal fibres." *Optics Express* 13.1 (2005): 236-244.

[128] Nktphotonics.com, (2014). *Hollow core photonic crystal fibers | NKT Photonics*. [online] Available at: http://www.nktphotonics.com/hollowcorefibers [Accessed 19 Feb. 2014].

[129] Wadsworth, William, Jonathan Knight, and Tim Birks. "State-of-the-Art Photonic Crystal Fiber." *Optics and Photonics News* 23.3 (2012): 24-31.

[130] Ramsay, Richard. "Photonic Crystal fiber characteristics benefit numerous applications." *SPIE Newsroom* (2008).

Bjarklev, Anders, Jes Broeng, and Araceli Sanchez Bjarklev. *Fabrication of Photonic Crystal Fibres*. Springer US, 2003.

[131] Benabid, Fetah. "Hollow-core photonic bandgap fibre: new light guidance for new science and technology." *Philosophical Transactions of the Royal Society A: Mathematical, Physical and Engineering Sciences* 364.1849 (2006): 3439-3462.

[132] Couny, Francois, Fetah Benabid, and P. S. Light. "Subwatt Threshold cw Raman Fiber-Gas Laser Based on H_ {2}-Filled Hollow-Core Photonic Crystal Fiber." *Physical ReviewLletters* 99.14 (2007): 143903.

[133] Benabid, Fetah, et al. "Stimulated Raman scattering in hydrogen-filled hollow-core photonic crystal fiber." *Science* 298.5592 (2002): 399-402.

[134] Ritari, Tuomo, et al. "Gas sensing using air-guiding photonic bandgap fibers." *Conference on Lasers and Electro-Optics*. Optical Society of America, 2004.

[135] Benabid, Fetah, J. Knight, and P. Russell. "Particle levitation and guidance in hollow-core photonic crystal fiber." *Optics Express* 10.21 (2002): 1195-1203.

[136] Light, P. S., et al. "Electromagnetically induced transparency in Rb-filled coated hollow-core photonic crystal fiber." *Optics Letters* 32.10 (2007): 1323-1325.

[137] Husakou, A. V., and J. Herrmann. "Supercontinuµm generation of higher-order solitons by fission in photonic crystal fibers." *Physical Review Letters* 87.20 (2001): 203901.

[138] Jones, A. M., et al. "Characterization of mid-infrared emissions from C_2H_2, CO, CO_2, and HCN-filled hollow fiber lasers." *Proc. SPIE8237 Y* 82373 (2012): 82373Y-10.

Tittel, Frank K., Dirk Richter, and Alan Fried. "Mid-infrared laser applications in spectroscopy." *Solid-State Mid-Infrared Laser Sources*. Springer Berlin Heidelberg, 2003. 458-529.

[139] Teikemeier, Gabriele, and David J. Goldberg. "Skin resurfacing with the erbium: YAG laser." *Dermatologic surgery* 23.8 (1997): 685-687.

Bornstein, E. "Proper use of Er: YAG lasers and contact sapphire tips when cutting teeth and bone: scientific principles and clinical application." *Dentistry today* 23.8 (2004): 84-86.

Lewandrowski, Kai-Uwe, et al. "Use of the Er: YAG laser for improved plating in maxillofacial surgery: comparison of bone healing in laser and drill osteotomies." *Lasers in surgery and medicine* 19.1 (1996): 40-45.

[140] Aggarwal, I. D., et al. *IR Photonic Bandgap Fibers for Missile Defense*. Naval Research Lab Washington DC Optical Sciences Div, 2007.

[141] Wooten, Frederick. *Optical properties of solids*. Vol. 111. New York: Academic press, 1972.

Harris, Daniel C. *Materials for infrared windows and domes: properties and performance*. SPIE press, 1999.

[142] Eggleton, Benjamin J., Barry Luther-Davies, and Kathleen Richardson. "Chalcogenide photonics." *Nature Photonics* 5.3 (2011): 141-148.

[143] I.G.I. Consulting. *Study of the Market for IR Fibers*. Information Gatekeepers Inc.

[144] SANGHERA, Jasbinder, et al. "Hollow core photonic band gap infrared fivers." WIPO Patent No. 2005017569. 25 Feb. 2005.

[145] Anscombe, Nadya. "The promise of chalcogenides." *Nature Photonics* 5.8 (2011): 474-474.

[146] Pottage, J., et al. "Robust photonic band gaps for hollow core guidance in PCF made from high index glass." *Optics Express* 11.22 (2003): 2854-2861.

[147] German, Randall M., Gary L. Messing, and Robert G. Cornwall, eds. *Sintering technology*. CRC Press, 1996.

[148] Lucas, Jacques, Frederic Smektala, and Jean Luc Adam. "Fluorine in optics." *Journal of fluorine chemistry* 114.2 (2002): 113-118.

[149]Masuoka, Toshio, and Takanori Oshio. "Lyman-alpha detector with MgF_2 window." *Review of Scientific Instruments* 45.8 (1974): 1012-1014.

Ding, Luying, and Paul Marshall. "Kinetic studies of the reactions of atomic chlorine and bromine with silane." *The Journal of Physical Chemistry* 96.5 (1992): 2197-2201.

Inoue, Kohji, et al. "Low Temperature Growth of SiO_2 Thin Film by Double-Excitation Photo-CVD." *Jpn. J. Appl. Phys* 26 (1987): 805-811.

[150] Jacob, Mohan V., et al. "Cryogenic complex anisotropic permittivity of magnesium fluoride." *Materials Science and Engineering: A* 427.1 (2006): 175-180.

[151] Fisher, G. B., et al. "A Standard for Ultraviolet Radiation." *Applied optics* 12.4 (1973): 799-804.

Uchida, Saburo, et al. "Plasma damage mechanisms for low- k porous SiOCH films due to radiation, radicals, and ions in the plasma etching process." *Journal of Applied Physics* 103.7 (2008): 073303-073303.

El-Habachi, Ahmed, and Karl H. Schoenbach. "Emission of excimer radiation from direct current, high-pressure hollow cathode discharges." *Applied physics letters* 72.1 (1998): 22-24.

Washida, N., et al. "Emission spectra of SiH (A Δ→ X Π) and SiCl (A B→ X A) in the VUV photolyses of silane and chlorinated silanes." *The Journal of Chemical Physics* 83 (1985): 2769.

[152] Mikeska, Kurt R., Stephen J. Bennison, and Steven L. Grise. "Corrosion of ceramics in aqueous hydrofluoric acid." *Journal of the American Ceramic Society* 83.5 (2000): 1160-1164.

[153] Pickering, W. F. "The mobility of soluble fluoride in soils." *Environmental Pollution Series B, Chemical and Physical* 9.4 (1985): 281-308.

[154] Powder Diffraction File Card No. ICDD 41-1443 for MgF_2, 27–1402 for Si, Card No. 45–946 for MgO (International Center on Diffraction Data, Newtown Square, Pennsylvania); www.icdd.com

[155] Wen, Tzu-Chien, and *Dinesh K. Shetty. "Birefringence and grain-size effects on optical transmittance of polycrystalline magnesium fluoride." SPIE Defense, Security, and Sensing. International* Society for Optics and Photonics, 2009.

[156] Xie, Z., et al. "Broad spectral photonic crystal fiber surface enhanced Raman scattering probe." *Applied Physics B* 95.4 (2009): 751-755.

Khetani, Altaf, et al. "Method for using a photonic crystal fiber as a Raman biosensor." U.S. Patent No. 7,738,097. 15 Jun. 2010.

Yang, Xuan, et al. "High-sensitivity molecular sensing using hollow-core photonic crystal fiber and surface-enhanced Raman scattering." *JOSA A* 27.5 (2010): 977-984.

Joly, N. Y., et al. "Bright spatially coherent wavelength-tunable deep-UV laser source using an Ar-filled photonic crystal fiber." *Physical review letters* 106.20 (2011): 203901.

Naji, Majid, et al. "A novel method of using hollow-core photonic crystal fiber as a Raman biosensor." *Biomedical Optics (BiOS) 2008*. International Society for Optics and Photonics, 2008.

US, Dinish, et al. "Highly sensitive SERS detection of cancer proteins in low sample volume using hollow core photonic crystal fiber." *Biosensors and Bioelectronics* 33.1 (2012): 293-298.

[157] http://www.thorlabs.com/images/TabImages/Application_note_-_stripping_cleaving_and_coupling.pdf

[158] Chen, Andrea, and Randy Lo. *Semiconductor Packaging: Materials Interaction and Reliability*. CRC Press, 2012.

[159] Allan, Shawn Michael. "Reactive replacement and addition of cations in bioclastic silica and calcite." (2005).

[160] Potassium Hydroxide Silicon Etch; Tufts University, http://engineering.tufts.edu/microfab/index_files/SOP/KOHEtch_SOP.pdf

[161] Zubel, Irena, and Małgorzata Kramkowska. "The effect of alcohol additives on etching characteristics in KOH solutions." *Sensors and Actuators A: Physical* 101.3 (2002): 255-261.

[162] Cho, Dong Hyun, et al. "Behavior of chromium oxide on MgO or MgF_2." *The Journal of Physical Chemistry A* 102.41 (1998): 7913-7918.

Visher, Paul S. "Process for the purification of mag." U.S. Patent No. 2,441,668. 18 May 1948.

Cho, Dong Hyun, Young Gul Kim, and Jong Shik Chung. "Catalytic fluorination of 1, 1, 1-trifluoro-2-chloroethane (HCFC-133a) over chromium catalysts." *Catalysis letters* 53.3-4 (1998): 199-203.

da Conceicao, T. F., et al. "Surface modification of magnesium alloy AZ31 by hydrofluoric acid treatment and its effect on the corrosion behaviour." *Thin Solid Films* 518.18 (2010): 5209-5218.

Iwasaki, K., H. Fukutani, and S. Nakano. "Polymerization of vinyl ethers with magnesium compounds. I. Catalytic reactivity of magnesium halides." *Journal of Polymer Science Part A: General Papers* 1.6 (1963): 1937-1946.

[163] Mikeska, Kurt R., Stephen J. Bennison, and Steven L. Grise. "Corrosion of ceramics in aqueous hydrofluoric acid." *Journal of the American Ceramic Society* 83.5 (2000): 1160-1164.

[164] Schacht, M., N. Boukis, and E. Dinjus. "Corrosion of alumina ceramics in acidic aqueous solutions at high temperatures and pressures." *Journal of materials science* 35.24 (2000): 6251-6258.

Schacht, Michael, et al. "Corrosion of zirconia ceramics in acidic solutions at high pressures and temperatures." *Journal of the European Ceramic Society* 18.16 (1998): 2373-2376.

[165] Roberts, P., et al. "Ultimate low loss of hollow-core photonic crystal fibres." *Optics Express* 13.1 (2005): 236-244.

Birks, T. A., et al. "The fundamental limits to the attenuation of hollow-core photonic crystal fibres." *Transparent Optical Networks, 2005, Proceedings of 2005 7th International Conference*. Vol. 1. IEEE, 2005.

[166] Marc J. Madou. *Fundamentals of Microfabrication and Nanotechnology: Manufacturing techniques for microfabrication and nanotechnology*. Vol. 2. CRC Press, 2011.

Saito, Yoji, Osamu Yamaoka, and Akira Yoshida. "Plasmaless etching of silicon using chlorine trifluoride." *Journal of Vacuum Science & Technology B: Microelectronics and Nanometer Structures* 9.5 (1991): 2503-2506.

[167] Tamai, Tsukasa, Koji Inazu, and Ken-ichi Aika. "Dichlorodifluoromethane decomposition to CO_2 with simultaneous halogen fixation by calcium oxide based materials." *Environmental science & technology* 40.3 (2006): 823-829.

Chapter 4: Kinetic Study of Magnesium Silicide Growth

4.1 Summary

The conversion reaction of silicon into magnesium silicide is utilized throughout the research described in this thesis. After an extensive review of the literature, a detailed kinetic study elucidating the growth mechanism, temperature-dependent growth rates, and activation energy of Mg_2Si growth was not found. The motivation behind this chapter is two-fold: first, to investigate the kinetics of the conversion of silicon into magnesium silicide at various temperatures; and second, to evaluate the use of high temperature X-ray diffraction (HTXRD) as an in-situ method for quantitative study of thin-film growth kinetics.

4.2 The Silicidation Reaction

Binary compounds of the formula M_xSi_y (where M is a metal atom), also known as metal silicides, have received interest due to their refractory, thermal, and electronic properties. Molybdenum silicides can be used as protective coatings to prevent high temperature oxidation[168]. Various transition metal silicides, including WSi_2, $TiSi_2$, and $CoSi_2$ are utilized in microelectronics as ohmic contacts, electrodes, interconnects, and diffusion barriers[169]. Fabrication of metal silicides can be accomplished in several ways, including physical vapor deposition of a metal film (via sputtering, evaporation etc.) onto a silicon wafer followed by heat treatment, codeposition of metal and silicon, or decomposition of silane gas over a metallic surface. By far the most well studied fabrication method, especially for the formation of thin films or nanostructures, is the deposition of a metal film onto a silicon wafer followed by annealing. The reaction

occurs between the solid metal and the silicon wafer, and so is referred to as a solid/solid silicidation reaction (as opposed to a gas/solid reaction). The relevant reaction for formation of magnesium silicide is shown in reaction 5.1.

$$2Mg(s) + Si(s) \rightarrow Mg_2Si(s) \qquad \Delta G^o_{rxn}(773K) = -71kJ \quad (5.1)$$

The growth kinetics of a large number of silicide thin films have been investigated. Nearly all kinetic studies have focused on the growth of transition metal silicides, mainly due to their use in microelectronics. Alkaline earth metal silicides (e.g. Mg_2Si) have only recently attracted attention due to their potential use in thermoelectric devices. Comprehensive kinetic studies into the formation of alkaline earth metal silicides are still lacking. From previous studies into transition metal silicides, three broad categories of growth kinetics have been observed: (1) solid-state diffusion controlled (either by the metal diffusing inward or silicon diffusing outward); (2) nucleation controlled; or (3) other interfacial chemical reaction controlled. Significant characteristics with each type of growth, and examples of each from the literature are shown in Table 7.

Table 7: Overview of rate limiting steps and growth characteristics of various silicides.

Rate limiting Step	Observed Growth	Examples
Solid-state diffusion	Parabolic growth of reacted zone w.r.t. time. Generally occurs at low temperatures ($0.4T_m$). Most common silicide growth mechanism.	Ni_2Si, Pd_2Si, Co_2Si, Pt_2Si, PtSi, MnSi, FeSi[194]
Nucleation of silicide phase	No reaction below a threshold temperature, extremely fast reaction above threshold temperature. Common for silicides with small ΔG^f values.	$IrSi_3$, PdSi, $NiSi_2$, $ZrSi_2$[170]
Chemical reaction	Linear growth of reacted zone w.r.t. time. Uncommon, not well studied.	VSi_2[175]

Solid-state diffusion control is the most common and occurs when mass transport of one of the species through a thickening reaction product zone is rate-limiting. The

diffusing species can be either the silicon (as in the case of $TiSi_2$[171]) or the non-silicon element (as in the case of Ni_2Si[172]). For a magnesium-silicon reaction couple, previous experiments using inert markers have determined that inward diffusion of magnesium dominates[188,196] and that Mg_2Si growth occurs predominantly at the Mg_2Si/Si interface. A schematic, assuming diffusion limited reaction kinetics, showing the magnesium activity before growth (t=0) and after some growth has occurred (t>0) is shown in Figure 68.

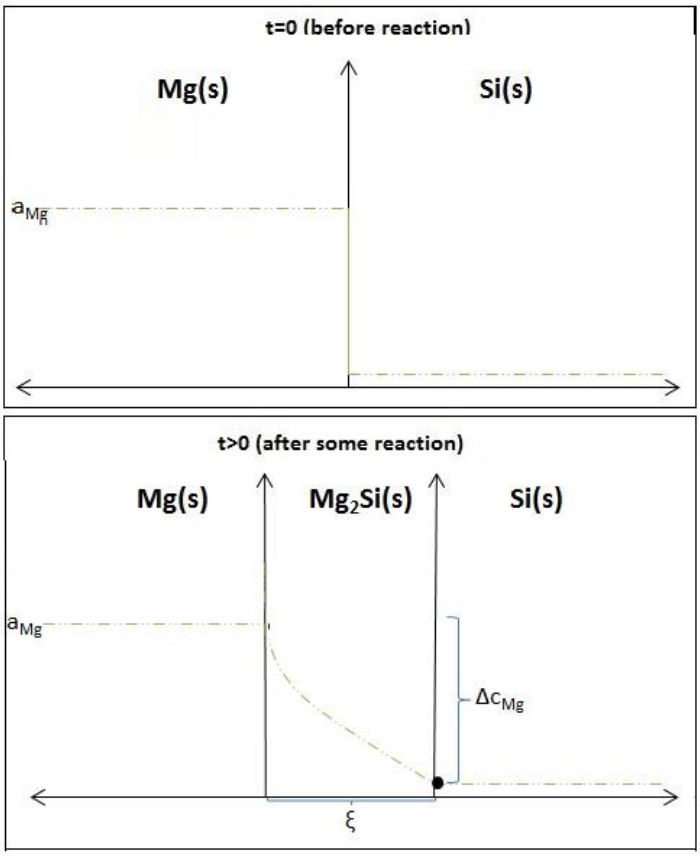

Figure 68: Profile of magnesium activity before reaction (top) and after some reaction has occurred (bottom).

As can be seen from Figure 68, after some time a reacted zone forms with thickness ξ. Assuming the reacted layer is dense and crack-free, further growth requires diffusion of magnesium from the metal, across the reacted zone, and to the silicide/silicon

interface. The growth of the reacted zone with time, dξ/dt, is proportional to the flux of magnesium atoms across the reacted zone (equation 5.2), which is given by Fick's first law (equation 5.3). Since magnesium has nearly no solubility in silicon[173], the magnesium activity at each interface (the metal/silicide interface and the silicide/silicon interface) is considered constant with time. The dC_{Mg} term in equation 5.3 is therefore also constant (and denoted Δc_{Mg}) to form equation 5.4. Combination with equation 5.2 followed by integration and combination of all constants into k_p yields a parabolic relationship between reacted zone thickness and with time, as shown in equation 5.7. Note that there is factor of ½ on the left hand side of the equation which results from integration of equation 5.6 to form equation 5.7. In this case, the factor has been included in the constant k_p, and the k_p values reported herein include this factor.

$$\frac{d\xi}{dt} = constant * j_{Mg} \qquad \text{Eq 5.2}$$

$$j_{Mg} = D_{Mg} * \frac{dc_{Mg}}{dx} \qquad \text{Eq. 5.3}$$

$$j_{Mg} = \frac{D_{Mg} * \Delta c_{Mg}}{\xi} \qquad \text{Eq. 5.4}$$

$$\frac{d\xi}{dt} = constant * \frac{D_{Mg} * \Delta c_{Mg}}{\xi} = \frac{k}{\xi} \qquad \text{Eq. 5.5}$$

$$\xi d\xi = kdt \qquad \text{Eq. 5.6}$$

$$\xi^2 = k_p t \qquad \text{Eq. 5.7}$$

Note that there is a factor of 2, not shown, which arises upon integration of 5.6 and which has been included into the parabolic rate constant k_p. In reviewing the available published literature on silicide growth, it was found that equation 5.7, in which the

integration constant is incorporated into k_p, is the most common manner of representing the parabolic rate constant (this is not the case for oxidation studies, in which the integration factor is generally separated from the rate constant). When comparing rate constants from various sources it is important to ensure that similar definitions of k_p are utilized.

For a growth mechanism under solid-state lattice diffusion control, the thickness of the reacted zone plotted against square root of time will show a linear relationship with a slope equal to the square root of the parabolic growth rate constant, k_p. Since k_p is a function of thermally activated diffusivity, it is further expected to vary with temperature according to the Arrhenius equation. Diffusion controlled reactions in silicides generally occur at low temperatures (as low as ~$0.4T_m$, where T_m is the melting point of the silicide) and have activation energies typically between 1-3 eV[194].

Although solid-state diffusion limited kinetics are the most common for silicide growth, a number of silicide films have been reported to grow via other mechanisms. Several silicides, most notably the rare earth metal silicides with formula $MSi_{1.7}$ (M= Er, Gd, Tb, Y), were found to exhibit growth limited by initial nucleation of the silicide phase[174]. In these cases, below a threshold temperature there was no observed reaction zone. Once a critical temperature was reached, islands of the silicide formed and rapidly grew in size to consume the entire deposited metal film. After initial nucleation, the reaction occurred so rapidly that it was difficult to determine growth rates with respect to time. Atomic mobility at the temperatures required to drive nucleation was high, so that diffusion no longer limited the overall growth. In addition to nucleation-controlled growth, some authors have reported observing a linear growth rate with time[175]. When a

linear growth rate was observed, it was assumed that a chemical reaction at the interface, which occurred at a constant rate regardless of the thickness of the reacted zone, limited the overall growth (an example of this is VSi_2)[175].

4.3 In-situ Observation via Grazing Angle, HT-XRD

In order to determine the kinetics of the conversion of silicon to magnesium silicide--including growth rates at various temperatures, determination of the rate limiting step, and activation energy-- it was necessary to measure the thickness of the Mg_2Si layer formed after various annealing times at several temperatures. In the large majority of previous studies into silicide growth, either Rutherford Backscattering Spectroscopy (RBS) or Auger Electron Spectroscopy (AES) was used to determine the reacted zone thickness after reaction at several times for a given temperature[176]. While these spectroscopic methods are capable of very precise depth and composition profiling, the use of such *ex-situ* measurements limits the number of data points which are generally obtained. As a result, most kinetic studies of silicide growth found in literature utilize five or less, and sometimes as few as two or three, data points per reaction temperature.

An *in-situ* technique, alternatively, could yield hundreds of data points for a single temperature with minimal time or cost associated with each additional point. One possible technique to monitor the silicidation reaction *in-situ* at various temperatures is high-temperature X-ray diffraction (HT-XRD). In HT-XRD, the material is held at elevated temperatures under flowing helium while XRD patterns are periodically collected. As the silicidation reaction occurs, the peaks corresponding to reactants (Mg in

this case) are expected to decrease while peaks associated with products (Mg_2Si in this case) are expected to increase.

For the growth of thin films, such as the formation of an Mg_2Si layer on a Si substrate, it may be desirable to utilize *grazing angle* X-ray diffraction. In a grazing angle XRD instrument, the angle of the incident beam is held constant, generally at a value of less than 5^o, and only the detector moves. The low incident angle results in a small penetration depth and therefore minimizes the contribution from the underlying substrate while maximizing the near-surface volume that is sampled. This is in contrast to the standard gonio (also known as a Θ-2Θ) geometry, in which the angle of the incident beam is varied during a scan. As the incident angle increases, the X-ray beam penetrates deeper into the material and the sampled volume of the underlying substrate increases while the fraction of the sampled volume near the surface decreases (Figure 69). Grazing angle XRD is therefore preferred when primarily surface contributions are of interest, as is the case for thin films.

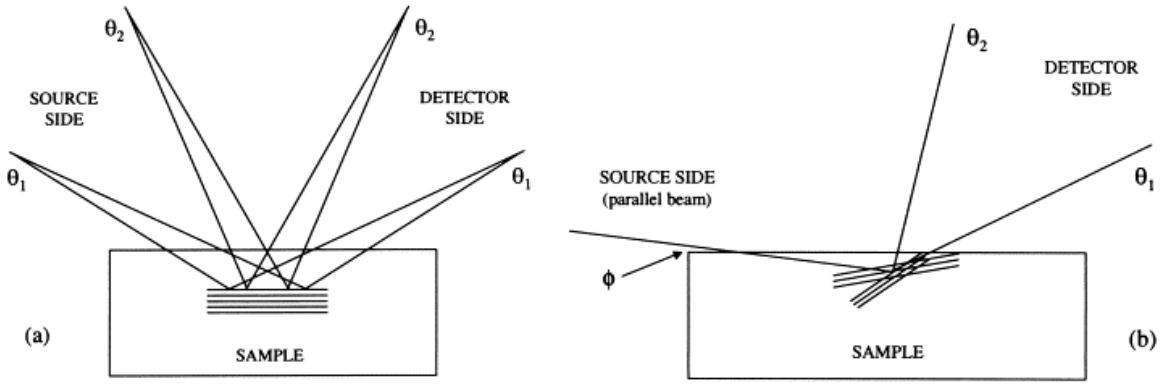

Figure 69[177]: (Left) In a normal gonio scan, both the angle of the incident beam and the angle of the detector move. At high angles, the beam penetrates deeper into the sample. (Right) In grazing angle geometry, the incident beam is held at a low angle, so penetration depth is minimized and surface contributions are larger.

While various HT-XRD based kinetic studies have been previously published, after extensive literature searches no publications utilizing *grazing angle* HT-XRD to quantitatively determine growth kinetics have been found. In this chapter, an experimental setup is designed to monitor the solid/solid silicidation reaction *in-situ* via grazing angle HT-XRD and equations are derived to relate obtained X-ray diffraction patterns to growth rates. The temperature-dependent growth rates, rate-limiting step, and activation energy for thin film growth of Mg_2Si are determined.

4.4 Experimental Setup

Polished single crystal silicon wafers (UniversityWafer, Massachusetts, USA; surface roughness <0.5 nm) of orientation (100) and (111) were placed into a CHA Industries Mark 40 e-beam assisted evaporation system. The chamber was pumped down to a pressure below 1E-6 Torr, and an automated program was executed to coat 10,000 Å of magnesium, followed by approximately 150Å of titanium, without breaking vacuum

between the coatings. The thickness of the coatings was monitored *in-situ* by a quartz crystal resonator. Deposition rates of 5Å/second and 1 Å/second were used for magnesium and titanium, respectively. The quartz crystal resonator indicated a total deposition of 10,070Å of magnesium and 153Å of titanium. The coated wafers were then cut into smaller samples of approximately 2 cm x 2 cm and placed into a HTK-1200 furnace connected to a Panalytical X'pert PRO MPD diffractometer. The furnace was heated to the desired reaction temperature at 30°C per minute and X-ray diffraction scans were collected with the following parameters: constant 5° incident angle, 2Θ sweep of 33-42 degrees, soller slits of 0.4 radians for both incident and diffracted beams, anti-scatter slit and divergence slit of 1/4° and 1/8°, respectively. In a typical experiment, the samples were held at the desired temperature for a total of 10 hours and XRD patterns were collected at 10 minute intervals. HT-XRD experiments were carried out three times each for growth on both Si(100) and Si(111) wafers at a temperature range of 280-400°C.

4.5 Results

The X-ray diffraction pattern of a Mg-coated silicon wafer before reaction is shown in Figure 70. The coated magnesium shows a preferred orientation along the (002) plane. This preferred orientation, which was observed on both Si(100) and Si(111), is thought to minimize stress during the deposition process and has been reported numerous times in the published literature for both e-beam evaporation[178] and other deposition methods[179] of magnesium onto various substrates. SEM images of the as-coated wafers confirm that a uniform magnesium layer, with a thickness of approximately 1 μm was deposited, consistent with the value reported from the CHA-1 deposition instrument.

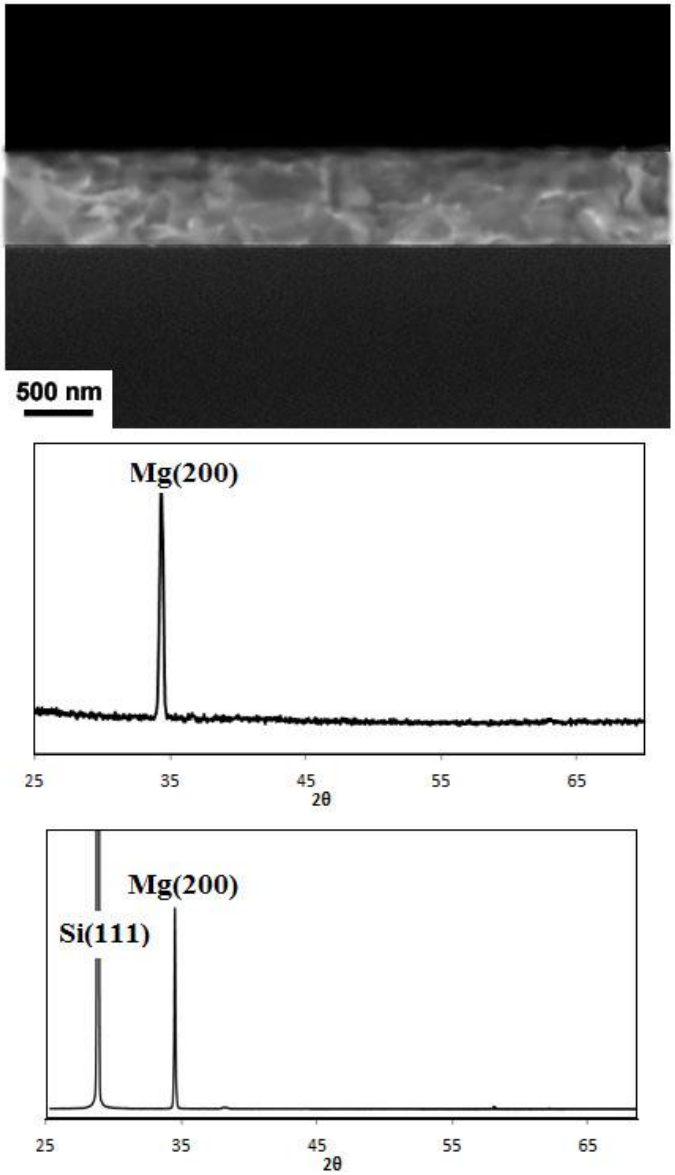

Figure 70: (a) SEM cross section of as-coated Si(100) wafer and (b) XRD pattern of as-coated Si(100) and (c) XRD pattern of as-coated Si(111) wafer.

The thickness of the coated wafers was evaluated by SEM at various areas selected randomly from the wafer.

Table 8 summarizes the measured magnesium coating thicknesses, determined by SEM, for the as-coated wafers.

Table 8: Thickness of Mg-coating at randomly selected areas of the wafer.

	Si(100)	Si(111)
Mg thickness (nm)	1041	1016
	1046	1037
	1006	985
	974	978
	990	1028
Average	1011.4	1008.8
St. Dev.	31	26

As noted in the experimental section, in addition to magnesium, each wafer was also coated with a very thin (~15 nm) capping layer of titanium. This capping layer served to protect the coated magnesium film from oxidation during both handling in air and during elevated temperature annealing. Although the annealing step was conducted under flowing helium, the oxygen partial pressure required to oxidize magnesium is extremely low ($pO_2=2E^{-98}$ atm at 300^oC)[180]. The trace oxygen content of high-purity gasses is more than sufficient to drive surface oxidation of magnesium, so a capping layer was necessary. Previous studies of Mg_2Si thin film formation have found that annealing without a capping layer under either high-vacuum or argon atmospheres leads to significant formation of MgO in addition to Mg_2Si[191,]. Titanium was chosen as the capping layer since it is one of the few metals that is inert with respect to magnesium (Figure 71). Only a very thin layer of titanium was used, below the threshold necessary for detection via XRD, in order to ensure that the XRD peaks associated with Ti ($2\Theta^{(101)}=40.1^o$)[181] did not overlap appreciably with the primary peak associated with Mg_2Si ($2\Theta^{(022)}=39.7^o$)[184].

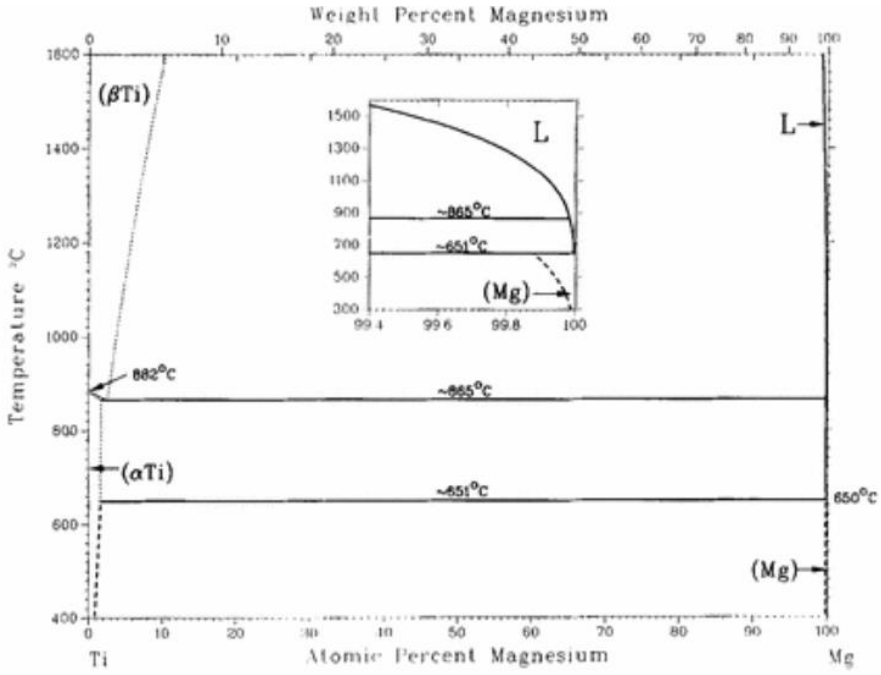

Figure 71: Phase diagram of the Ti-Mg system182.

In order to determine the appropriate parameters for HT-XRD analysis, a sample of the Mg-coated wafer was annealed in a conventional furnace under an argon-atmosphere at 500ºC for 12 hours in order to completely consume all magnesium and form Mg_2Si. Following the reaction, the sample was cooled to room temperature and an XRD pattern was collected from $2\Theta=20^{o}$-70^{o} (Figure 72). The XRD pattern confirmed the formation of polycrystalline Mg_2Si with no preferred orientation. No other reaction products, such as MgO, other Mg-Si compounds (i.e., the metastable Mg_5Si_6 compound[183]), or Ti-Si compounds, were detected. Using the known molar volumes of Mg (11.3 cm^{-3})[184] and Mg_2Si (39.5 cm^{-3})[184], as well as the stoichiometry of the silicidation reaction (2:1 molar ratio of Mg:Mg_2Si), it can be calculated that complete consumption of a 1 μm thick layer of magnesium should result in a 1.4 μm thick layer of Mg_2Si (this assumes that all volume expansion occurs via thickening, and that there is no

change in the lateral dimensions upon conversion). SEM images of the reacted sample revealed an Mg_2Si layer of thickness in very close agreement with the expected value.

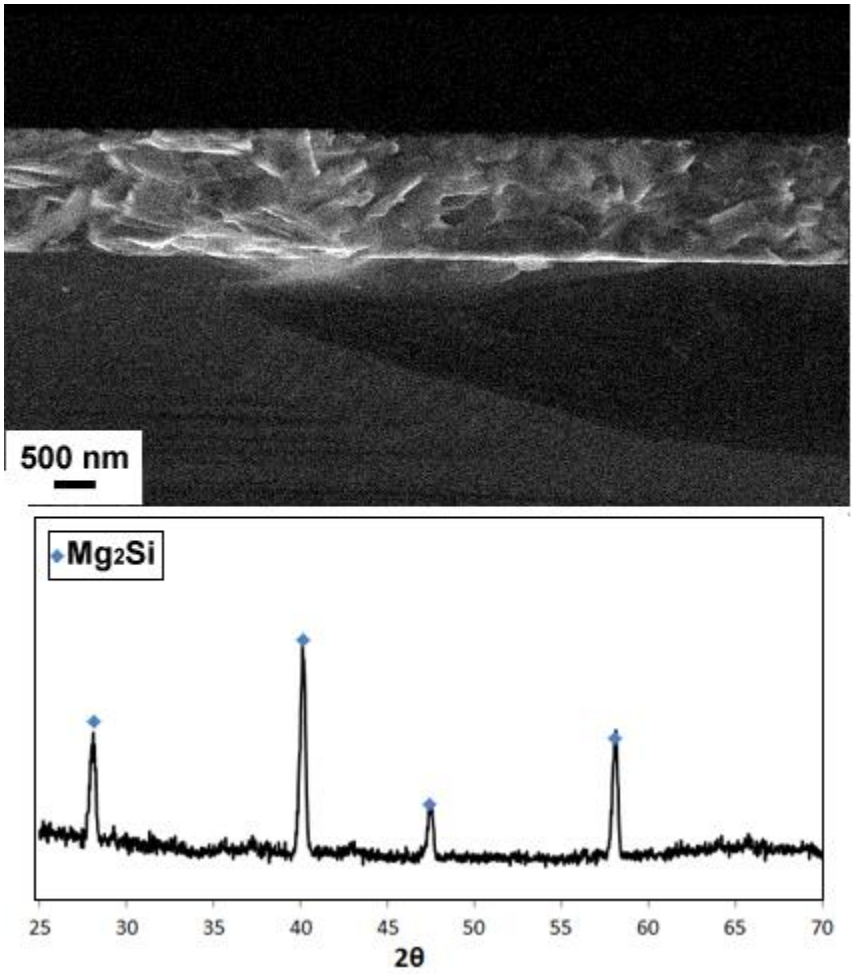

Figure 72: XRD pattern and SEM image of a fully reacted sample at 500oC for 12 hours.

The Mg_2Si thickness after complete reaction was measured at various, randomly selected areas of both Si(100) and Si(111) wafers, as shown in Table 9.

Table 9: SEM determined thickness of Mg_2Si after complete reaction.

	Si(100)	Si(111)
Mg_2Si thickness (nm)	1505	1470
	1442	1420
	1427	1345
	1371	1418
	1423	1435
Average	1434	1418
St. Dev.	48	46

To accurately observe the reaction as it happened, relatively fast XRD scans were necessary. Thus, for the *in-situ* HT-XRD evaluations, only a 2Θ range of 33-42°, which included both the primary magnesium peak (~34.4°) and the primary magnesium silicide peak (~39.7°), was monitored. Note that the exact peak position varied slightly for each run due to changes in sample height, and peaks were shifted for data analysis and display to a constant position. The total annealing time was set to 10 hours and scans were collected at 10 minute intervals, so a single experiment yielded a total of 60 scans. Representative HT-XRD patterns collected at several temperatures from 280°C-400°C are shown in Figure 73.

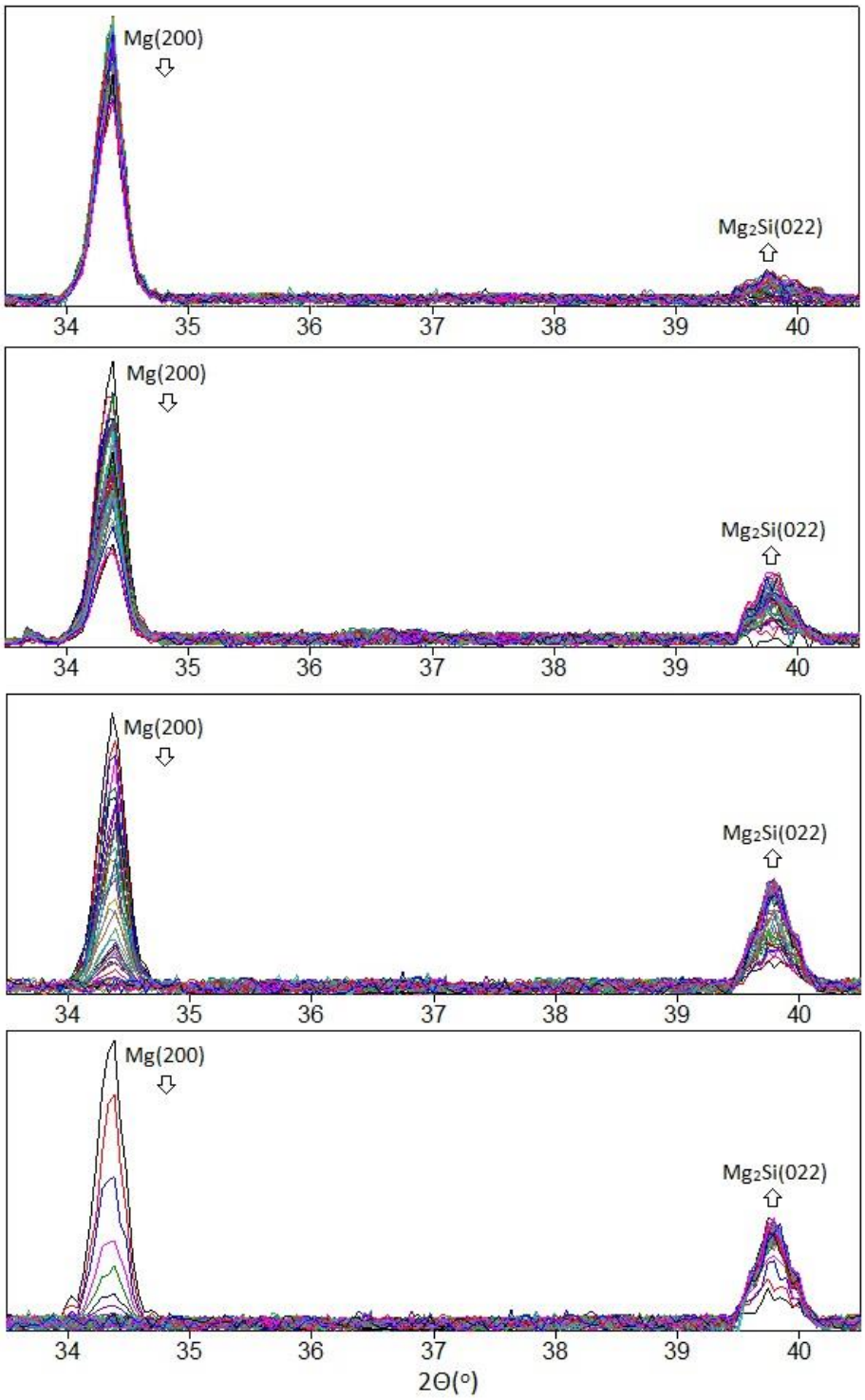

Figure 73: Collected HT-XRD diffraction scans for (from top to bottom): 280ºC, 320ºC, 360ºC, and 400ºC for Si(100) wafers. Arrows indicate whether peaks are growing or shrinking with time.

4.6 Quantitative Analysis of HT-XRD Patterns

Some qualitative observations can be made via direct observation of the HT-XRD scans shown in Figure 73. First, the large step size (.05^o) and very fast time per step resulted in a substantial amount of noise and significantly non-ideal peak shapes. The only way to remedy these issues is to increase the scan speed which, in turn, would sacrifice time resolution. At low temperatures, during which the reaction can be seen to proceed slowly, the loss of time resolution resulting from slower scans would likely not significantly affect the data collection. At higher temperatures, for example 400^{o}C, the reaction proceeded very quickly and a slower scan speed would substantially hinder reliable temporal data collection.

Despite the noise and distorted peak shapes, however, the intensity of the Mg(200) peak at ~34.4^o was clearly observed to decrease as the reaction proceeded, while the intensity of the Mg_2Si(022) peak at 39.7^o increased. At 280^{o}C, the lowest temperature at which any appreciable reaction was observed within 10 hours, the reaction proceeded gradually and even after 10 hours significant magnesium remained. At 360^{o}C and 400^{o}C, the first scan revealed a clearly distinguishable Mg_2Si(022) peak, indicating that some initial reaction occurred during the heating process. Qualitatively, the rate of reaction clearly increased as the annealing temperature increased.

To allow for quantitative evaluation of Mg_2Si growth (or, alternatively, consumption of Mg), the intensities observed for each XRD peak in Figure 73 must be correlated to the thicknesses of the reacted layer (or to the thickness of the unreacted Mg). In powder diffraction, the measured integrated peak intensity at a given 2Θ value should correlate linearly with the volume of material causing the diffraction. Due to absorptive affects,

however, for planar films the correlation is not necessarily expected to be linear—that is, a magnesium film of 1000 nm is not necessarily expected to diffract with twice the intensity of a magnesium film of 500 nm thickness. The exact relationship between observed intensities and layer thickness is not trivial to derive and, after extensive literature searches, was not found in published literature for grazing angle conditions. Such derivation is presented here for monitoring the consumption of Mg, which can then be related to the growth of Mg_2Si. The decision to use the Mg(200) peak to monitor the reaction instead of the Mg_2Si(022) peak was mainly due to the fact that the maximum observed Mg(200) peak intensity was much higher than the maximum observed Mg_2Si(022) peak intensity, and, hence, the signal to noise ratio was much better for the Mg(011) peak.

Imagine a layer of magnesium with some unknown thickness (*t*) which is capped by an inert titanium layer of some thickness (t_{Ti}). At appropriate 2Θ angles, diffraction will occur throughout the entire thickness of the magnesium film. The *observed* intensity is the sum of all the diffracted beams through the entire thickness of the layer (this is why it is often referred to as *integrated intensity).* To derive the relationship between intensity and film thickness, it was first necessary to consider the diffraction observed from a small section of the film which had an infinitesimally small thickness of dx (**Figure 74**).

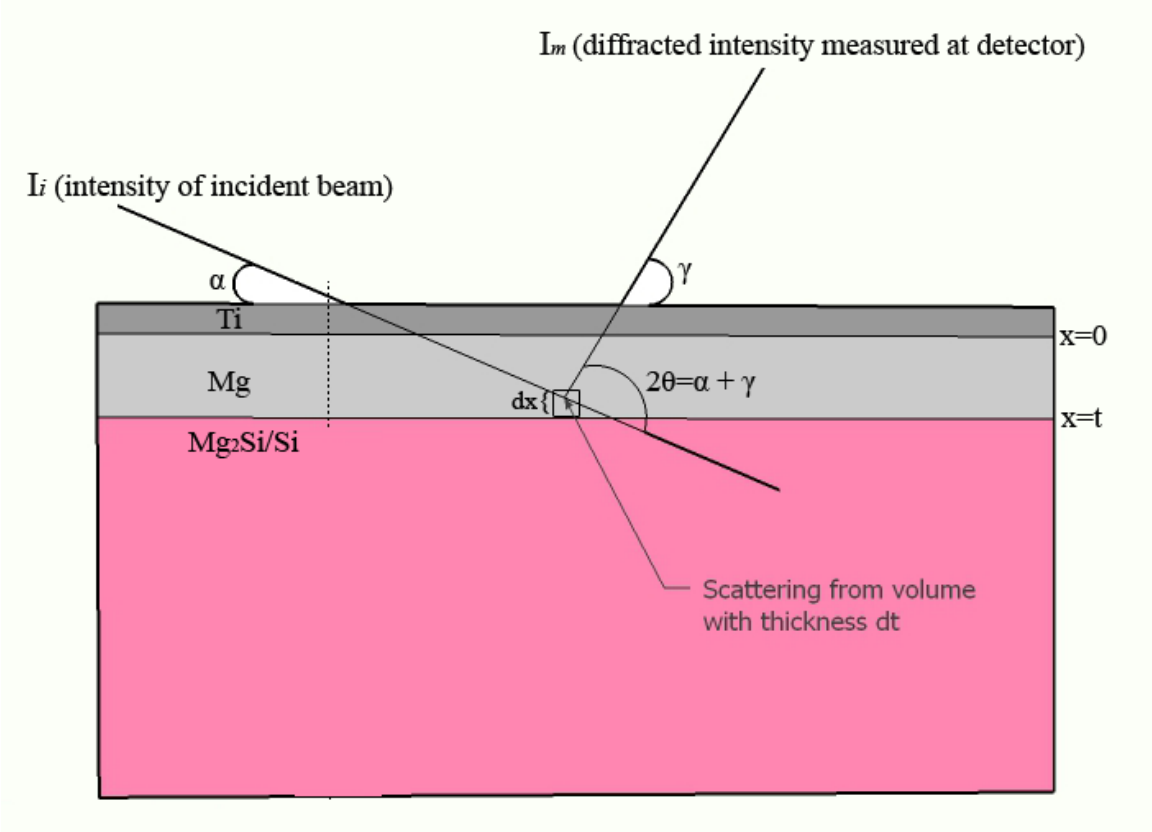

Figure 74: Diffraction for small section of film with thickness dx.

The diffracted intensity from this section of film (I_d) is proportional to the intensity of the incident beam (I_i) times the volume of material causing the diffraction. The volume of material causing diffraction is equal to the irradiated area (*A)* times the thickness of the material causing diffraction (*dx*) (equation 5.8).

$$I_d = k * I_i * V = k * I_i * A * dx \qquad \text{Eq. 5.8}$$

Note that the constant, *k*, in equation 5.8 is a function of 2Θ and includes terms like polarization factors, instrumental factors, multiplicity factors, etc. Per Bragg's law, *k* is non-zero only at 2Θ values which correspond to coherent scattering from the crystal lattice.

In order to reach the point of diffraction, the incident beam must pass through both the capping layer which has a constant thickness (t_{Ti}) and some thickness of magnesium. Due to absorption, the intensity of the incident beam *at the point of diffraction* is therefore less than the intensity of the beam generated by the X-ray source (I_o), and is equal to:

$$I_i = I_0 * exp\frac{-\mu_{Ti} * t_{Ti}}{sin(\alpha)} * exp\frac{-\mu_{Mg} * x}{sin(\alpha)} \quad \text{Eq. 5.9}$$

Here, μ_M represents the linear x-ray attenuation coefficient for metal M. The area of the beam width (*A* in equation 5.8) can be determined from trigonometry to depend on the beam width (*b*) and the angle of incidence (α) according to equation 5.10:

$$A = \frac{b}{sin(\alpha)} \quad \text{Eq. 5.10}$$

Note that, in equations 5.9 and 5.10, the thickness of the titanium layer (t_{Ti}), the attenuation coefficient of the capping layer (μ_{Ti}) the incident angle (α), the intensity of the source (I_o), and the X-ray beam width (*b)* are all constant throughout the silicidation process. Plugging equations 5.9 and 5.10 into equation 5.8, and combining all constant terms into "*k*", yields an equation for diffracted intensity *at the point of diffraction*:

$$I_d = k * exp\frac{-\mu_{Mg} * x}{sin(\alpha)} * dx \quad \text{Eq. 5.11}$$

The intensity of the diffracted beam which reaches the detector, or the measured intensity (I_m), will be less since the diffracted beam must travel back upwards through

the material before reaching the detector. The *measured intensity* (I_m), accounting for loss due to absorption of the diffracted beam before reaching the detector, is related to the diffracted angle (γ in Figure 74) and given by:

$$I_m = I_d * exp\frac{-\mu_{Mg} * x}{sin(\gamma)} * exp\frac{-\mu_{Ti} * t_{Ti}}{sin(\gamma)} \quad \text{Eq. 5.12}$$

$$I_m = k' * exp[-\frac{\mu_{Mg} * x(sin(\alpha) + sin(\gamma))}{sin(\alpha)sin(\gamma)}] * dx \quad \text{Eq. 5.13}$$

Plugging equation 5.11 into equation 5.12 and again combining constant terms yields equation 5.13, which represents the measured diffracted intensity due to a small volume of the film with thickness dx. Integration of equation 5.13 through the entire thickness of the magnesium film (from x=0 to x=*t*) gives an equation for the total measured diffracted intensity due to a magnesium film of thickness *t*, denoted I_t.

$$I_t = k' * \frac{sin(\alpha)sin(\gamma)}{\mu_{Mg} * (sin(\alpha) + sin(\gamma))} * [1 - exp(\frac{-\mu_{Mg} * t(sin(\gamma) + sin(\alpha))}{sin(\alpha)sin(\gamma)})] \quad \text{Eq. 5.14}$$

Note that the angle of diffraction (γ) can easily be determined from the measured 2Θ value for a given incident angle via the equation γ= $2\theta - \alpha$ (see Figure 74). For clarity, the sin terms and the absorption coefficient for magnesium are grouped together (denoted Ω, equation 5.15), and a simpler equation for I_t (which represents the total diffracted intensity due to a magnesium film of thickness *t*) is obtained (equation 5.16).

$$\Omega = \frac{-sin(\alpha)sin(2\theta - \alpha)}{\mu_{Mg} * (sin(\alpha) + sin(2\theta - \alpha))} \quad \text{Eq. 5.15}$$

$$I_t = k' * \Omega * [1 - exp(\frac{t}{\Omega})]$$

Eq. 5.16

The linear absorption coefficient for magnesium (μ_{Mg}) is known from literature, the incident angle (α) is held constant and set by the user, and both the total diffracted intensity (I_t) and the 2Θ angle are obtained from the measured XRD pattern. The only unknowns therefore are the thickness of the remaining magnesium film (*t)*, which is what we wish to solve for, and the constant term (*k*). The constant term can be cancelled out by introducing a reference sample with a known thickness of t_{ref}. The measured intensity of the reference sample is defined as value $I_{ref.}$. Dividing equation 5.16 by I_{ref} yields equation 5.17.

$$\frac{I_t}{I_{ref}} = \frac{1 - exp(\frac{t}{\Omega})}{1 - exp(\frac{t_{ref}}{\Omega})}$$

Eq. 5.17

The values of I_t and Ω are determined directly from the XRD pattern. The only remaining unknown is *t*, or the thickness of unreacted magnesium film at a given time.

Equation 5.17 therefore allows for conversion of the observed intensities (as measured by area under the peak) from Figure 73 to the thickness of the unconsumed magnesium layer. The only requirement is the availability of a reference sample with a known thickness of magnesium which can be measured to give I_{ref} at various temperatures. There are several options for the reference sample. The initial idea was to use the e-beam evaporator to deposit a magnesium film of known thickness (t_{ref}) onto an inert substrate, for example MgO. The diffracted intensities of the Mg-coated-MgO

sample can then be measured at various temperatures to yield I_{ref}. However, this method requires directly comparing peak intensities between XRD patterns collected from different runs. In order to compare intensities collected from different runs, an internal standard is necessary to account for things like variations in sample position, sample height, etc. Initially, it was thought that a thick titanium capping layer could serve as both the XRD standard as well as a protective layer to prevent oxidation of the magnesium. Unfortunately, the primary titanium XRD peak ($2\Theta=40.1^{o}$) interfered with the primary Mg_2Si peak ($2\Theta=39.8^{o}$). After evaluation of numerous metals, iron was the only metal which both does not react with magnesium and has XRD peaks which would not overlap with either Mg or Mg_2Si peaks. Unfortunately, the available e–beam evaporator was not configured for iron deposition.

An alternative method of obtaining t_{ref} and I_{ref} was therefore utilized. The initial thickness of magnesium deposited on the silicon wafers (before any reaction or heat treatment) was known from the quartz crystal microbalance attached to the deposition instrument (and further confirmed via SEM, within errors of the SEM). For the reactions carried out at $280^{o}C$ and $320^{o}C$, it can be seen from Figure 73 that no apparent reaction occurred before the first XRD pattern was collected. Hence, the measured intensity of Mg(001) peak from the first scan was used as I_{ref} and, and the initial coating thickness as t_{ref}. For the $360^{o}C$ and $400^{o}C$ reaction temperatures, it was clear from Figure 73 that some Mg_2Si film had already formed during the heating process and before the initial XRD pattern was collected. For these scans, a separate sample was first heated to the desired temperatures using the same heating rate, held for five minutes (the time required to complete the first scan), and then immediately cooled. The remaining thickness of

magnesium was then determined via SEM observation and used for t_{ref}, and I_{ref} was obtained from the Mg peak intensity of the first XRD pattern at each temperature.

Note that, with this method, intensities from different HT-XRD runs are never compared; only intensities from different scans within a single run are compared. This minimizes the need for an internal standard. *If* there is some change *within* a run (for example, sample height changes or sample position shifts or beam intensity decreases in the middle of a run), then without an internal standard it is impossible to compensate for such changes. In practice, however, other than random noise there appeared to be no significant systemic changes within single runs. Plots for I/I_{ref} vs. time for various temperatures, along with a magnified view of the diminishing Mg(200) peak, are shown in Figure 75.

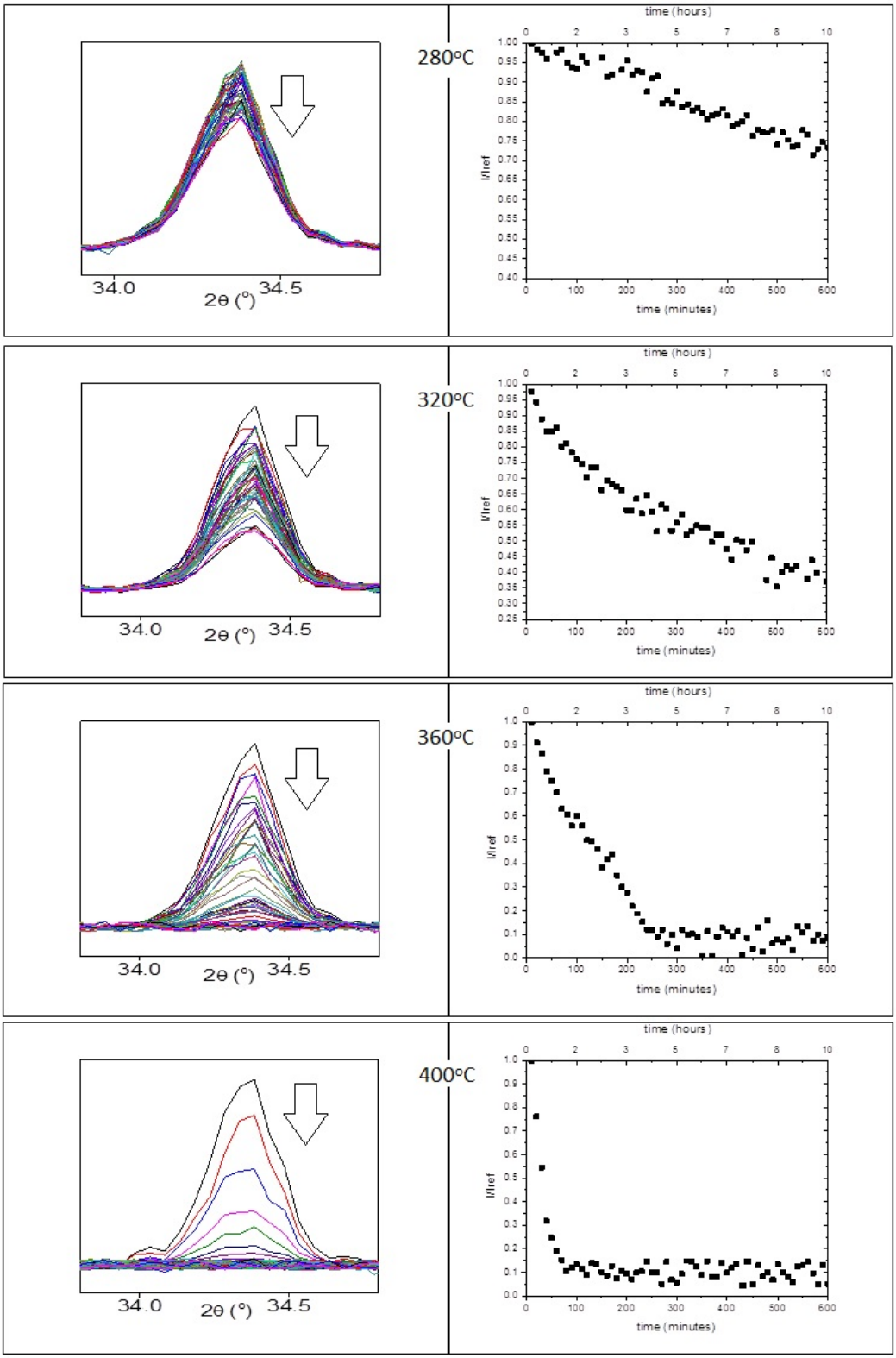

Figure 75: Relative peak intensities (I/I_{ref}) of the Mg(200) peak plotted vs. time for the XRD patterns shown in Figure 73.

Note that the scatter of data points generally increases with time. In the initial stages of the reaction, when the magnesium peak was relatively large, the percentage of peak area due to random noise was small compared to the percentage of peak area due to actual diffraction from the magnesium film. In the final stages of the reaction, when the magnesium peak was significantly smaller (or gone completely), random noise represented a much larger percentage of the peak area, and, hence, scatter in general was observed to increase with increasing reaction time. Even when the magnesium was completely consumed and there was no observable magnesium peak, there was still some area under the curve due to background noise.

Using equation 5.17, the I/I_{ref} plots shown in Figure 75 can be directly converted into plots of the thickness of the magnesium layer vs. time. However, it is desirable to report kinetics and growth rate constants in terms of *growth* of the silicide layer rather than *consumption* of the magnesium layer. In general, the thickness of a silicide of formula M_ySi expected due to consumption of a given thickness of a metal film (M) on silicon can generally be trivially expressed as:

$$t_{silicide} = (t_M^0 - t_M) * \frac{\rho_M * M_{silicide}}{\rho_{silicide} * M_M * y} \qquad \text{Eq. 5.18}$$

where t_M^0 is the starting thickness of the metal film, t_M is the thickness of the metal film after some reaction, ρ_M and $\rho_{silicide}$ are the densities of the metal and the silicide respectively, M_M and $M_{silicide}$ are the molar mass of the metal and the silicide respectively, and y is the stoichiometric factor from the formula M_ySi. Plugging in the

literature values for Mg and Mg_2Si, the thickness of Mg_2Si film can be related to the unreacted thickness of the magnesium film via:

$$t_{Mg_2Si} = 1.41(t^0_{Mg} - t_{Mg}) \qquad \text{Eq. 5.19}$$

where t^0_{Mg} is the starting thickness of the magnesium before any reaction and t_{Mg} is the thickness of magnesium after some reaction time. Combining equation 5.17 to determine t_{Mg} with equation 5.19 allows for facile determination of Mg_2Si thickness from the HT-XRD patterns. However, a few important assumptions must be made for equation 5.19 to be strictly valid. These assumptions are that: (1) the deposited magnesium thin film has a density similar to bulk magnesium; (2) that the Mg_2Si formed is stoichiometric with a Mg:Si ratio of exactly 2:1; and (3) that the polycrystalline Mg_2Si formed has a density similar to bulk Mg_2Si.

The first assumption is that the density of the e-beam deposited magnesium thin film is the same as the bulk density of magnesium. Densities of evaporated thin films may be much lower than bulk densities, especially if deposition parameters are not correctly optimized, if poor vacuum conditions are used during deposition, or if contaminants are present in the deposition chamber. In this study, however, the e-beam evaporation instrument was carefully calibrated prior to deposition, and SEM observations of the deposited Mg thickness were consistent (within error of the SEM, see

Table 8) with reported thicknesses determined using the quartz crystal microbalance built into the e-beam evaporation instrument. This agreement between the deposition thickness determined from SEM analysis and weight gain data confirms that

the deposited magnesium film was very close to near bulk density. The second assumption, that the formed Mg_2Si is stoichiometric, is almost certainly valid since Mg_2Si is a line compound[173].

The final assumption, that the density of the grown Mg_2Si film is equal to the bulk density of Mg_2Si, is a bit more liberal and is strictly true only if the resulting Mg_2Si film is stress-free. The molar volume of Mg_2Si is 3.2 times larger than the molar volume of silicon. Due to this volume difference, the consumption of Si to form Mg_2Si is expected to initially generate compressive stresses, followed by some stress relaxation process. Previous silicide literature indicates that such stresses are normally relaxed via either Coble creep[185] or Nabarro-Herring creep[186,187]. If the stress relaxation occurs *quickly* relative to the growth process, then residual compressive stress in the Mg_2Si layer at any given time will be near zero and the actual thickness of the Mg_2Si should be close to the value predicted by equation 5.19. If, however, the relaxation mechanism occurs *slowly* relative to the growth process, then the Mg_2Si layer may be under large residual compressive stresses at any given time. The density of the stressed Mg_2Si film formed will be higher than the density of stress-free bulk Mg_2Si, and the actual thickness of the grown Mg_2Si may be less than the value predicted by equation 5.19. A detailed evaluation of residual stress and relaxation mechanisms during the silicidation reaction was not undertaken. However, SEM images of several reacted samples revealed Mg_2Si thicknesses similar to the values predicted by equation 5.19 (see

Table **9**), suggesting that density differences between the Mg_2Si film and bulk Mg_2Si were negligible. This was also consistent with data found in literature, as Chu, et al.[188] reported the consumption of a 400 nm thick magnesium coating to yield an Mg_2Si layer of thickness 530 nm (only 30 nm less than the stress-free theoretical thickness of 560 nm given by equation 5.19) at 275^{o}C.

Furthermore, even if there are residual compressive stresses present during the reaction, it is likely that the variation in density caused by such stress would be limited. If compressive stresses were significant enough to substantially increase the density of the Mg_2Si film relative to bulk Mg_2Si, then the reacted layer would be expected to either spall and crack, or the reaction would stop altogether due to the positive free energy associated with the stresses. Therefore, equation 5.19 likely provides a reasonable estimate of Mg_2Si thickness even in the presence of some residual compressive stress. However, for the sake of thoroughness, the growth of Mg_2Si has been plotted in Figure 76 both in terms of thickness of the reacted layer (right axis, which requires making an assumption about the density of the Mg_2Si film) and in terms of molar amount of Mg_2Si grown per unit area (left axis, which requires no assumption about residual stress or the density of the Mg_2Si film).

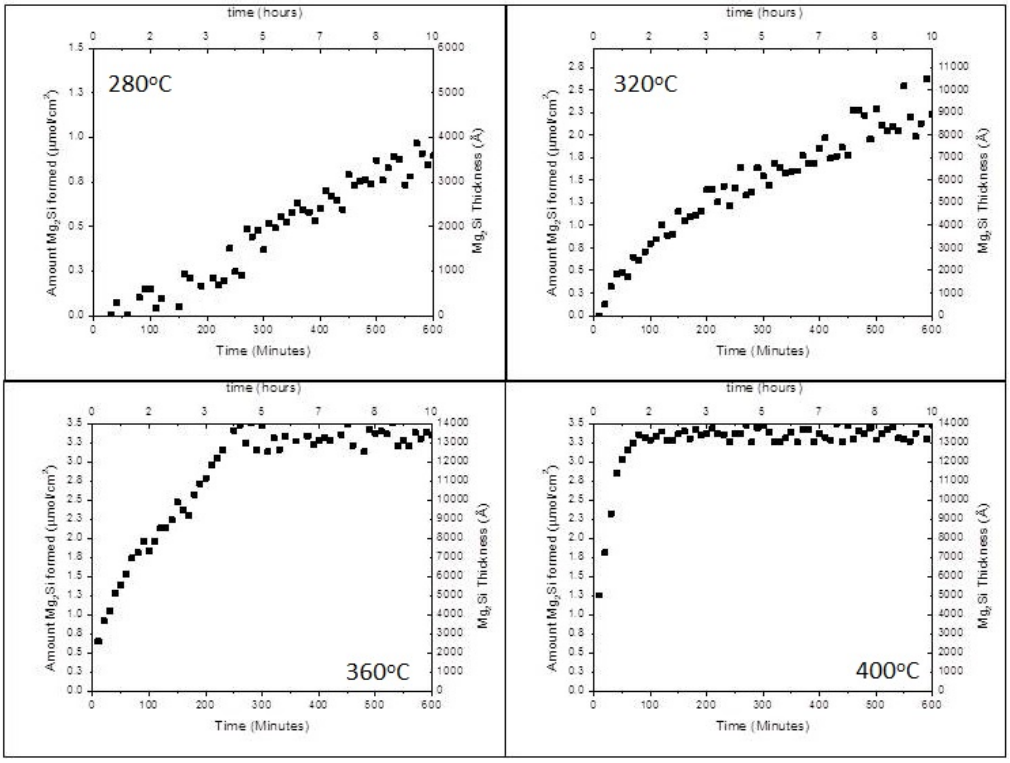

Figure 76: Plots of Mg_2Si growth for time at various annealing temperatures.

At 280°C, there appears to be a short incubation period (approximately 45-60 minutes) before sustained reaction was detected. For annealing temperatures higher than 280°C, Mg_2Si formation was observed within the first few analyses. It is difficult to tell directly from the plots in Figure 76 whether the Mg_2Si growth followed a parabolic or linear growth rate. At reaction temperatures of 280°C, the observed time (10 hours) was insufficient to establish a clear, definitive characteristic growth curve. At 320°C, the reaction appeared clearly parabolic, while for temperatures of 360°C and 400°C it was not immediately clear if the growth was parabolic or linear with respect to time since the magnesium was completely consumed and the Mg_2Si thickness leveled off before a clear curve was established. In order to differentiate between linear or parabolic rate laws, log-log plots of Mg_2Si growth at each temperature were created and are shown in Figure 77.

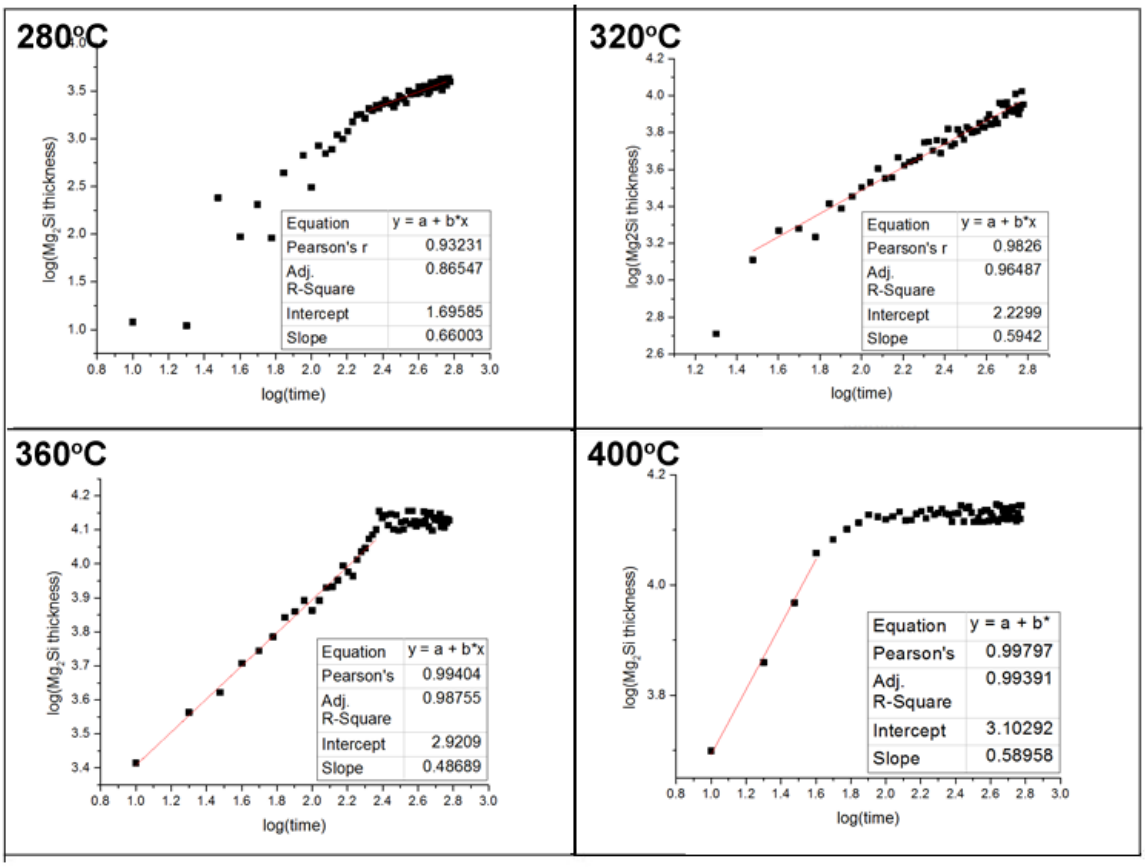

Figure 77: Log-Log plots of Mg_2Si growth at various reaction temperatures for the XRD scans shown in Figure 73.

Figure 77 shows plots of log(Mg_2Si thickness) vs log(time) for the XRD patterns shown in Figure 73, showing the slopes of the best fit lines for linear regions. For the 360°C and 400°C, data analysis was stopped after 80% of total reaction, since for later times the Mg(200) peak used for analysis was so low that noise effects started to dominate. The slopes of the best-fit lines for each of the individual runs collected (three repetitions at each temperature for both Si(100) and Si(111) substrates) is shown in Table 10.

Table 10: Slopes of best-fit lines in log(Mg_2Si thickness) vs log(time) plots.

Temperature (°C)	Si(100)			Average
280	0.66	0.63	0.68	0.66
320	0.59	0.53	0.51	0.55
360	0.49	0.44	0.42	0.45
400	0.59	0.56	0.62	0.59
Temperature (°C)	Si(111)			
280	0.71	0.64	0.74	0.70
320	0.59	0.65	0.57	0.60
360	0.47	0.50	0.46	0.48
400	0.61	0.52	0.55	0.56

Growth following parabolic rate laws (i.e., $\xi=k*t^{0.5}$) will ideally have a slope of 0.5 in the log-log plots, while growth following linear rate laws ($\xi=k*t^{1}$) will ideally have a slope of 1 in the log-log plots. The slopes of the log-log plots for temperatures 320°C, 360°C, and 400°C were all close to 0.5, conclusively demonstrating parabolic growth rates. For the 280°C reaction, the average slope was 0.66 and 0.70 for Si(100) and Si(111) substrates, respectively, which was in between the value expected for parabolic and linear growth rates. At 280°C (the lowest temperature at which any reaction was observed), there appeared to be some incubation period necessary before sustained Mg_2Si formation was achieved, as evidenced by the significant scatter at early times. At higher temperatures, sustained Mg_2Si formation began very early upon reaching the annealing temperature (320°C) or even during the heating process before the desired temperature was reached (360°C, 400°C). At 400°C. The reaction occurred very quickly, and only a few (five) usable data points could be collected. Temperatures higher than 400°C could not be evaluated since the reaction occurred too quickly for HT-XRD observation.

From the slopes in the log-log plot, it was determined that, at least at temperatures higher than 280°C, Mg_2Si formation followed a parabolic rate law. Figure 78 reveals plots of magnesium silicide formation vs. square root of time for each temperature.

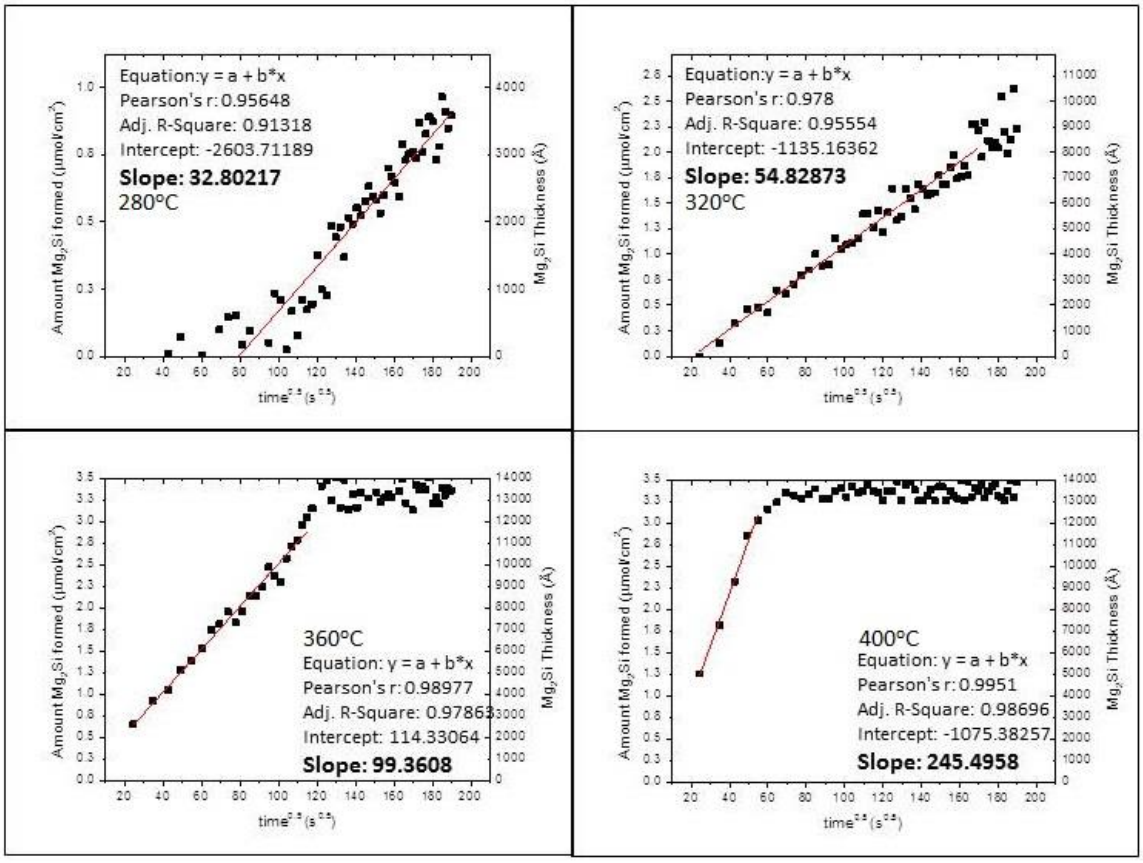

Figure 78: Growth of Mg_2Si plotted vs $time^{0.5}$ for various reaction temperatures from XRD patterns shown in Figure 73.

A linear relationship between growth and square root of time was observed for each temperature, confirming parabolic behavior. For the two higher temperatures, very strong linear fits were obtained with R-squared values of at least 0.99. At 320°C, the linear fit was still relatively good with an R-squared value of 0.96, while at 280°C the R-squared value was 0.91. For all temperatures above 280°C, the R-squared values for the plots of growth vs. square root of time were stronger than for the growth vs time plots

(shown in Figure 76), which had R-squared values of 0.92, 0.90, 0.93, and 0.82 for 280°C, 320°C, 360°C, and 400°C, respectively. The parabolic rate constant, k_p, can be determined directly from the slopes of the lines in Figure 78. In order to reliably determine the parabolic rate constant for the reactions and elucidate the activation energy for Mg_2Si growth, HT-XRD experiments were carried out in triplicate on both Si(111) and Si(100) wafers. Arrhenius plots for Mg_2Si growth on each orientation are shown in Figure 79.

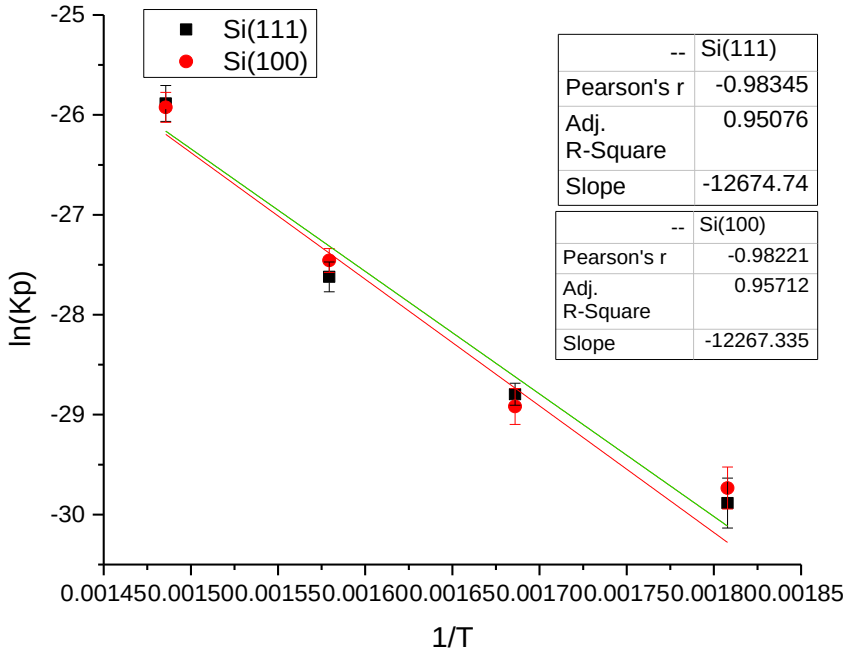

Figure 79: Arrhenius plot for growth of Mg_2Si on Si(111) and Si(100) wafers.

A strong linear fit is observed in the Arrhenius plot. Multiplication of the slope of the line times the molar gas constant yields the activation energy for the growth process. The experimentally determined activation energy and parabolic growth rates are shown in Table 11.

Table 11: Experimentally determined growth data.
Values in parenthesis represent the standard deviation or standard error.

	Activation Energy(eV)	kp (cm^2/s)			
		280°C	320°C	360°C	400°C
Si(111)	1.09 (.12)	1.05 (.11)E-13	3.12 (.18)E-13	1.01 (.17)E-12	5.73 (.15)E-12
Si(100)	1.06 (.14)	1.22 (.16)E-13	2.76 (.15)E-13	1.19 (.20)E-12	5.51 (.21)E-12

4.7 Discussion

The orientation of the Si wafer had no statistically significant effect on either Mg_2Si growth rate or activation energy. Since parabolic growth was observed and it is known that the mobile species during growth is magnesium[189], it can be concluded that the reaction is limited by solid state diffusion of magnesium through the Mg_2Si layer. *If* the microstructure of an Mg_2Si layer grown on Si(111) were significantly different than that of Mg_2Si grown on Si(100), it is possible that magnesium mobility (and therefore overall reaction kinetics) through Mg_2Si would differ for differing Si orientations. However, similar growth rates and activation energies suggest that there is likely no significant difference in the structure of Mg_2Si grown on Si(100) vs. Si(111) substrates.

The question arises of whether the measured values for activation energy and growth rates are reasonable and consistent with the literature. Most silicide literature has been focused on transition metal silicides rather than alkaline earth metal silicides, and, as a result, relatively few studies have quantitatively evaluated Mg_2Si thin film growth. Only two studies have been found in published literature which report either activation energy or growth rates for the solid/solid silicidation reaction between Mg and Si to form Mg_2Si.

In a 1983 paper, J.P. Stark, et al. investigated Mg_2Si growth by depositing between 200-1000 nm of magnesium onto silicon substrates and annealing the samples at 400°C for times of 10 minutes to 1 hour[190]. Depth profiling to locate the silicide interface and measure growth rate was conducted via Auger electron spectroscopy (AES), while magnesium isotope separation was measured via secondary ion mass spectrometry (SIMS). Stark observed parabolic growth, and the separation of magnesium isotopes was consistent with grain boundary diffusion of magnesium. However, the reported parabolic rate constant at 400°C was only 8.1E-13cm^2/s (using the k_p definition given in equation 5.7). This is nearly an order of magnitude less than the rate constants determined here at 400°C. There were some important differences between Stark's experiments and the ones conducted in this study. In Stark's study the reaction was conducted under vacuum atmosphere while in the current study flowing inert gas was used. Annealing atmosphere has been shown to have a significant effect on silicide growth, with argon atmospheres resulting in more rapid observed growth than vacuum[191].

Another significant factor which could explain the discrepancy is the absence of a protective capping layer in Stark's study. It is well known that a substantial amount of magnesium oxide can easily form on the deposited magnesium at elevated temperatures used for silicide growth. Once an MgO layer forms, it will not react further. If the growth rate is determined by depth profiling to locate the silicide/metal interface (as it was in Stark's study), it is quite possible that the MgO layer could be misinterpreted as unreacted magnesium. Apparent growth rates would therefore be lower than actual growth rates. It should further be noted that in the same paper, Stark reported parabolic growth of VSi_2. Subsequent publications have found that VSi_2 forms under linear growth

rates over similar temperature ranges, and suggested that observed parabolic growth rate usually indicates the presence of contaminants, especially oxygen[175]. Presumably, Stark used the same instrumentation for both magnesium and vanadium deposition and reaction, so evidence of oxygen or other contamination in the deposited vanadium film suggests a high probability of similar contamination in the deposited magnesium films.

Stark only examined growth at 400^{o}C, and so did not determine an activation energy. Recently (November 2013), a paper was published by Udono, et al. in Physics Status Solidi C which used Raman spectroscopy to evaluate the solid-state reaction of magnesium deposited on a silicon substrate[192]. Although growth constants were not reported, the activation energy was determined to be 0.70 eV, significantly lower than the ~1.0-1.1eV determined here. However, the Arrhenius plot, reproduced without modification in Figure 80, was *highly* irregular. While the authors acknowledge the irregularities in the Arrhenius plot, they claim that over a small temperature range a linear dependence could be observed and that they were able to extract the activation energy from this region. The authors offer no explanation as to why only a portion of the plot was linear and even in the part of the plot the authors identify as linear, there was significant scatter of Raman intensities measured at similar temperatures. The irregularities in their Arrhenius plot suggest that their reported activation energy should be treated with caution.

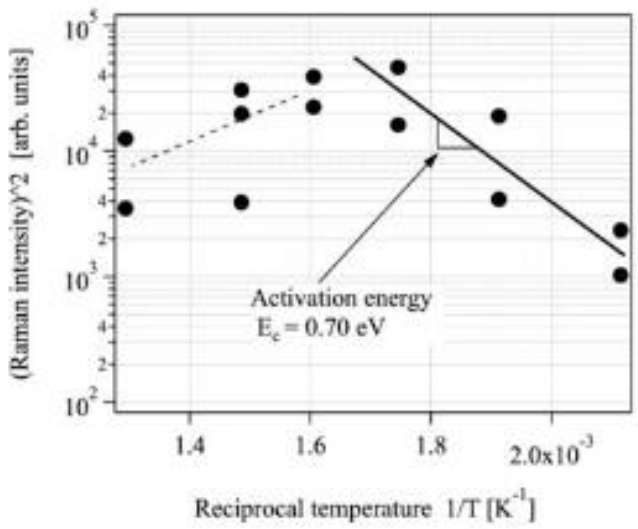

Figure 80: Arrhenius plot for Mg_2Si taken from Udono, et al.[192]

No other studies could be found which report specific growth rates or an activation energy for the solid/solid reaction of an Mg-coated silicon wafer. However, several studies offer observations at single annealing temperatures or times. Chu, et al.[188] reported growth of a 530 nm thick magnesium silicide film after annealing for 70 minutes at 275ºC, while Janega et al[193] reported the growth of a 300 nm thick magnesium film after annealing for 30 minutes at 300ºC. These observations correspond to parabolic growth rates of approximately 6.7E-13cm^2/s and 5E-13cm^2/s at 275ºC and 300ºC, respectively, which compare relatively well with values reported here.

Although no other quantitative kinetic data for solid-state Mg_2Si growth could be found, there is substantial data in the literature regarding growth of a large variety of other silicides. The parabolic growth constants and activation energy reported here for Mg_2Si compare relatively favorably with data collected from other silicides. F.M. d'Heurle with IBM investigated silicide thin film formation extensively in the 1980's and 1990's, publishing numerous papers, reviews, and book chapters[194]. D'Huerle observed

that, for silicides whose growth is controlled by diffusion of the non-silicon element, certain general approximations can be made relating both activation energy and growth constants with the melting temperature of the silicide[195]. First, the activation energies for formation of different silicides generally scale with melting temperatures in a relationship approximately given by:

$$Q(eV) \approx .001T_M \Longleftrightarrow Q(eV)/R \approx 11.5T_M \qquad \text{Eq. 5.20}$$

where Q is the activation energy of the reaction and R is the molar gas constant with units eV*atom^{-1}*K^{-1}. The melting point of Mg_2Si is 1375K (1102^{o}C)[173], which should yield a predicted activation energy of approximately ~1.3eV according to d'Huerle's relation. This relationship is merely a general approximation based on observed data, not a strict rule derived from kinetic theory. The measured activation energy in this study of ~1.1 eV is in reasonable agreement with this relationship, certainly more so than the 0.70eV reported by Udono, et al. A plot of melting temperature vs. reported activation energy for a number of metal-rich silicides with the formula M_2Si is shown in Figure 81.

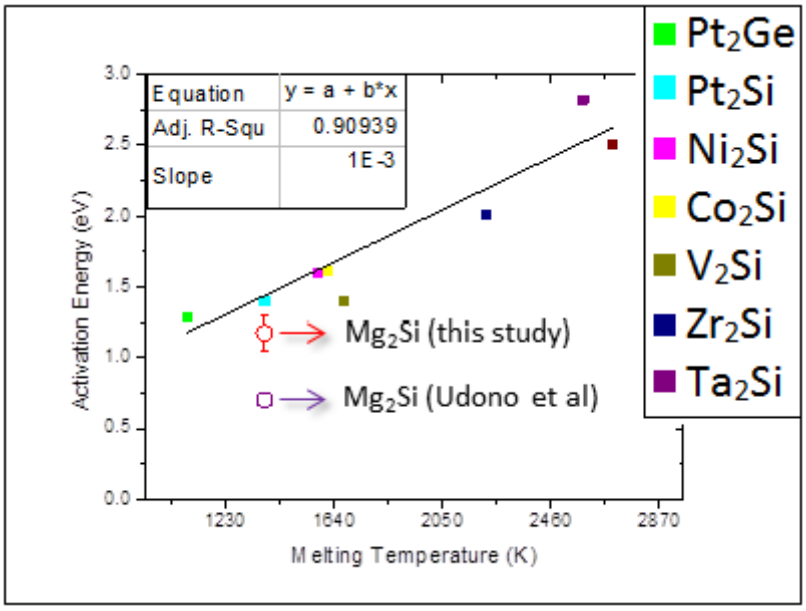

Figure 81: Activation energy vs. melting temperature for a variety of dimetal silicides, adapted from d'Huerle et al.

In addition to activation energies, d'Huerle observed that parabolic growth constants can also be approximately correlated with the melting temperature for a variety of silicides. D'Huerle observed that the lowest temperature at which growth is observed (T_f) occurs around $0.4T_M$, and the parabolic growth constant at this temperature is generally between 10^{-13} to 10^{-14} cm^2/second.

$$T_f(K) \approx 0.4T_M(K) \Leftrightarrow rate\ at\ T_f \approx 10^{-13}\ to\ 10^{-14} cm^2/s \qquad \text{Eq. 5.21}$$

In this study, the lowest temperature at which growth was observed was 553.15K (280°C), which corresponds to $0.4T_M$ almost exactly, very close to the value predicted by d'Huerle's relationship. The parabolic rate constant at this temperature is ~1E-13cm^2/s, which is also in strong agreement with d'Huerle's observation and consistent with the growth rates of other silicides at similar homologous temperatures (Figure 82).

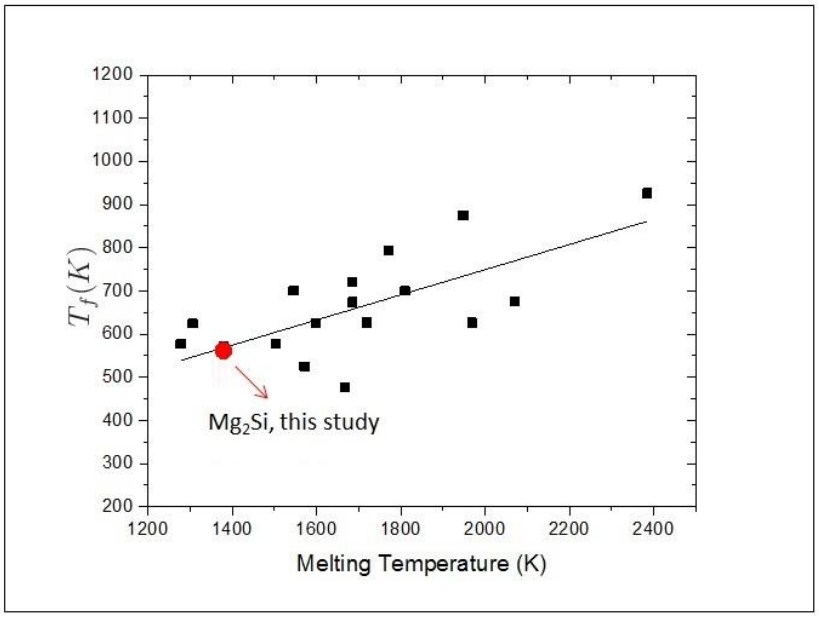

Figure 82: Initial formation temperature (corresponding to growth rates of ~1E-13cm^2/s) vs. melting temperature for a variety of dimetal silicides, adapted from d'Huerle et al.

Both the activation energy and rate constant obtained in this study are therefore quite reasonable and consistent compared to values identified for growth of other silicides. D'Huerle then compared the activation energies and rate constants observed in diffusion-controlled silicide growth with the approximate activation energies and diffusivities of grain boundary and lattice self-diffusion in pure metals.

$$Q_{g.b.}(eV)/R \approx 10 - 12T_M \quad \text{Eq. 5.22}$$

$$Q_{lattice}(eV)/R \approx 18T_M; \quad \text{Eq. 5.23}$$

$$D_{g.b.}\ at\ 0.4T_M \approx 10^{-10} cm^2/s \quad \text{Eq. 5.24}$$

$$D_{lattice}\ at\ 0.4T_M \approx 10^{-21} cm^2/s \quad \text{Eq. 5.25}$$

where $Q_{g.b.}$ and $Q_{lattice.}$ are the activation energies for grain boundary self-diffusion and lattice self-diffusion in pure metals; and $D_{g.b.}$ and $D_{lattice}$ are the diffusivities for grain boundary and lattice self-diffusion in pure metals. Comparison of equations 5.22 and 5.23 with equation 5.20, and of equations 5.24 and 5.25 with equation 5.21 clearly suggests a grain boundary mechanism, as opposed to lattice diffusion, as the dominant form of mass transport. Furthermore, grain boundary diffusion has been directly identified as the primary mechanism of diffusion in similar dimetal silicides[196]. Grain boundary diffusion could also explain the unstable, non-parabolic growth observed at short times and low temperatures (see Figure 77 for 280^{o}C), as film growth (driven by grain boundary diffusion through Mg_2Si) may be occurring simultaneously with grain growth of the Mg_2Si, resulting in non-parabolic kinetics. Eventually, grain sizes may stabilize and parabolic growth, through standard grain boundary diffusion mechanisms, would be expected to dominate as was observed for growth at 280^{o}C for longer time periods. At higher temperatures, it is possible that grain sizes stabilize much faster which explains why no unstable incubation period was observed for growth at temperatures greater than 320^{o}C. Unfortunately, attempts to determine the Mg_2Si grain size directly from the HT-XRD patterns yielded inconsistent results (peak fitting resulted in poor fits with high error values and no consistent trend was observed), likely due to the very fast scan speeds used which resulted in non-standard peak shapes with significant noise. Additional experimentation is therefore necessary to conclusively confirm grain boundary diffusion as the primary mechanism of diffusion during Mg_2Si growth.

4.8 Conclusion

Grazing angle, high temperature *in-situ* X-ray diffraction was successfully utilized for the first time to monitor the solid state formation of a silicide, Mg_2Si, on a Si substrate. Parabolic growth rates were observed, indicating solid-state diffusion through the reacted zone as the rate limiting step. Equations were derived to quantitatively extract growth constants and activation energy from the HT-XRD patterns. Growth rates between 1E-13 to 6E-12 cm^2/s were obtained for temperatures of 280°C to 400°C, respectively, and an activation energy of approximately 1.1 eV was determined for the growth process. The experimentally determined activation energy and growth constants compared reasonably well with general trends reported for other silicides.

4.9 References

[168] Petrovic, John J., and A. K_ Vasudevan. "Key developments in high temperature structural silicides." *Materials Science and Engineering: A* 261.1 (1999): 1-5.

[169] Chen, L. J. "Metal silicides: An integral part of microelectronics." *JOM* 57.9 (2005): 24-30.

[170] Anderson, R., et al. "Nucleation-controlled thin-film interactions: Some silicides." *Applied Physics Letters* 35.3 (2008): 285-287.

[171] Corcoran, Yunji L., et al. "Grain boundary diffusion and growth of titanium silicide layers on silicon." *Journal of electronic materials* 19.11 (1990): 1177-1183.

[172] Lien, C-D., M-A. Nicolet, and S. S. Lau. "Kinetics of silicides on Si< 100> and evaporated silicon substrates." *Thin Solid Films* 143.1 (1986): 63-72.

Lien, C-D., M-A. Nicolet, and S. S. Lau. "Kinetics of $CoSi_2$ from evaporated silicon." *Applied Physics A* 34.4 (1984): 249-251.

[173] Nayeb-Hashemi, A. A., and J. B. Clark. "The Mg− Si (Magnesium-Silicon) system." *Journal of Phase Equilibria* 5.6 (1984): 584-592.

[174] Zhang, Shi-Li, and Mikael Östling. "Metal silicides in CMOS technology: Past, present, and future trends." *Critical reviews in solid state and materials sciences* 28.1 (2003): 1-129.

[175] Krautle, H., M-A. Nicolet, and J. W. Mayer. "Kinetics of silicide formation by thin films of V on Si and SiO_2 substrates." *Journal of Applied Physics* 45.8 (1974): 3304-3308.

Nava, F., et al. "Phase transformations in alloy and bilayer thin films of vanadium and silicon." *Journal of applied physics* 59.7 (1986): 2429-2438.

Psaras, P. A., M. Eizenberg, and K. N. Tu. "Sequential silicide formation between vanadium and amorphous silicon thin-film bilayers." *Journal of applied physics* 56.12 (1984): 3439-3444.

[176] Knapp, J. A., et al. "Kinetics and morphology of erbium silicide formation." *Journal of applied physics* 58.10 (1985): 3747-3757.

Wittmer, Marc. "Growth kinetics of platinum silicide." *Journal of applied physics* 54.9 (1983): 5081-5086.

Pico, C. A., and M. G. Lagally. "Kinetics of titanium silicide formation on single-crystal Si: Experiment and modeling." *Journal of applied physics* 64.10 (1988): 4957-4967.

[177] Gibson, P. N., et al. "Modelling of the structure of CdS thin films." *Thin Solid Films* 361 (2000): 34-40.

[178] Ares, J. R., et al. "Hydrogen desorption in nanocrystalline MgH_2 thin films at room temperature." *Journal of Alloys and Compounds* 495.2 (2010): 650-654.

[179] Störmer, Michael, et al. "Structure and corrosion of magnetron sputtered pure Mg films on silicon substrates." *Plasma Processes and Polymers* 4.S1 (2007): S557-S561.

[180] Rao, Y. Kris. *Stoichiometry and thermodynamics of metallurgical processes*. CUP Archive, 1985.

[181] *Powder Diffraction File* Card No. XX for Mg, Card No. 00-005-0682 for Ti(International Center on Diffraction Data, Newtown Square, Pennsylvania); 〈www.icdd.com〉.

[182] Murray, J. L. "The Mg− Ti (Magnesium-Titanium) system." *Bulletin of Alloy Phase Diagrams* 7.3 (1986): 245-248.

[183] Daoudi, Mourad Ibrahim, Abdelhafid Triki, and Abdelkrim Redjaimia. "DSC study of the kinetic parameters of the metastable phases formation during non-isothermal annealing of an Al–Si–Mg alloy." *Journal of thermal analysis and calorimetry* 104.2 (2011): 627-633.

[184] *Powder Diffraction File* Card No. XX for Mg, Card No. 35–0773 for Mg_2Si, 00-004-0770 for Mg (International Center on Diffraction Data, Newtown Square, Pennsylvania); ⟨www.icdd.com⟩.

[185] Liew, K. P., et al. "Characterization and Modeling of Stress Evolution During Nickel Silicides Formation." (2003).

[186] Buaud, P. P., et al. "In situ strain measurements during the formation of platinum silicide films." *Journal of Vacuum Science & Technology B: Microelectronics and Nanometer Structures* 9.5 (1991): 2536-2541.

[187] Tinani, Manisha, et al. "In situ real-time studies of nickel silicide phase formation." *Journal of Vacuum Science & Technology B: Microelectronics and Nanometer Structures* 19.2 (2001): 376-383.

[188] Chu, W. K., et al. "Implanted noble gas atoms as diffusion markers in silicide formation." *Thin Solid Films* 25.2 (1975): 393-402.

[189] Ohring, Milton. *Materials science of thin films*. Academic press, 2001; and Chu, W. K., et al. "Implanted noble gas atoms as diffusion markers in silicide formation." *Thin Solid Films* 25.2 (1975): 393-402.

[190] Lim, B. S., and J. P. Stark. "The thin film reactions—Mg_2Si and VSi_2." *Acta Metallurgica* 32.6 (1984): 915-918.

[191] Xiao, Qing Quan, et al. "Effect of Annealing Atmosphere on the Mg_2Si Film Growth Deposited by Magnetron Sputtering." *Advanced Materials Research* 129 (2010): 290-294.

[192] Ikehata, T., Ando, T., Yamamoto, T., Takagi, Y., Sato, N., & Udono, H. (2013). Solid-phase growth of Mg_2Si by annealing in inert gas atmosphere. *physica status solidi (c)*.

[193] Janega, P. L., et al. "Contact resistivity of some magnesium/silicon and magnesium silicide/silicon structures." *Applied physics letters* 53.21 (1988): 2056-2058.

[194] d'Heurle, F. M., and P. Gas. "Kinetics of formation of silicides: A review." *Journal of materials research* 1.01 (1986): 205-221.

d'Heurle, François M., and Olivier Thomas. "Stresses during silicide formation: a review." *Defect and diffusion forum*. Vol. 129. 1996.

Gas, P., and F. M. d'Heurle. "4 Diffusion in silicides." *Diffusion in Semiconductors*. Springer Berlin Heidelberg, 1998. 1-38.

[195] Gas, P., and F. M. d'Heurle. "Formation of silicide thin films by solid state reaction." *Applied surface science* 73 (1993): 153-161.

[196] Pretorius, R., et al. "Radioactive silicon as a marker in thin-film silicide formation." *Applied Physics Letters* 30.10 (1977): 501-503.

Van Gurp, G. J., W. F. Van der Weg, and D. Sigurd. "Interactions in the Co/Si thin-film system. II. Diffusion-marker experiments." *Journal of Applied Physics* 49.7 (1978): 4011-4020.

Milanese, Chiara, et al. "Reactive growth of tantalum silicides in Ta-Si diffusion couples." *The Journal of Physical Chemistry B* 106.23 (2002): 5859-5863.